Modelling the Accretion Process in Intermediate Polars

Thesis

UNRESTRICTED

Modelling the Accretion Process in Intermediate Polars

by

Peter Taylor

Thesis submitted to the Open University

for the degree of Doctor of Philosophy

1997

Astrophysics Group, Department of Physics, Open University.

Date of submission: 30th September 1997
Date of award : 6th April 1998

ProQuest LLC.
789 East Eisenhower Parkway
P.O. Box 1346
Ann Arbor, MI 48106 – 1346

Modelling the Accretion Process in Intermediate Polars

by Peter Taylor

Abstract

Intermediate Polars form a subclass of the cataclysmic variables, wherein a white dwarf accretes material from a main sequence star. They are inferred to have a magnetic field of $\gtrsim 10^6$ G which has observable effects on the accretion, in particular whether it occurs mainly through a truncated disc, or directly via a stream. The result is pulsed X-ray emissions, caused by occultation of the bright area, and absorption of the X-rays. The project concerning this thesis is to develop a computer model to simulate these pulses using the assumed physics involved, hence to constrain the physical parameters for particular systems.

This thesis starts in Chapter 1 with an introduction to intermediate polars, setting them in context, and pointing out some of the unknown quantities and problems involved with them. Chapter 2 briefly describes some of the instrumentation used to obtain the data, and gives examples of X-ray data from some of the systems. Chapter 3 gives a more detailed examination of two particular objects, AO Psc and V1223 Sgr, using observations from the *Ginga* and *ROSAT* satellites, and concludes that both have a high inclination, and are predominantly disc-fed. Chapter 4 is the core of the thesis, in which some of the work discussed in Chapter 1 is taken further, with a detailed re-evaluation of the geometry involved, and how these are incorporated into the computer simulation. The results of using this are discussed in Chapter 5, although its use up to the present has been in investigating the parameter space rather than formally fitting to known systems. Chapter 6 discusses this latter possibility, and considers enhancements which would be useful to include. Also in this final chapter, a brief comparison to another model from a different research team is made.

Declaration

I hereby declare that no part of this thesis has been previously submitted to this or any other University as part of the requirement for a higher degree. The work described herein was conducted by the undersigned except for the contributions from colleagues and other workers which are acknowledged in the text, and in the following note on publications.

Peter Taylor

30th September, 1997

Publications

Some of the work reported here has been published elsewhere as follows:

Chapters 2 & 3

Norton, A.J., Beardmore A.P., Taylor P., 1996. *Mon. Not. R. astr. Soc.*, **231**, 783. "On the interpretation of intermediate polar X-ray power spectra"

Taylor P., Beardmore A.P., Norton, A.J., Osborne J.P. and Watson M.G., 1997. *Mon. Not. R. astr. Soc.*, **231**, 783. "Ginga and ROSAT observations of AO Psc and V1223 Sgr"

Norton, A.J., Hellier C., Beardmore A.P., Wheatley P.J., Osborne J.P. and Taylor P., 1997. *Mon. Not. R. astr. Soc.*, **231**, 783. "Stream-fed and dic-fed accretion in TX Columbae"

This thesis is dedicated to

Mum & Dad

For their support (both financial and otherwise!)

Contents

"To make progress in all this, we need to begin with simplified (oversimplified?) models and ignore the critics' tirade that the real world is more complex. The real world is always more complex, which has the advantage that we shan't run out of work. "

John Ball 1984. Ethology and Sociobiology, vol. 5, p. 145.

Chapter 1

Introduction

This report is an account of the development of a computer simulation used to model observations of X-rays from *intermediate polars*. These systems are described in this chapter and set in context with related objects, together with an overview of the relevant ideas and assumptions used in the simulation. Subsequent chapters discuss the X-ray observations of intermediate polars, give a detailed look at the development of the simulation, show results of testing, and report recent observations of two particular intermediate polars, AO Psc and V1223 Sgr, using data from the *Ginga* and *ROSAT* satellites.

1.1 Cataclysmic variables

Intermediate polars (detailed definition in section 1.3.4) form a subset of the class of objects known as *cataclysmic variables* (CVs) – semi-detached interacting binaries in which a white dwarf (the primary) accretes material via Roche-lobe overflow from its companion (the secondary), usually a late-type red dwarf. Figure 1.1 shows the Roche potentials of such a binary system. The accretion occurs when they are so close that the secondary fills its Roche lobe, and material spills through the inner Lagrangian point and falls towards the white dwarf.

The accretion processes are of great interest, and can happen in various ways, depending largely on the strength of the white dwarf's magnetic field. In non-magnetic (or low

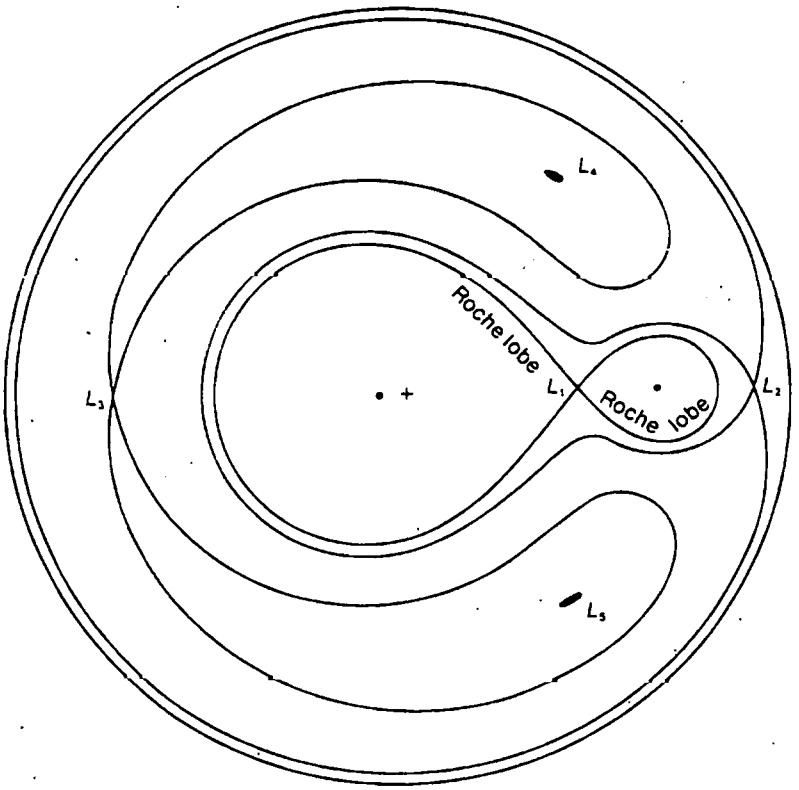

Figure 1.1: Roche potentials for a cataclysmic variable.

magnetic-field strength) systems the accretion is via an *accretion disc* which is thought to extend down to the white dwarf surface. Accretion discs are themselves objects of interest, and can occur in other types of systems, for example accreting neutron stars, and in active galactic nuclei. In magnetic cataclysmic variables the field may be too strong to allow a disc to form; in lower strength systems a disc forms, but is disrupted at some distance from the white dwarf (typically several white dwarf radii). Magnetic and non-magnetic in this context are defined empirically, that is if a disc is disrupted or absent, this is considered to be due to a magnetic field, although in some magnetic systems there is polarization of light in the optical (see below), which is interpreted as being direct evidence of a strong magnetic field.

The modern era of study of cataclysmic variables may be considered to have started in about 1954, when observations of Nova Herculis 1934 (now identified with DQ Her), using a photoelectric photometer attached to the Mount Wilson-100 inch reflector, revealed a pulse in the optical and UV at a period of 71s, which at the time was one of the fastest known for stellar objects (Walker, 1954 and 1956). This study also revealed DQ Her to be an

eclipsing binary, which led Walker to suggest tentatively that all novae may be binaries. It was generally assumed that the explanation for the pulse must involve a compact object, but no detailed models were accepted until the 1970s, when the discovery and modelling of pulsars (using neutron stars) gave an incentive to rapid rotation and accretion models with white dwarfs in semi-contact binaries. Calculations (Lamb, 1974) show that in the white dwarf case, accretion can result in the release of copious amounts of gravitational energy. In magnetic systems, if a substantial portion of the infall releases its energy near the white dwarf surface over a small area, the resulting temperatures lead to radiation predominantly in the X-ray band, with ultra-violet and some gamma radiation. Attempts were made to detect the predicted X-ray flux from DQ Her using the *Einstein* observatory (Córdova, Mason and Nelson, 1981), but none was discovered at that time (or indeed up to the time of writing). However, such signals *were* seen in the systems AE Aquarii (Patterson, 1979), AO Piscium (Patterson and Price, 1981 and White and Marshall, 1981), and V1223 Sagittarii (Steiner *et al.*, 1981), in accordance with the model [1]

Comprehensive reviews of cataclysmic variables are given by Córdova (1993) and Warner (1996).

1.2 Non magnetic CVs

In non-magnetic CVs, the accreting material forms a disc which extends down to the white dwarf surface. At some point close to the surface, a *boundary layer* is formed, where the material is braked from its Keplerian speed to the white dwarf rotation speed, with consequent release of kinetic energy. Frank, King and Raine (1992) (hereafter FKR92) discuss this in detail.

Non-magnetic CVs were originally classified as *classical novae* (or simply *novae*), *dwarf novae*, *recurrent novae* and *nova-like objects*. See for instance Warner (1996). For convenience these may be abbreviated to CN, DN, RN and NL respectively. In this classification, CN have only *one* observed eruption, the increase in brightness being from 6 to 19 magnitudes. DN are novae which erupt at irregular intervals, with varying increases in magnitude, but generally smaller than for CN ($\simeq 2-5$ magnitudes). The intervals between eruptions is

[1] The actual spin period of DQ Her is now thought to to be 142s (Zhang et al, 1995) from optical photometry.

from $\sim$ 10 days to tens of years. RN are novae which were previously identified as CN, but are observed to undergo a subsequent eruption. In DN there is a loose correlation between the size of the outburst and length of preceding/subsequent intervals.

The outburst of classical novae is satisfactorily modelled by assuming that the accretion of material on the white dwarf surface results at some point in a *thermonuclear runaway*, where the temperature and pressure of the hydrogen-rich accumulation is sufficient for it to undergo fusion.

The dwarf nova outburst, however, is thought to be due to the release of gravitational energy caused by a temporary large increase in the amount of mass transfer. There is some overlapping here, with some stars originally classified as CN also showing DN outbursts.

NL stars are those systems which are thought to be a CV (i.e. semi-detached binaries with accreting white dwarf) but which have not been observed to erupt. In these cases they may be expected to erupt on timescales of centuries or millenia, but our observational baseline is only $\sim$ one century or so. Most of the magnetic CVs are classed as NL, since they are identifiable as such by signatures other than outbursts.

1.3 Magnetic CVs

In the magnetic cataclysmic variables, material falls onto the white dwarf in a trajectory guided by magnetic field lines, and splashes down in the vicinity of the magnetic poles. These processes involve complex magnetohydrodynamic interactions, largely unsolved, and the temperatures reached at the "splashdown" regions can be several times 10^8 K (compare $\sim 10^4 - 10^5$ K for the normal white dwarf surface temperature). These temperatures result in emission of radiation largely in the ultra-violet and X-ray band. This is discussed in more detail in section 1.3.2 below.

A diagram of the splashdown region is given in figure 1.2.

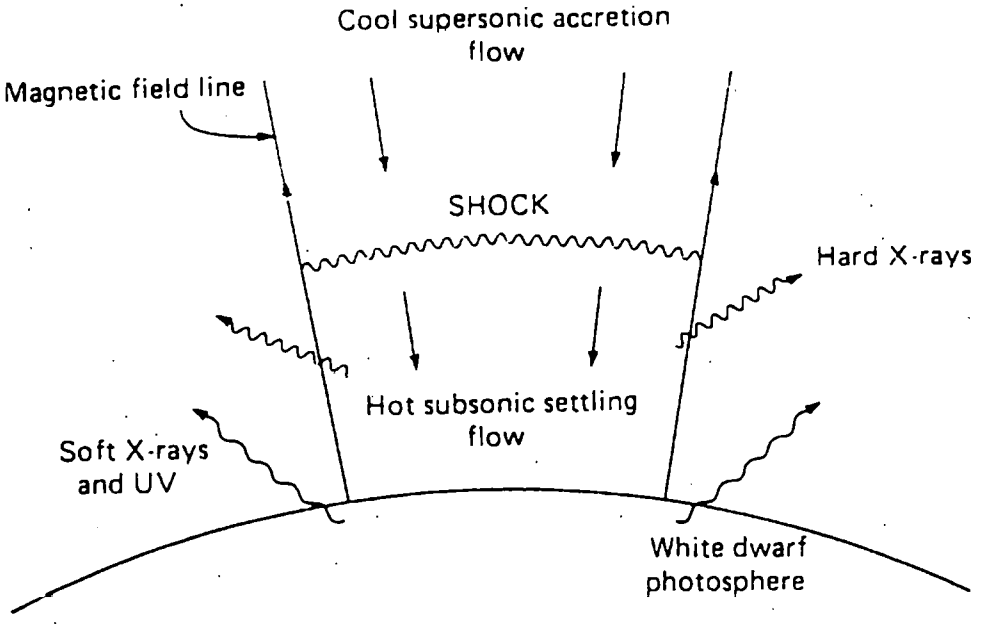

Figure 1.2: The splashdown region for a magnetic cataclysmic variable

1.3.1 Limiting values for magnetic moment in CVs

Following an analysis by FKR92 and Warner (1996), we can estimate a lower limit for the strength of the magnetic field (and the magnetic moment) below which the CV can be considered to be non-magnetic. Firstly, the magnetic moment, μ, is related to the field strength $B(r)$ (at a distance r from the white dwarf centre) by $\mu \sim Br^3$, assuming a dipole field. (μ is a constant for the system.)

The field will affect the accretion flow when the magnetic pressure (P_{mag}) equals or exceeds the "ram" pressure (P_{ram}) of the matter (which is supersonic). The plasma should thread on to the field lines at around this point.

Calling the radius at which equality occurs R_m, the system can be considered non-magnetic when $R_m \lesssim R_*$ (R_* being the white dwarf radius). In cgs units the magnetic pressure is given by (FKR92 p. 38)

$$P_{mag} = B^2/8\pi$$

$$= \mu^2/(8\pi r^6), \tag{1.1}$$

and the ram pressure for a gas of density ρ and speed v is (Warner, 1996 p.308)

$$P_{ram} = \rho v^2. \tag{1.2}$$

The speed at radius r should be close to the free-fall value $v_{ff} = (2GM_*/r)^{1/2}$, where $G = 6.67 \times 10^{-8}$dyn cm^{2}g^{-2} is the gravitational constant and M_* is the mass of the white dwarf. The density, $\rho(r)$, of the accreting material is related to the accretion rate ($\dot{M}$), the speed (v), and the cross-sectional area of the accretion stream (A), by the relation $\rho(r) = \dot{M}/(Av)$, so the problem here is to find a value for A. If the accretion is spherically symmetric then $A = 4\pi r^2$, whereas if the accretion is not spherical, say over a fraction f of the sphere at radius r about the white dwarf, then $A = 4\pi r^2 f$, giving $\rho(r) = \dot{M}/(4\pi r^2 v f)$.

Hence at R_m (using the free-fall speed),

$$\begin{aligned} P_{ram}(R_m) &= \frac{\dot{M}}{4\pi R_m^2 v f} v^2 \\ &\simeq \frac{\dot{M}}{4\pi R_m^2 f}\left(\frac{2GM_*}{R_m}\right)^{1/2} \\ &= \frac{\dot{M}(2GM_*)^{1/2}}{4\pi f R_m^{5/2}}; \end{aligned} \tag{1.3}$$

and equating this to P_{mag} at $r = R_m$ (equation 1.1) gives

$$\frac{(2GM_*)^{1/2}\dot{M}}{4\pi R_m^{5/2} f} = \frac{\mu^2}{8\pi R_m^6} \tag{1.4}$$

$$\begin{aligned} \text{so } R_m &= \left(\frac{\mu^2 f}{2(2GM_*)^{1/2}\dot{M}}\right)^{2/7} \\ &= 2^{-3/7}\mu^{4/7}(GM_*)^{-1/7}\dot{M}^{-2/7}f^{2/7}. \end{aligned} \tag{1.5}$$

For a non-magnetic system we require $R_m \lesssim R_*$, so an estimate for a limiting value of μ is

$$\mu^{4/7} \simeq 2^{3/7} R_* (GM_*)^{1/7} \dot{M}^{2/7} f^{-2/7} \tag{1.6}$$

$$\text{i.e. } \mu \simeq 2^{3/4} R_*^{7/4} (GM_*)^{1/4} \dot{M}^{1/2} f^{-1/2}. \tag{1.7}$$

The accretion rate is thought to be in the range $10^{16} - 10^{17}$ g s^{-1} (FKR92, p. 4), so choosing the lower extreme, and putting in values $M_* \simeq M_1 = 2 \times 10^{33}$ g, $R_* \sim 5 \times 10^8$ cm, we get

$$\begin{aligned} \mu &\sim 2^{3/4}(5\times 10^8)^{7/4}(6.67\times 10^{-8}\times 2\times 10^{33})^{1/4}(10^{16})^{1/2} f^{-1/2} \text{ gauss cm}^3 \\ &\simeq 10^{30} f^{-1/2} \text{ gauss cm}^3. \end{aligned} \tag{1.8}$$

Given plausible values for f of between 1.0 and 0.01, we get an estimate of

$$\mu \sim 10^{30} - 10^{31} \text{ gauss cm}^3 \tag{1.9}$$

as the limiting value. Translating into magnetic field strength at the white dwarf surface, this gives $B \sim \mu/(R_*)^3 \sim 10^4 - 10^5$ gauss as the limit for a non-magnetic system.

This gives a lower limit, but it could be argued further that for the field to affect the infall significantly, the threading should occur at some height above the white dwarf, say at $r \sim 5R_*$.

So, putting $R_m \sim 5R_*$ as the lower limit for magnetism, the magnetic moment should be greater than the amount calculated above by a factor of about $5^{7/4}$, roughly an order of magnitude, giving $\mu \sim 10^{31} - 10^{32}$ gauss cm^3 as the lower limit for the magnetic moment.

Those CVs which have shown evidence of magnetic fields due to polarization of the light have magnetic field strengths of about $10^7 - 10^8$ gauss, giving a magnetic moment of $\sim 10^{33} - 10^{34}$ gauss cm^3. However, these objects are mainly "polars" (discussed below), and the value for f in these systems is thought to be in the region of $\sim 10^{-4}$. This gives a value for R_m of about $2 - 6 \times 10^9$ cm, or 4 – 10 white dwarf radii.

1.3.2 Emission ranges for MCVs

The spectral range of the emission can be estimated (to order of magnitude) from accretion onto white dwarfs. The following analysis is derived from FKR92.

They initially consider the radiation to be a result of thermal bremsstrahlung, as the ionised material is braked near the surface. Assuming the material is dominated by ionised hydrogen, the potential energy released by each proton-electron pair is

$$E_{pe} = GM_*(m_e + m_p)/R_* \simeq GM_*m_p/R_*, \tag{1.10}$$

where G is the gravitational constant, M_* is the mass of the white dwarf, R_* is the white dwarf radius, and m_e, m_p are the masses of the electron and proton respectively. Since $m_p >> m_e$ the above approximation is valid. The thermal energy is given by $2 \times \frac{3}{2}kT$, where $k = 1.38 \times 10^{-16}$erg K^{-1} is the Boltzmann constant and T is the temperature. Hence the thermal temperature is

$$T_{th} = GM_*m_p/(3kR_*). \tag{1.11}$$

This would apply if the emission were optically thin, i.e. with little absorption. In the optically thick case, the radiation is absorbed, and reaches thermal equilibrium with the absorbing material. The radiation will eventually leak out, but now the spectrum approaches that of a blackbody. To find the blackbody temperature, we first need to consider the "accretion luminosity", L_{acc}, which is the rate at which the infall energy is radiated. This is given by

$$L_{acc} = GM_*\dot{M}/R_*, \tag{1.12}$$

where $\dot{M}$ is the rate at which material accretes. In the white dwarf case, L_{acc} is of the order of 10^{33} erg s^{-1}.

From classical thermodynamics, the temperature is given by

$$T_b = (L_{acc}/4\pi R_*^2\sigma)^{1/4}, \tag{1.13}$$

where $\sigma = 5.7 \times 10^{-5}$erg cm^{-2}K^{-4}s^{-1} is Stephan's constant.

Now the system cannot radiate at lower than the blackbody temperature (FKR92, p. 5), hence $T_b \leq T_{th}$. Since the system is expected to lie somewhere between perfectly optically thin and optically thick, we expect the actual radiation temperature, T_{rad}, to lie between the blackbody and thermal temperatures, so

$$T_b \leq T_{rad} \leq T_{th}. \tag{1.14}$$

Applying these limits to a white dwarf, and putting in values $M_* \sim 2 \times 10^{33}$g, $R_* \sim 5 \times 10^8$ cm, and $m_p = 1.67 \times 10^{-24}$g, we have

$$\begin{aligned} T_b &\sim (2 \times 10^{33}/(4\pi \times 10^{18} \times 5.7 \times 10^{-5}))^{1/4}\text{K} \\ &\sim 3 \times 10^4\,\text{K}, \end{aligned} \tag{1.15}$$

$$\begin{aligned} T_{th} &\sim \frac{6.67 \times 10^{-8} \times 2 \times 10^{33} \times 1.67 \times 10^{-24}}{3 \times 1.38 \times 10^{-16} \times 5 \times 10^8}\text{K} \\ &\sim 3 \times 10^8\,\text{K}. \end{aligned} \tag{1.16}$$

Hence 10^5 K$\lesssim T_{rad} \lesssim 10^9$ K. The average frequency of the radiation, $\bar{\nu}$, could be obtained (to order of magnitude) using the relation $kT_{rad} = h\bar{\nu}$, where $h = 6.6 \times 10^{-27}$ ergs is Planck's constant. In terms of photon energy the spectral range is

$$8\,\text{eV} \lesssim h\bar{\nu} \lesssim 100\,\text{keV}, \tag{1.17}$$

the upper limit to an order of magnitude. This range extends from the ultraviolet, to the X-ray band (> 0.1 keV).

1.3.3 Polars

The magnetic systems (MCVs) include *polars* (or AM Her systems) and *intermediate polars*, which differ from the polars in the degree of synchronization of the primary's spin period with the system orbital period. In the polars the white dwarf spin period is synchronised with the system orbital period, so that the white dwarf presents the same hemisphere to the secondary. This phase-locking is assumed to be caused by the white dwarf's strong magnetic field, and its magnetostatic interaction with an intrinsic field on the secondary. This interaction provides a torque sufficient to balance the accretion torque (Lamb & Melia 1989).

In polars there is no evidence for accretion discs, and the accreting material proceeds in a stream from the L1 point in a Keplerian orbit, until the magnetic pressure exceeds the ram pressure of the stream. At this point the material "threads" onto the magnetic field lines, and its subsequent trajectory follows the field down to a spot close to the nearer magnetic pole.

The terms *polar* and *intermediate polar* appear to have been originated by Krzeminski (1977) during his study of the cataclysmic variable AM Herculis. This system was studied in the optical and ultra-violet and in 1977 significant polarization was observed, which was interpreted by Krzeminski as an indicator of a strong magnetic field. He suggested the name "polar" to denote those magnetic CVs which had synchronised spin and orbital periods, and proposed that unsynchronised magnetic CVs (then unconfirmed by polarization data) should be termed "intermediate polars". Evidence of polarization in unsynchronised MCVs was first obtained in 1986 with observations of BG Canis Minoris (Penning, Schmidt and Liebert 1986), and later of RE 0751+144 (Piirola, Hakala and Coyne 1993).

1.3.4 Intermediate polars

In intermediate polars the white dwarf spin period and the system orbital period are different. In this document the expressions p_{spin}, p_{orb} and p_{beat} are used to symbolise these periods. They are related by

$$1/p_{beat} = 1/p_{spin} - 1/p_{orb}. \tag{1.18}$$

Most models assume that the magnetic field is not strong enough to synchronise the periods,

although there is some speculation that there is a resonance at a ratio of p_{spin}:$p_{orb} \sim 0.1$, when small increases or decreases in p_{spin} result in the white dwarf losing or gaining angular momentum respectively, so giving an equilibrium. (See Hameury, King & Lasota, 1986). Other researchers, e.g. Patterson (1994), do not consider the evidence of this resonance to be convincing, however.

The X-ray flux from intermediate polars shows modulations at various periods, including the white dwarf spin period (typically about 10 – 20 minutes), the orbital period (about 3 – 4 hours), and the beat period, which is defined as the spin period of the primary relative to the orbital frame.

Recent comprehensive reviews of intermediate polars (IPs) are given by Patterson (1994) and Hellier (1996). Patterson considers intermediate polars and the class *DQ Hers* (named after the prototype DQ Herculis) to be equivalent, although some researchers (for instance the aforementioned Warner, p. 412) consider that the latter constitute a subset of the IPs, the distinguishing feature being their lack of hard X-ray emission. This is also discussed in Warner and Wickramasinghe (1991). The existence (or not) of the p_{spin}:p_{orb} resonance mentioned above depends on whether this distinction is genuine. In this thesis I use Warner's criterion, since the model discussed is designed to simulate the X-ray flux only.

See Table 1.1 for a list of known IPs and their periods. Table 1.2 gives a similar list of possible IPs. For some of these, evidence is available to provide a basis for a reasonable estimate of the inclination angle. These are listed in Table 1.3.

Some early work on the theory of the accretion near the white dwarf surface was done by Fabian, Pringle and Rees (1976), in which it was argued that the infall would create a stand-off shock above the surface of the white dwarf, with a height $\sim 10^7$ cm, in which the material reaches temperatures of $\sim 10^8$ K. The X-ray flux emanates from this region. (See figure 1.2.)

X-ray spectra and lightcurves of intermediate polars are discussed fully in Chapter 2.

1.4 The theory of magnetic cataclysmic variables

1.4.1 Accretion theory

Matter can accrete onto the white dwarf by various methods. One way, which is not thought to be too significant in magnetic CVs, is via a *stellar wind*, where material is blown off the companion star by its own radiation pressure, and a proportion of this doesn't escape the system but is trapped by the white dwarf's gravitational field. This accretion could rain on the white dwarf from any angle, but would eventually be constrained by the magnetic field.

The most important accretion method, however, is by *Roche-lobe overflow* (described in section 1.1). In this case, the material will accrete in a stream from the inner Lagrangian point (the L1 point), preferentially in the orbital plane of the two systems (see Lubow and Shu 1975). This is a simple consequence of orbital dynamics.

The stream may self-interact as it rounds the white dwarf, and in some cases forms an accretion disc, which lies close to the orbital plane. (It may be tilted slightly, in which case it would "precess" as a result of the torque from the companion star.) If this happens, when the disc has stabilised the stream impacts the outer edge, resulting in a "hot-spot", with a bulge of matter heated by the dumping of kinetic energy into the disc. (See figure 1.6.) At this point, material from the impact may be thrown out of the orbital plane, with observational consequences described below. The disc is in a state of quasi dynamic equilibrium, with material slowly spiralling inwards (although the azimuthal speed is Keplerian) towards the disc's inner edge (at the magnetic radius in MCVs) and eventually onto the white dwarf. The disc is replenished by the stream from the L1 point.

In some cases the disc will not form. This is believed to be the case in all polars, as the magnetic field is strong enough to affect the stream at radii comparable to the distance of the L1 point (from the white dwarf). The material accretes in a narrow stream and threads on to the magnetic field lines almost as soon as it leaves the L1 point, hitting the white dwarf close to a magnetic pole. The situation is depicted in figure 1.3, and this scenario is fixed in the orbital frame.

The situation with intermediate polars, on the other hand, is less clear. A truncated disc was the usual model until the mid 1980s, with a disc forming (Lubow and Shu, 1976), but Hameury, King and Lasota (1987) argued that the majority of IPs would have no disc, and

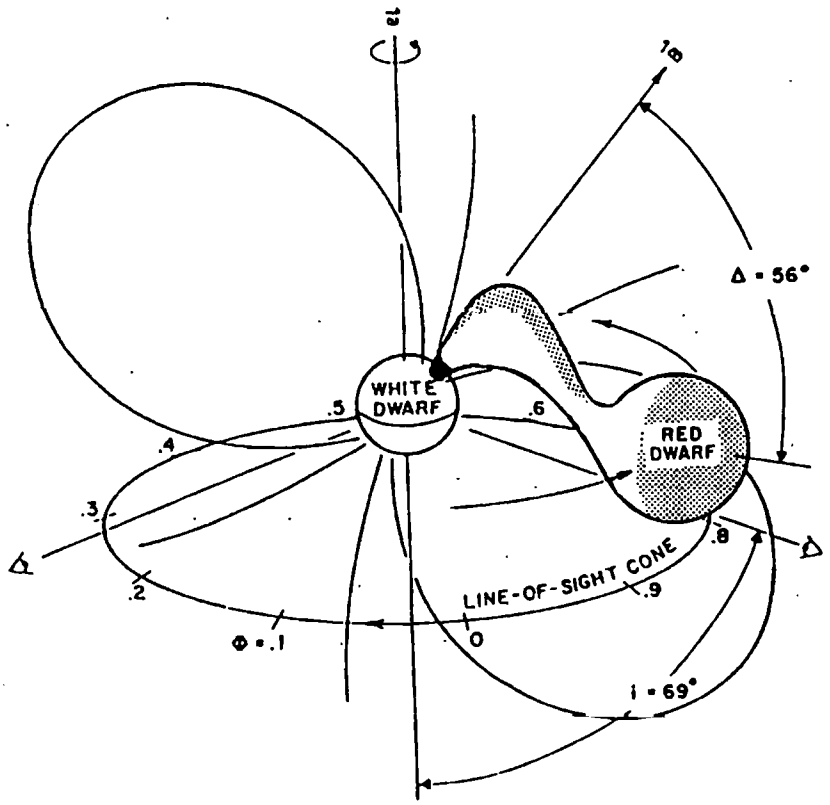

Figure 1.3: Accretion of material in a polar

gave a detailed mathematical analysis that constrained conditions which would allow a disc to form. Hellier (1991), though, has produced evidence for the existence of discs in some IPs.

Since there is evidence both for systems accreting via a disc and for those accreting directly via a stream, material accreting via Roche-lobe overflow may be said to have two main modes of accretion: *disc-fed* and *stream-fed.*

If a disc is present, it does not necessarily mean that accretion is wholly via the disc: part of the stream may skim over the disc and fall directly to the point where it threads onto the magnetic field. This is often called a "disc-overflow" mechanism (Lubow, 1989), although if the proportion of disc-fed material is small it may be referred to as a "non-accretion disc".

The accretion is thought to occur at regions around all magnetic poles, due to the accreting plasma threading onto the field lines (figure 1.4).

The study of intermediate polars from the 1970s to the mid 1980s modelled the accretion

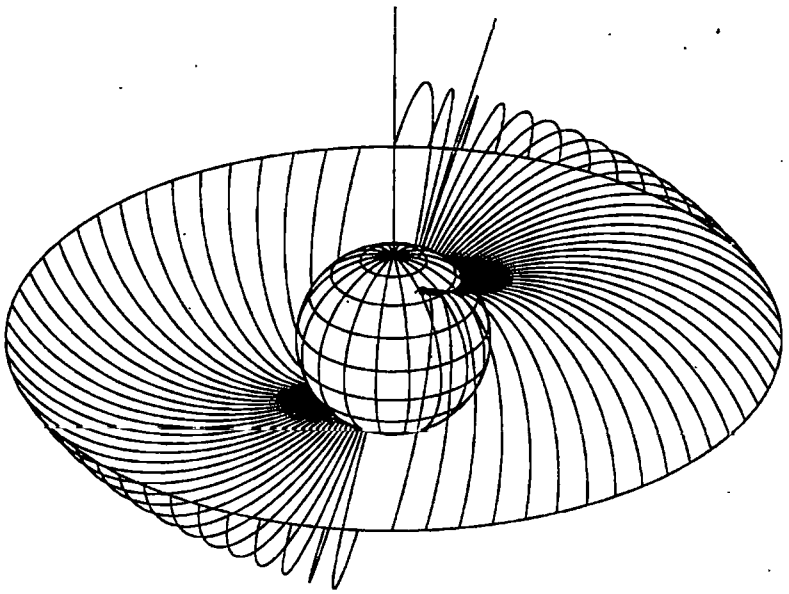

Figure 1.4: Accretion arc from disc inner edge to white dwarf surface

column as a circular cylinder. Fabian *et al.* (1976) and King & Shaviv (1984) calculate the absorption at various angles of elevation on the assumption that the cylinder is filled, giving rise to a filled-circle accretion region; FKR92 note that the cylinder may be hollow as the material follows the field lines, the accreting region therefore being a hollow circle. This has been largely replaced since around 1987 by assuming that the accretion column is guided by the magnetic field to form an "accretion curtain", arc-shaped in cross-section, which therefore forms an arc-shaped "footprint" (see figure 1.4), rather than a filled or hollow circle. (See Rosen, Mason and Córdova 1988.) This needs to be considered in any simulation, and is considered in more detail in Chapter 4.

The accretion itself may be clumpy rather than a steady stream, with varying sized blobs overflowing L1. This may also apply to the attachment of material to field lines at the inner edge of the disc (if present). See, for example, Frank, King & Lasota (1988), or King (1993).

1.4.2 Conditions for disc formation

As the material overflows throught the L1 point, FKR92 calculate its speed to be of the order of $100\,\mathrm{km\,s^{-1}}$, whereas the speed of sound in the plasma is $\sim 10\,\mathrm{km\,s^{-1}}$, hence the flow is highly supersonic, which means that pressure forces can be neglected in calculating the subsequent trajectory. Thus, as a first approximation, this allows us to consider the accretion as consisting of individual cells undergoing a ballistic orbit. These will carry a large amount of angular momentum, due to the orbital speed at L1. In the case of a (non-magnetic) compact accreting star the material will then orbit the star in a Keplerian ellipse. (For non-compact stars the stream could splash directly on to the star, thus never making it round to form a disc.) The next refinement to this model is then to consider what happens when the stream rounds the star and self-interacts. Friction and viscosity will result in the material dissipating energy, in the form of heat. Its angular momentum cannot be dissipated in the same timescale, so the material then tends to assume the lowest energy configuration for the initial angular momentum – a circular ring. This will be at the corresponding Keplerian radius for the initial angular momemtum, R_{circ}. The material will still be losing energy though dissipative forces, and again, on these timescales, the loss of angular momentum is insufficient to allow the material simply to spiral inwards with no other effects. In fact there is a transfer of angular momentum through viscosity from lower radii to higher radii, resulting in the ring extending in both directions, inwards and outwards, forming the disc. Ultimately as the disc reaches its steady state, the accreting material hits this at its outer point, creating the hotspot, and the disc itself transfers its angular momentum to the secondary by tidal effects.

As alluded to in the previous paragraph, one condition for the above process to occur is that the minimum radius of the Keplerian orbit of the material (R_{min}) should be greater than the radius of the primary. When magnetic fields are taken into account, a further condition is necessary: R_{min} should be greater than R_{mag}, the latter depending on the magnetic dipole moment and the ram pressure.

1.4.3 Estimates of R_{mag}

It is widely accepted that the inner radius of the truncated disc is difficult to calculate, depending as it does on the relative values of magnetic pressure and ram pressure, with the

latter being dependent on the material density, and the former being affected by possible disortions of the magnetic field by the plasma. Therefore the theoretical calculations are usually expressed as order of magnitude.

FKR92 give a formula for this radius:

$$R_{mag} = 5.1 \times 10^8 \dot{M}_{16}^{-2/7} M_1^{-1/7} \mu_{30}^{4/7} \text{ cm}, \tag{1.19}$$

however this is based on the density being given by $|\rho v| = \dot{M}/4\pi r^2$, which is true for spherically symmetric accretion, and would not be valid for a disc.

Lamb(1988) gives an alternative formula for the inner disc radius, based on the assumption of disc accretion:

$$R_{mag} \sim 0.5 \mu_1^{4/7} (2GM_1)^{-1/7} \dot{M}_1^{-2/7} \tag{1.20}$$

where the symbols represent the c.g.s. values. Putting $M_1 = 10^{33} M_*$ (taking the primary mass to be half a solar mass), $\mu_1 = 10^{33} \mu_{33}$, and $\dot{M}_1 = 10^{17} \dot{M}_{17}$,

$$\begin{aligned} (2GM_1)^{-1/7} &= (13.4 \times 10^{35} M_*)^{-1/7} \\ &= 1.85 \times 10^{-4} M_*^{-1/7}, \qquad (1.21) \\ \text{so } R_{mag} &= 9.3 \times 10^9 \dot{M}_{17}^{-2/7} M_*^{-1/7} \mu_{33}^{4/7} \text{ cm}. \qquad (1.22) \end{aligned}$$

Now, if $\dot{M}_{17} \approx 1.0$, and $M_* \approx 0.5$, R_{mag} expressed as a function of μ_{33} is

$$\begin{aligned} R_{mag}(\mu_{33}) &\approx 1.0 \times 10^{10} \mu_{33}^{4/7} \text{ cm} \\ &\approx 20 R_* \mu_{33}^{4/7} \qquad (1.23) \end{aligned}$$

(assuming $R_* = 5.0 \times 10^8$ cm).

So varying μ_1 from 10^{32} G cm^3 to 10^{34} G cm^3 by factors of ten, μ_{33} varies from 0.1 to 10.0, giving

$$R_{mag}(0.1) \approx 5.4 R_*, \tag{1.24}$$

$$R_{mag}(1.0) \approx 20 R_*, \tag{1.25}$$

$$R_{mag}(10.0) \approx 75 R_*. \tag{1.26}$$

From this, it seems that the inner radius can vary from $5R_*$ to $20R_*$ as the magnetic moment varies up to 10^{33} G cm^3, but for field strengths above this disc formation seems increasingly unlikely.

1.4.4 Angular momentum and $\dot{P}_{spin}$

The spin period in some systems has been observed to increase or decrease, and accretion theory should provide a plausible mechanism for this effect. When the material flows through the L1 point it has a large angular momentum of which most must eventually be lost for it to accrete. For disc-fed accretion, the material is assumed to be rotating at Keplerian speeds, hence the critical radius is the *corotation* radius, r_{co}, given by

$$r_{co} = \left(\frac{GM_*}{\omega^2}\right)^{1/3}, \tag{1.27}$$

where $\omega = 1/p_{spin}$. (Warner 1995, p374). Thus attachment at $r < r_{co}$ acts to speed up the primary. Warner points out that steady accretion along field lines can only occur for attachment at $r < r_{co}$.

For stream-fed accretion only, the magnetic field is too strong to allow formation of a disc, and (particularly for small p_{orb}, i.e. small separation) the interaction of the primary's field with the secondary may have a braking torque exceeding any positive accretion torque, leading to negative $\dot{P}_{spin}$.

1.4.5 Origins of X-ray modulation

As noted in section 1.3.4 the X-ray signals from IPs can show modulations at various periods, and here we discuss the causes of these in light of the theory.

Spin-period modulation. This effect may be caused by occultation of the accretion zone and obscuration of the radiation due to absorption by infalling material, both of which will vary with the spin phase. This absorption will have two components (assuming the material to be a plasma): electron scattering and photoelectric absorption. The latter effect is energy dependent (absorption roughly $\propto E^{-3}$), hence a significant absorption contribution should show up as a systematic decrease in modulation depth as the energy window increases.

This relation between photon energy and modulation depth had not been detected before about 1988, hence King and Shaviv (1984) considered absorption to be insignificant. Thus the model developed by these researchers had self-occultation as the cause of modulation, and they used this to argue for a large accretion area ($\sim 0.25 \times$ the white dwarf surface area), using statistical analyses of the light curves from various systems, and comparing the

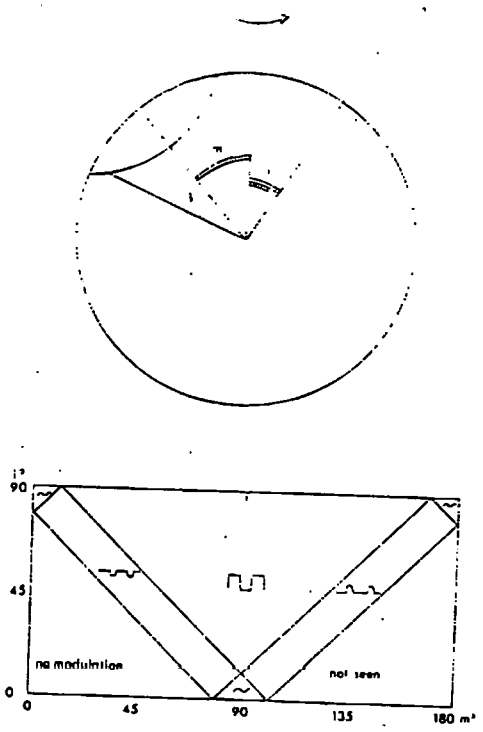

Figure 1.5: Hard X-ray light-curve shapes as a function of the angles i and m for $\beta = 11.5°$ ($f = 10^{-2}$). (From King & Shaviv, 1984).

frequency of occurrence of the various shapes to that predicted by their model. Also, to avoid absorption effects, the accretion column would need to be optically thin.

Figure 1.5 shows one of their predictions, in various ranges of inclination (i) and magnetic colatitudes (m). The angle β is the half-angle subtended by the accreting area at the white dwarf centre. The figure shows regions in $i - m$ space in which their model predicts pulse profiles of square-wave shapes, sinusoids, and no modulations.

However, Norton and Watson (1989), along with others including Rosen, Mason and Córdova (1988), used data from the *EXOSAT* mission to reveal evidence for energy dependent modulation, and argued for a significant absorption contribution to the modulation. (See figure 1.7.) This is a feature now known to be common to most intermediate polars.

One consequence of this is that, unlike the occultation only model, completely symmetric poles can still lead to a spin modulation. This is because the upper pole peaks in brightness

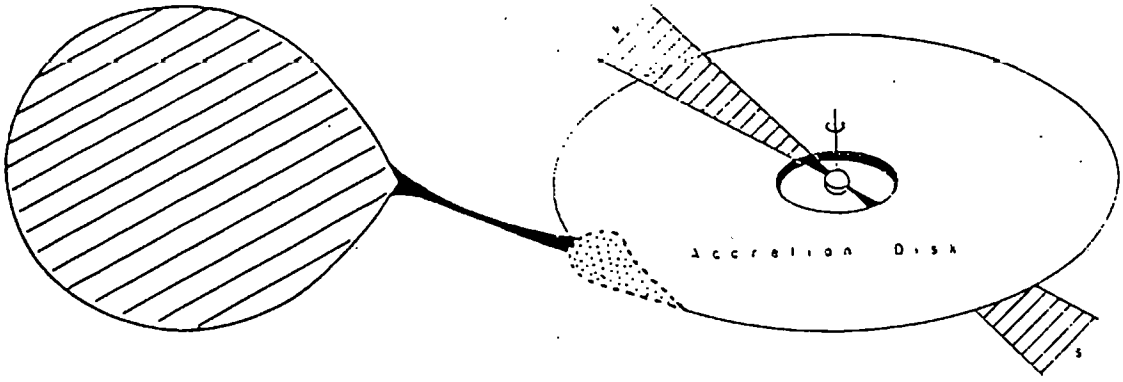

Figure 1.6: Schematic of the binary system with truncated disc

when the spin takes it away from the observer, when the line of sight from the bright region is through the side of the curtain; while when the pole is on the near side the line of sight is down the column, giving an increase in optical depth, resulting in the minimum observed X-ray brightness. The lower pole, on the other hand, would have a minimum when it is occulted, and this is in phase with the upper pole minimum.

A further contribution to the modulation at the spin period may be eclipsing of the emitting regions by the secondary (unlikely) or more likely by the inner edge of the accretion disc assumed to be present. This would only be expected for systems with a high inclination angle, and should only affect emission regions below the white dwarf equator (relative to the observer) as the lower pole is periodically eclipsed at the spin period.

Beat-period modulation. In IPs, the asynchronous spin and orbital periods means that the face of the white dwarf presented towards the secondary star changes continuously, going through a whole cycle at the beat frequency. Consequently, the magnetic poles (if they are offset from the spin axis) will at various times during the beat period point towards and

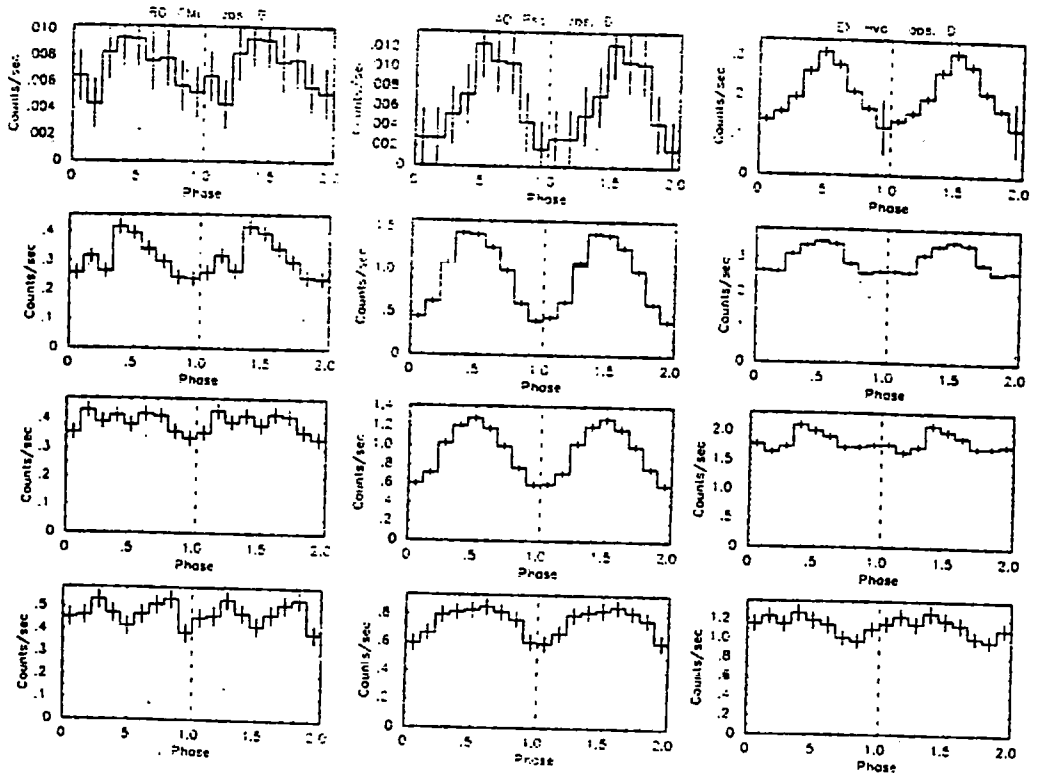

Figure 1.7: Various spin pulse profiles (From Norton & Watson 1989).

away from the secondary. If the white dwarf's field is a dipole, then one pole will be nearer the secondary for half the beat period, the other will then be nearer for the other half. Also the angle at which the stream hits the magnetic field lines is expected to have an effect on the proportion of material going to each pole. Therefore, if there is a substantial stream-fed component of accretion, the stream-fed material would accrete preferentially to one pole or the other depending on the beat phase, hence a beat would be detectable. Currently there is no complete solution to the general magnetohydrodynamic problem of the interaction of the stream (or the disc) with the magnetic field, but models have been tried with the stream "flipping" from one pole to the other, successive "flips" occurring at intervals of half a beat period. (Other models assume that the proportion of the stream threading onto each pole varies more smoothly, for example as a sinusoid; e.g. see Kim and Beuermann, 1995). Thus the footprints of the stream-fed region around each pole would brighten and darken alternatively with a cycle length equal to the beat period. Since observations of the system would normally be at an angle to the orbital plane, one pole would be more visible than the other, so the varying brightness of the more visible pole should be detectable as a

modulation in the signal.

If accretion is entirely through a disc, however, it should lose any information regarding the beat phase, hence the existence of a beat signal is usually considered an indicator of a stream-fed component. Since these are often found, sometimes when evidence of a disc is also present, current models allow for the possibility of the disc-overflow mechanism mentioned above.

Orbital modulation. Modulation at the orbital period may be caused by the light passing through an absorber fixed in the orbital frame, for instance a cloud of plasma thrown up above the disc plane at the "hotspot" where the stream meets the disc (as described above). A similar effect may occur in discless models, if the line of sight passes through the stream at the same phase in each orbit. The requirements for this to happen are that the inclination angle be high enough, and the absorber be dense enough to cause significant attenuation of the flux. In the actual data, these effects can show up as a dip in the light curve and a dip in the orbital fold. (Examples of this will be presented in Chapter 3 for two specific systems).

A modulation at the orbital period may also be present as a result of the interaction between the spin and beat signals as discussed in Norton, Beardmore and Taylor (1996). Calling the spin frequency ω_s, the orbital frequency ω_o, and the beat frequency $\omega_b = \omega_s - \omega_o$, the power spectrum may show modulations at the sidebands $m\omega_s + n\omega_b$, for integers m and n. In particular with $m = 1$, $n = -1$ we get a signal at the frequency $\omega_s - \omega_b = \omega_o$. (In subsequent chapters the spin and orbital frequencies are labelled ω and Ω for consistency with referenced papers. The beat frequency is then simply $\omega - \Omega$.)

1.4.6 Unsolved problems in intermediate polars

Evolutionary scenarios. It is of interest to find the precursors of polars and intermediate polars, and how they evolve from their current state. At one time it was thought that intermediate polars would eventually become phase-locked, thereby being the precursors of polars; this is no longer considered to be a likely scenario, the difference being the magnetic field strengths.

Mode of accretion. This, the relative amount accreted by disc or by stream, is a highly important factor in modelling the behaviour of these objects. Apart from the strength

of the various pulses (beat pulse c.f. spin pulse), there is the method by which angular momentum is eventually dumped on to the white dwarf, which has implications as to stable spin periods.

Asymmetry in the spin pulse profile. Although the majority of intermediate polars have spin pulse profiles which are roughly sinusoidal, a few, notably FO Aqr, have a distinctively asymmetric spin profile, so models explaining the source of modulations have to be able explain both the symmetry and the asymmetry in different systems. This is addressed in more detail in Chapter 4.

Covering fraction. Since it is now believed that partial covering is necessary to explain the modulation depths, the determination of the covering fraction in the various systems is a target of investigation.

Selection effects. The study by King & Shaviv (1984) made the point that, using the occultation only model, intermediate polars would be undetectable with certain system parameters. For example, if the system had a perfectly symmetrical dipole the effects of each pole would cancel each other out. Also if the inclination angle was close to 0° there would be no occultation of the emission region, so no modulation. With the occulation/absorption model, and with arc-shaped curtains, the former cancellation would no longer apply. However, it is still possible to conceive of system parameters whereby we would not receive a modulated signal, in which case it would not be detected as an intermediate polar. One of the program tests will be to identify the parameters which give this effect, from which a statistical estimate can be made of how many of these "invisible" systems there may be.

1.5 The computer model

The computer model used to simulate the IPs has evolved from an original idea by J. R. E. Brooker of Leicester University in 1985. A detailed description of the parameters used, with reference to current accretion models, is given by Norton (1993). I reproduce at this stage an overview of the current working of the program, with comments on alterations since 1993. A more detailed description of the program is given in Chapter 4.

1.5.1 The basic simulation method

The simulation is based on the assumption that the major contribution to the absorption is from the accretion column just above the stand-off shock, which is where the X-ray emission occurs. Using Fabian *et al.* (1976), an estimate of the linear extent of the bright area over the white dwarf surface is $\sim 10^8$ cm, and its height above the surface $\sim 10^7$ cm. So we imagine the bright region to be a two-dimensional region "painted" on the white dwarf surface, i.e. ignore the effects of its height. Then the cooler column above the shock acts purely as an absorber.

To justify the estimate of shock height, which is important for the simulation method, we note that FKR92 calculate an upper limit for it, by considering the time for the plasma to cool from immediate post-shock temperatures to the primary's surface temperature. Using radiation cooling alone, they derive the height:

$$D_{rad} \sim 9 \times 10^8 \dot{M}_{16}^{-1} f_{-2} M_1^{3/2} R_9^{1/2} \,\mathrm{cm}, \tag{1.28}$$

which is their equation 6.44. If we make plausible assumptions for the values here, for example $\dot{M}_{16} \simeq 10$, $f_{-2} \sim 1$, $M_1^{3/2} \simeq 0.5^{3/2} = 0.354$, and $R_9^{1/2} \simeq 0.707$, we obtain $D_{rad} \sim 2.25 \times 10^7$ cm. Thus, if other cooling processes are present, a shock height $\sim 10^7$ cm seems plausible.

As described in Norton (1993), the program defines small cells within the accreting area, and for each of these calculates the flux and the attenuation through the accretion column in the line of sight to the observer. The attenuation is calculated using the assumption of photoelectric absorption and electron scattering. This procedure is carried out for a particular timestep (from which the orientation of the accretion region and column to the observer can be calculated). The flux after attenuation is summed over all the visible (non-occulted) cells. This process is repeated over many timesteps, and output to a file, together with the pulse profiles at the various periods. The number of timesteps should be chosen to cover several orbital cycles in order to obtain useful pulse profiles.

The parameters used in the simulations may be considered to fall into two broad classes, intrinsic and runtime. The former are those which are intrinsic to an individual system, such as the spin and orbital periods, white dwarf mass, accretion rate and so on. The inclination angle is not strictly speaking intrinsic to the system itself as it depends on the orientation relative to the observer, but it is included here since it is a constant for any particular IP

we observe. In general, few of these are known for any particular system; the more obvious known ones being the spin (or beat) and orbital periods (but see note to BG CMi in table 1.1). Sometimes eclipse data allow an estimate for the inclination angle.

Runtime parameters include timestep size, length of run, size of cells, and photon energy. This last is a single value, in keV, giving the simulated energy "window" of the telescope, although in a real instrument it would be an energy range with a variable response. A complete list of parameters, from both the original version and the updated version, is given in Chapter 4.

In the simulation a dipole is assumed, either symmetrically placed through the centre of the primary, or offset, latitudinally and/or azimuthally. The geometry of the accretion regions on the surface of the white dwarf may differ markedly between the two accretion modes, and our simulation allows the proportion of disc-fed and stream-fed accretion to vary between the two extremes, disc-fed only and stream-fed only.

1.5.2 Alterations in brief

Since 1993 the program has been altered in various ways to try to get the simulation more in line with current theory. For example, the distribution of the stream-overflow between the poles was assumed to depend on the angle of the white dwarf axis and the line joining the two stars in the original simulation. The rate was varied sinusoidally, with the maximum (to the upper pole say) occurring when this pole pointed towards the secondary. This has now been altered so that the distribution depends on the angle at which the stream encounters the field lines at the magnetic capture radius (i.e. where connection occurs). (The user now has the option to allow this distribution to be sinusoidal, or sharper, for instance flipping from pole to pole.)

Another alteration to the simulation has been to allow for multiple density components and partial covering, which seems to be necessary to explain spectral data (Norton & Watson 1989).

A major amendment has been to include the variation in optical depth (in the accretion curtain) in different horizontal directions. In this context, "horizontal" means parallel to the white dwarf surface, and "vertical" means radial to the white dwarf, so would be be up

the accretion column. Previously only the vertical and a single horizontal depth (τ_h) was used (based on Fabian *et al.* (1976) and King & Shaviv (1984), both of which assumed a cylindrical accretion column). The vertical optical depth in these works, τ_v, was calculated by integrating from the white dwarf surface up the column to infinity, assuming that the density of the stream varies as $R^{-5/2}$ (the dipole approximation, R being the radial distance of a stream element from the white dwarf centre). The simulation program then used these to calculate the optical depth at various angles to the horizontal by the formula

$$\tau = \tau_h \cos^2 \mu + \tau_v \sin^2 \mu, \tag{1.29}$$

where μ is the elevation of the line of sight to the horizontal.

An alternative formula, used by Wynn and King (1992) and expressed in the above notation, is

$$\tau = \tau_h(1 - |\cos \mu|) + \tau_v |\cos \mu|. \tag{1.30}$$

As I show in Chapter 4, again assuming the dipole approximation, neither of the above formulae gives the optical depth accurately.

The changes to the program include a different approach to the calculation of optical depth; altering the method of splitting the stream-fed accretion between the poles; inclusion of the lower pole azimuthal lag parameter; defining the accretion envelope area by reference to magnetic capture radii and colatitudes; allowing the option of partial covering and multiple column densities; and refinement to the extra orbital N_H density parameters, in light of recent observations. These are described in detail in Chapter 4.

The amended program now allows the option to vary τ_h in different directions, on the assumption that the curtain is arc-shaped, by calculating the distance through the curtain from an emitting cell along the line of sight.

1.5.3 Applications to unsolved problems

Ultimately it is hoped to obtain parameters which give simulated lightcurves and profiles matching those from actual observations. One problem may be that with sinusoidal profiles there may be some degeneracy, with different parameter sets providing matches. Thus the more irregular systems may provide better targets. Attempting to model FO Aqr at different

epochs using plausible parameter changes is another approach: this highly interesting system is known to undergo changes in profile at different epochs, which may indicate different stream/disc-fed ratios, and alterations in accretion rate. Beardmore et al (1997) present a recent exploration of this system over the period 1983 – 1993.

More general uses may be to test ideas in modelling intermediate polars. For example if it were found that using full covering, and a single column density, the dependence of spin pulse modulation depth with energy did not correspond with observations, this would be support the idea that partial covering and/or multiple column densities are necessary.

As noted earlier, tests should include ranges of parameters in which modulations are barely detectable, and so estimate what proportion of intermediate polars would not be detectable due to these selection effects. It is plausible to argue, for instance, that an inclination angle of around zero would not result in any modulation at any of the spin periods.

1.6 Forward look

In the rest of the thesis: Chapter 2 describes the X-ray signals received from several IPs (and the limitations of the instruments used). Chapter 3 is a more detailed look at two specific IPs, AO Psc and V1223 Sgr, using recent *Ginga* and *ROSAT* data. Chapter 4 is a detailed look at the computer program and alterations in light of theoretical advances, and Chapter 5 presents some results. The final chapter summarises the work and discusses future work using this model.

Table 1.1: Periods of intermediate polars

System	X-ray name	P_{spin}/s[a]	P_{orb}/hr[a]	P_{beat}/s[a]	References
XY Ari	1H 0253+193	206.298(X)	6.06480(XE)		[3][7]
	RX J0558+53	545(P,H)	4.1 (S)		[6]
V709 Cas	RX J0028+59	313(X)	5.4(X)		[3]
GK Per	A 0327+43	351.34(O,X)	47.92327(S)		[3]
YY Dra	2A 1150+72	529.22	3.96		[3]
V405 Aur	RX J0558+54	545.455	4.15		[3]
	RX J1914+24	567.7(X)			[3]
V1223 Sgr	4U 1849-31	745.8(O,X)	3.365856(X)	794.38(O)	[3][11]
AO Psc	H2252-035	805.20(P,S,X)	3.591024(O,X)	858.69(O)	[3]
PQ Gem	RE J0751+14	833.40(X,O)	5.179(O)	872.30(O)	[3]
UU Col	RX J0152-32	863.5	3.45		[3]
BG CMi	3A 0729+103	847.03[b](P,S,X)	3.233976(O,X)	913.50[b](X)	[3]
	RX J1712-24	927.66(PL)	3.41	1003.6(P)	[3][4][12]
FO Aqr	H2215-086	1254.45(P,S,X)	4.84944(O)	1351.57(X)	[14][3]
	RX J0153+74	1414(X)			[4]
WX Pyx	1E 08309-2238	1503.7(P)	6–9.6(P,S)	1557.5	[8][3]
TV Col	2A 0526-328	1910. (X)	5.486400(E)		[3]
TX Col	H0542-407	1911. (X,O)	5.7192(S)	2106(P,X)	[9]
V1062 Tau	1H 0459+248	3726	9.952	3794	[5][3]
EX Hya	4U 1228-29	4021.62(P,S,X)	1.637616(O,X)		[3]
AE Aqr		33.0767335(O,X)	9.87873(O)		[1]
V533 Her		63.63(O)	5.035(O)		[2]
DQ Her		142[c](P)	4.646909(E)		[1][10]

The two sets are IPs and DQ Hers respectively.

[a] Precision as given in source

[b] There is some doubt as to which of these is which (Norton et al, 1992).

[c] Previously thought to be 71s

References:

[1] Patterson (1994)
[2] Ishida (1991)
[3] Ritter (1997)
[4] Motch & Haberl (1995)
[5] Warner (1996)
[6] Allan et al (1996a)
[7] Koyama et al (1991)
[8] O'Donoghue, Koen & Kilkenny (1996)
[9] Norton et al (1997)
[10] Zhang et al (1995)
[11] Norton et al (1996)
[12] Buckley et al (1995)
[13] Patterson & Moulden (1993)
[14] De Martino, Buckley, Mouchet & Mukai (1994)

Key to types of observations:

O: Optical
P: Optical photometry
S: Optical spectroscopy
PL: Polarimetry
X: X-rays
H: Hard X-rays
XE: X-ray eclipse
E: Eclipse

Table 1.2: Periods of possible intermediate polars

System	X-ray name	P_{spin}/s[a]	P_{orb}/hr[a]	P_{beat}/s[a]	References
	H0551-819	600-2400	3.34		
V348 Pup	H0709-360	$\sim P_{orb}$?	2.44		
V795 Her	PG1711-336	1140	2.6		
TT Ari		$\sim$ 1200	3.3		
VZ Pyx	H0857-242	2918	1.78	2925	[1]
V426 Oph		3600	6.8		[1]
V603 Aql	N.Aql 1918	$\sim$ 3780	3.3		
KO Vel	1E 1013-477	4086.	10.13	5330	[1]
	N.Aql 1995	$\sim$ 5189	6.1		
TW Pic	H0534-581	7560.	6.060(P)	7186	[1][2]
V347 Pup	4U 0608-49				
HZ Pup					

References:

[1] Ritter (1997)

[2] Patterson & Moulden (1993)

Table 1.3: Estimates of i for selected IPs

System	X-ray name	Inclination angle /°	Evidence
DQ Her		$\simeq 90$	Optical eclipse[1]
XY Ari	1H 0253+193	80–87	Eclipse data[2]
GK Per	A 0327+43	46–73	Lack of eclipse [3]
YY Dra	2A 1150+72	41–42	[4]
V1223 Sgr	4U 1849-31	15–27[a]	[5]
		~ 80	grazing orbital dip[6]
AO Psc	H2252-035	60	X-ray orbital dip, no Eclipse[7]
PQ Gem	RE J0751+14	Low?	No orbital modulation[8]
BG CMi	3A 0729+103	65 ± 10	Grazing eclipse[9]
	RX J1712-24	Low?	No orbital modulation[10]
FO Aqr	H2215-086	65	Grazing eclipse (of disc)[11]
TV Col	2A 0526-328	70	Grazing eclipse[12]
TX Col	H0542-407	< 25	Low radial velocity amplitude[13]
EX Hya	4U 1228-29	80	Eclipse data[14]

References:

[1] Zhang et al (1995)

[2] Kamata, Tawara & Koyama (1991)

[3] Reinsch (1994)

[4] Mateo, Szkody & Garnsvich (1991)

[5] Penning (1985)

[6] Taylor et al (1997)

[7] Hellier, Cropper & Mason (1991)

[8] Hellier, Ramseyer & Jablonski (1994)

[9] De Martino et al (1995)

[10] Buckley et al (1995)

[11] Hellier, Mason & Cropper (1989)

[12] Hellier, Mason & Mittaz (1991)

[13] Buckley & Tuohy (1989)

[14] Gilliland (1982)

Chapter 2

X-ray observations of intermediate polars

This chapter describes the instruments used, their characteristics, and the results obtained in the study of IPs up to the present. Various analyses of the X-ray signals from some systems are presented, including power spectra, spin pulse profiles and orbital pulse profiles. Evidence for the structures described in the previous chapter is discussed.

2.1 The satellites and instruments

Data from *EXOSAT*, *Ginga*, *ROSAT* and *ASCA* will be presented so a brief summary of the instruments carried by these satellites is given here.

2.1.1 *EXOSAT*

An early mission, from 1983 to 1986, was *EXOSAT*, the European X-ray Observatory Satellite (see White & Peacock, 1988). The orbit was eccentric, with an apogee of $\sim$ 190000 km and perigee of 350 km, and a period of about 90 hours. The instruments were operational above 50 000 km, for 76 hours out of each orbit.

EXOSAT carried several instruments, including a low-energy imaging telescope (LE), a medium energy telescope (ME), and a Gas Scintillation Proportional Counter (GSPC).

The LE had an energy range of $\sim$ 0.05–2 keV, and consisted of a channel multiplier array (CMA) with spatial resolution of $\sim$ 24 arcsec, but no real energy resolution. Its use is similar to the High Resolution Imager of *ROSAT*.

The ME was an array of collimated gas proportional counters, with 128 PHA channels, 40 of which covered the range $\sim$ 2–10 keV, suitable to observe intermediate polars. Each consisted of an argon PC and a xenon PC, the relevant ones to us being the argon PCs, which had an energy resolution of

$$\frac{\Delta E}{E} = 21\left(\frac{E}{6\mathrm{keV}}\right)^{-0.5}\%. \tag{2.1}$$

The telescope had no effective spatial resolution, however. The spatial coverage of the ME was a square field of .75 × .75° FWHM.

The GSPC had a resolution of

$$\Delta E/E = 4.5(E/6\mathrm{keV})^{-0.5}\% \text{ FWHM}.$$

This could be used to provide spectral data, and was effective over the range 1.0 – 20 keV, but its low sensitivity made it unsuitable for viewing low-intensity sources such as intermediate polars.

Taken together, the LE and ME provided data for several intermediate polars during the mission lifetime, and the results have been examined by Norton & Watson (1989), who used spectral data and spin profiles to develope a model using partial covering to explain the results.

2.1.2 *Ginga*

Ginga was launched in February 1987, with instruments including the All Sky Monitor, the Gamma-ray Burst Detector and, relevant to this study, the Large Area proportional Counter (LAC). A detailed description of the *Ginga* satellite and instruments is given by Turner et al (1989).

The LAC comprised 64 equal energy channels, covering the range 0 – 37 keV, the detectors

being argon-xenon-carbon dioxide PCs, which provided a resolution of

$$\frac{\Delta E}{E} = 18\left(\frac{E}{6\text{keV}}\right)^{-0.5}\%. \tag{2.2}$$

Its field of view was elliptical, 1.1° by 2.0° FWHM.

The coverage above 10 keV, together with the good spectral resolution, allowed spectral fitting of the harder X-ray band for several IPs (Ishida, 1991).

2.1.3 *ROSAT*

The Röntgen Satellite (*ROSAT*) was launched in June 1990, with instruments including the X-ray Telescope (XRT) with energy range 0.1 – 2.4 keV, and a coaligned EUV telescope (the Wide Field Camera (0.070 – 0.188 keV)). The XRT had two detectors, the Position Sensitive Proportional Counter (PSPC) and the High Resolution Imager (HRI). The orbit was nearly circular, with an altitude of 580 km and period 96 min. The satellite was used to do an all-sky survey using the PSPC for the first six months, after which the pointing phase began.

The HRI was used to observe several intermediate polars in the early 1990s. This instrument had no energy resolution, so was inappropriate for spectral work, but had good spatial resolution. Its field of view was 38 arcmin (square) and spatial resolution ~2 arcsec. It was found, though, to be useful only for the brighter IPs, and an attempted observation of FO Aqr provided too little signal to noise to be useful.

2.1.4 *ASCA*

The Advanced Satellite for Cosmology and Astrophysics was launched on 20 Feb 1993, in an approximately circular orbit, the period being 96 min. (Tanaka, Inoue and Holt, 1994.) It carried four grazing-incidence X-ray telescopes. The focal-plane detectors were two Solid-state Imaging Spectrometers (SIS) and two Gas Imaging Spectrometers (GIS).

The SIS has a field of view of 20′ × 20′ (square) and resolving power $E/\Delta E \sim 50$ at 6 keV and ~ 20 at 1.5 keV. It is sensitive down to 0.5 keV. The GIS has a circular field of view of diameter 50′, and $E/\Delta E \sim 13$ at 6 keV and ~ 7 at 1.5 keV, but is insensitive below ~ 1 keV. Above ~ 3 keV it has a higher sensitivity than does the SIS, so the instruments have

complementary advantages. Taken together, they can provide imaging and spectroscopic observations in the range 0.5–10 keV, ideal for intermediate polars.

2.2 Raw light curves

The first step in analysing the X-ray signal from a system is usually to have a look at the X-ray light curve, which may have an obvious modulation, often at the spin frequency. Some examples of these are given in figures 2.1 and 2.2, which show the light curves for GK Per and FO Aqr. If a period is already known from optical observations, the X-ray signal would naturally be inspected at that particular frequency, a positive identification identifying the X-ray object with an optical counterpart.

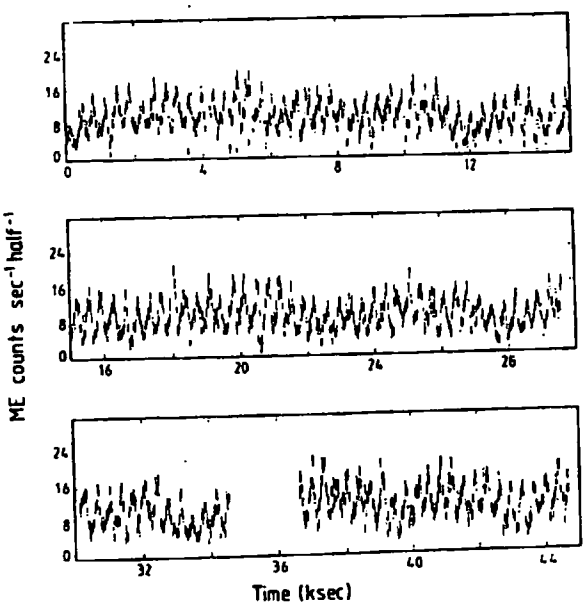

Figure 2.1: Light curve of GK Per (*EXOSAT*).

Figure 2.1 is the light curve from GK Per, and shows the spin modulation clearly. The *Ginga* light curve of FO Aqr, Figure 2.2, shows a feature common to many of these observations: the gaps in the coverage. This is due to the instruments being off-source, which may be due to occultation by the earth (in the case of low-orbit satellites), or because of instrument shutdown whilst passing through radiation belts. The gaps can make it difficult to determine

certain periods in the signal.

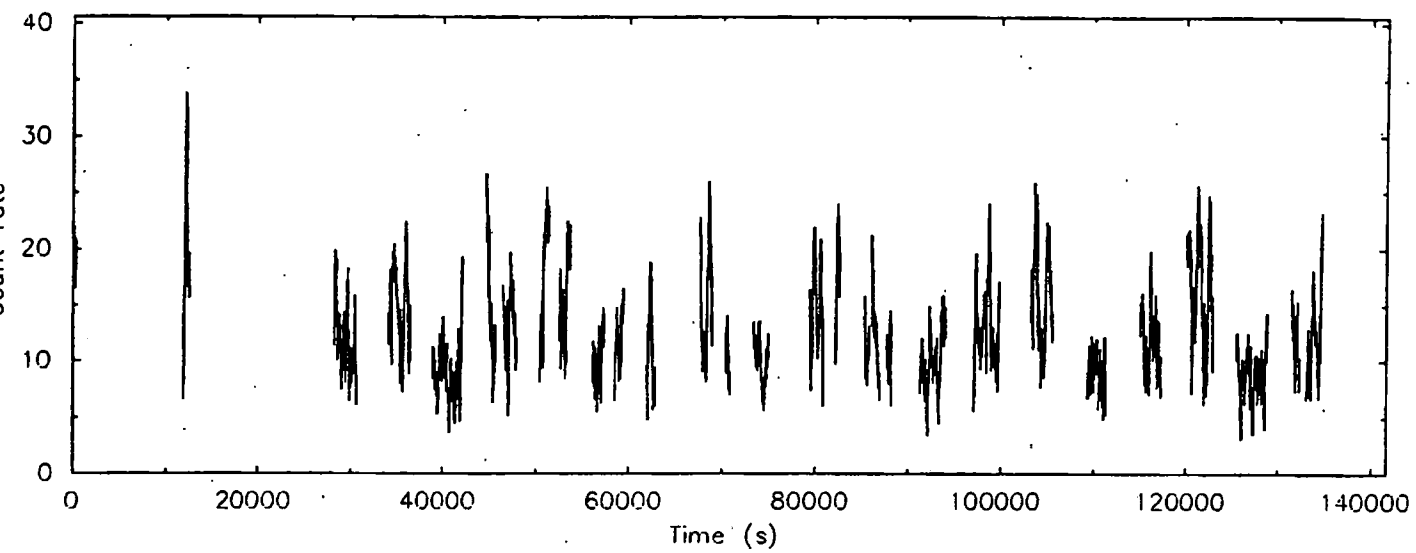

Figure 2.2: Light curve of FO Aqr (*Ginga*).

2.3 Power spectra

Apart from the obvious periods, others may be found by inspecting the power spectrum. The ones shown here (Figures2.3 and 2.4) were derived using the CLEAN algorithm as implemented by H.J. Lehto. This algorithm removes the instrument window function as it builds up the power spectrum.

For discussion of frequencies, we denote the spin frequency by ω and the orbital frequency by Ω. Thus the beat frequency is the negative sideband $\omega - \Omega$.

Figures 2.3 and 2.4 are power spectra from observations of TX Col, the former being the *ASCA* observation of TX Col, which started on 1994 October 3, and the latter from the *ROSAT* HRI observation of TX Col, starting on 1995 October 6.

These were presented in Norton et al (1997); summarising, the 1994 data show a strong

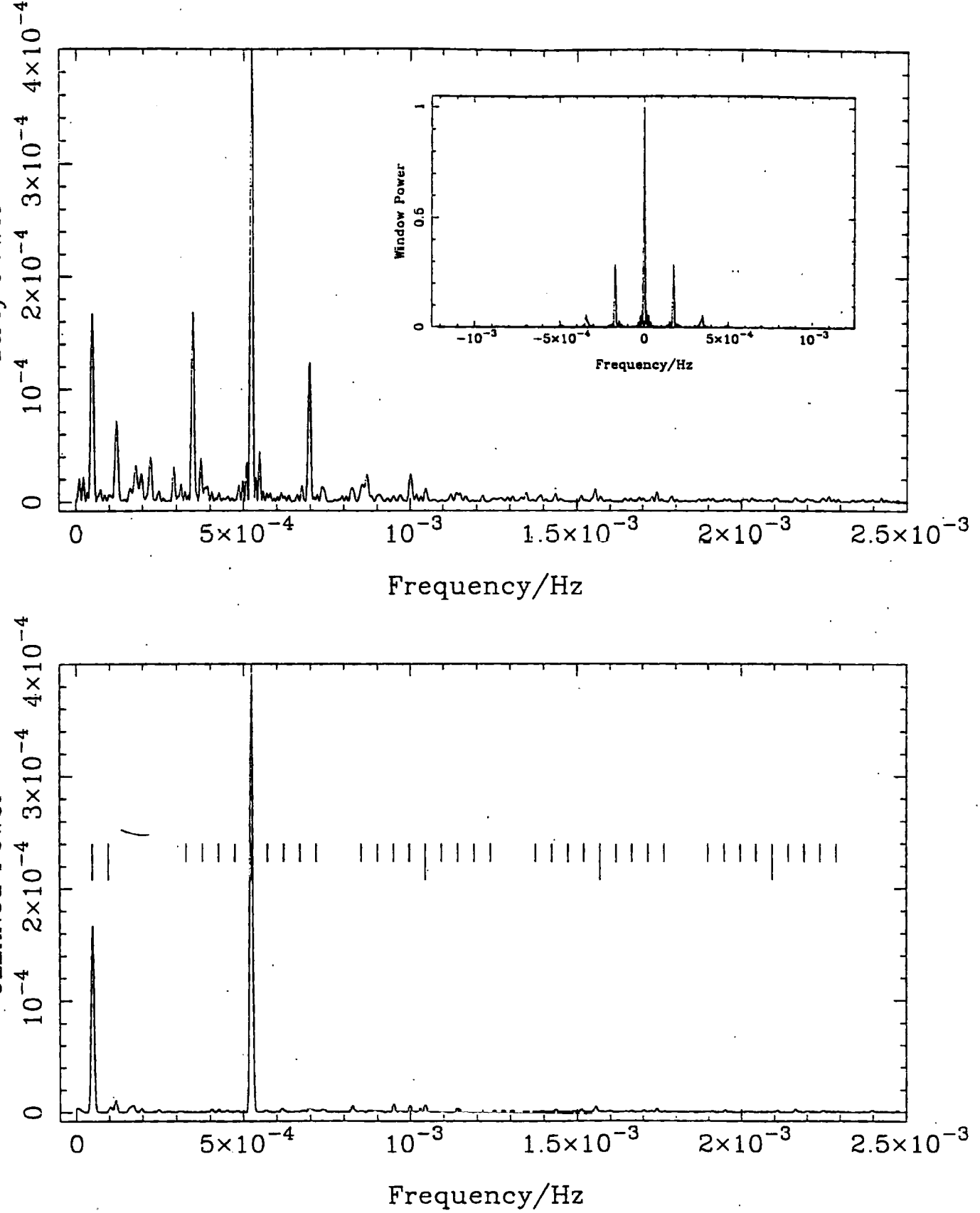

Figure 2.3: Power spectrum of the 0.5 – 7.0 keV ASCA TX Col data. Top is the dirty power with window function inset; bottom is the CLEANed power. (From Norton et al, 1997.)

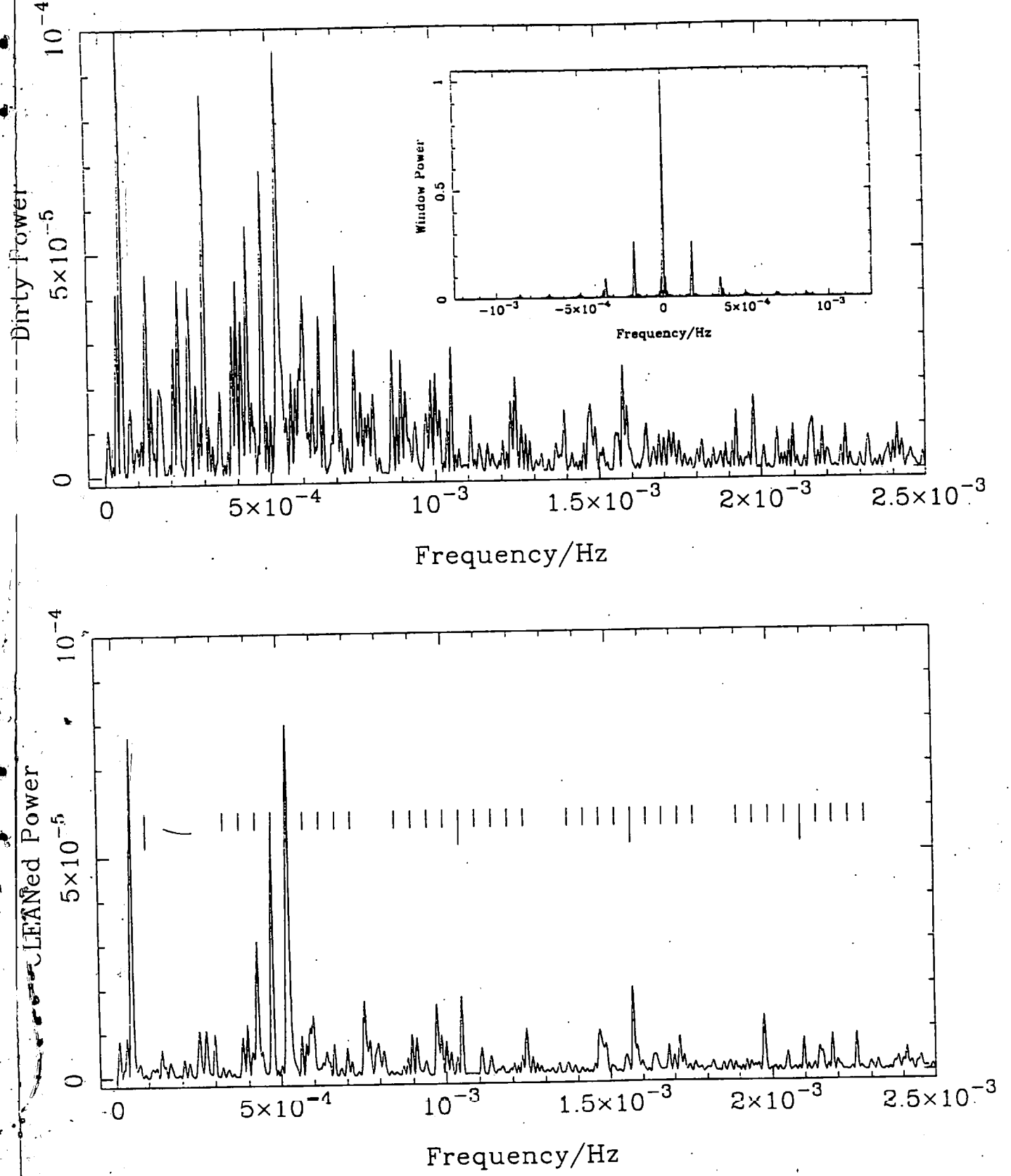

Figure 2.4: Power spectrum of the 0.2 – 2.0 keV HRI TX Col data. Top is the dirty power with window function inset; bottom is the CLEANed power. (From Norton et al, 1997.)

signal at the spin frequency, and also at the orbital frequency, but none at the first two negative sidebands $\omega - \Omega$ and $\omega - 2\Omega$. Since a stream-fed or disc-overflow mode would be expected to show show a signal at the first sideband, we can infer that the system was accreting predominantly via a disc in October 1994. (The large peaks between the spin and orbital frequencies are at the orbital frequency of the *ASCA* satellite, and its first harmonic.)

Figure 2.4 shows the power spectrum from the *ROSAT* HRI observation of TX Col, starting on 1995 October 6. The signal is noisy, but definite peaks are seen at the spin and orbital frequencies, and harmonics of the spin frequency. There are also decreasing peaks at the sidebands $\omega - \Omega$ and $\omega - 2\Omega$. If the presence of a signal at $\omega - \Omega$ is an indicator of a stream-fed component, these two power spectra show a change in the mode of accretion, to a disc-overflow mode, over a timescale of about a year.

A possible model for these, relating the mode to changes in the accretion rate (governed by the secondary) is presented by Norton et al (1997).

Figure 2.5 shows power spectra of FO Aqr at different epochs, and again there is a clearly seen change over epochs. Beardmore et al (1997) also used CLEAN to obtain these. In date order, the first spectrum is from 1988, and exhibits signals at ω, Ω, $\omega - \Omega$, with the harmonics 2Ω, 2ω, 3ω and 4ω. Small signals appear at other sidebands (Beardmore et al consider the top 5 per cent of peaks to be above the noise level). They tabulate the peaks in energy bands, and find the smaller sidebands to be more prominent at lower energies.

The 1993 *ASCA* data also show spin, orbital, beat and other sidebands, although the harmonics are much less prominent. In both these, the spectra suggest a significant stream-fed component to the accretion.

The 1990 *Ginga* data show a much smaller orbital signal, and the beat signal is barely discernible. Thus the situation may be similar to TX Col, each system undergoing changes in accretion mode over timescales of about 1–2 years.

2.4 Spin pulse profiles

The spin pulse profile is obtained by the folding the light curve at the spin period, therefore averaging out effects not resonant with the spin period. The result is usually displayed over

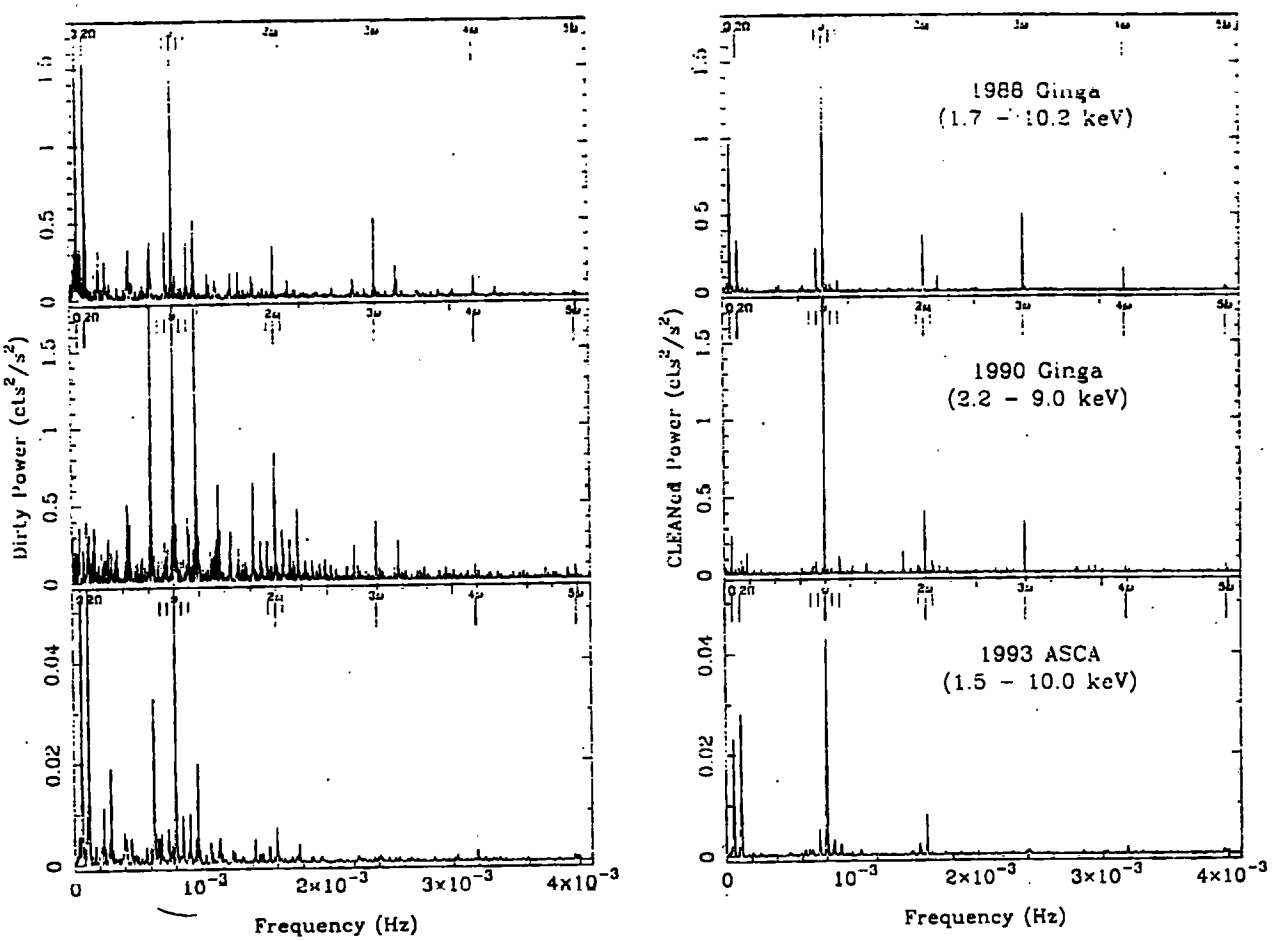

Figure 2.5: Power spectra of FO Aqr at different epochs. (From Beardmore et al, 1997.)

two cycles for clarity (some authors display the profiles over about one and half cycles).

The profiles can be classified by their shapes, one class having roughly sinusoid (and symmetric about phase zero) systems, the others being non-sinusoid, or asymmetric. (Phase zero is defined theoretically in our model as when the upper pole is nearest to the observer. Observationally, it coincides with the X-ray pulse minimum, on the assumption that the Rosen, Mason and Córdova (1988) model applies.) Thus the sinusoid type shapes include TX Col (figure 2.7), EX Hya (figure 2.8), and others. Those with irregular shaped spin profiles include FO Aqr, PQ Gem and BG CMi (figures 2.6, 2.9 and 2.10.)

Any model developed to explain the variety of these shapes is bound to be complex, hence the discussion in Chapter 1 of the interactions of occultation and absorption. Also, while systems with symmetric spin profiles can be modelled fairly simply by assuming diametrically opposite poles, the others require additional assumptions. It will be argued later that a dipole placed non-diametrically in the white dwarf can explain these type of spin profiles. (Specifically, the lower pole has an azimuthal lag relative to the upper different to 180°, contrary to the case of a symmetrically-placed dipole.)

FO Aqr is also intriguing in that its spin profile changes over epochs as well, and sometimes *is* symmetric. (The previous section has already shown evidence for important changes in accretion mode.) Any model of accretion ought to be able to explain this feature.

The spin profiles may also be used to calculate modulation depths, which are seen to differ at different energies. One work which included a study of these is Norton & Watson (1989), which used *EXOSAT* data of eight intermediate polars for their modelling. Their conclusion was that there is a decrease in the *modulation depth* as the energy increases.

This property, the energy-dependence of the *modulation depth*, suggests that absorption decreases at higher photon energies, and is consistent with a significant photoelectric absorption component of the absorption. (Electron scattering is expected to be present, but is energy independent.) Labelling the maximum X-ray luminosity of the spin profile by X_{max}, and the minimum by X_{min}, the modulation depth is defined in this document as $MD = (X_{max} - X_{min})/(X_{max} + X_{min})$. The maximum and minimum values are obtained where possible by finding the best-fit sinusoid to the profile curve. If this fitted sinusoid has the form $A\sin(\omega t - \phi) + B$, where ϕ is an arbitrary phase, then the amplitude $A = 0.5(X_{max} - X_{min})$ and the average $B = 0.5(X_{max} + X_{min})$, hence $MD = A/B$ is an

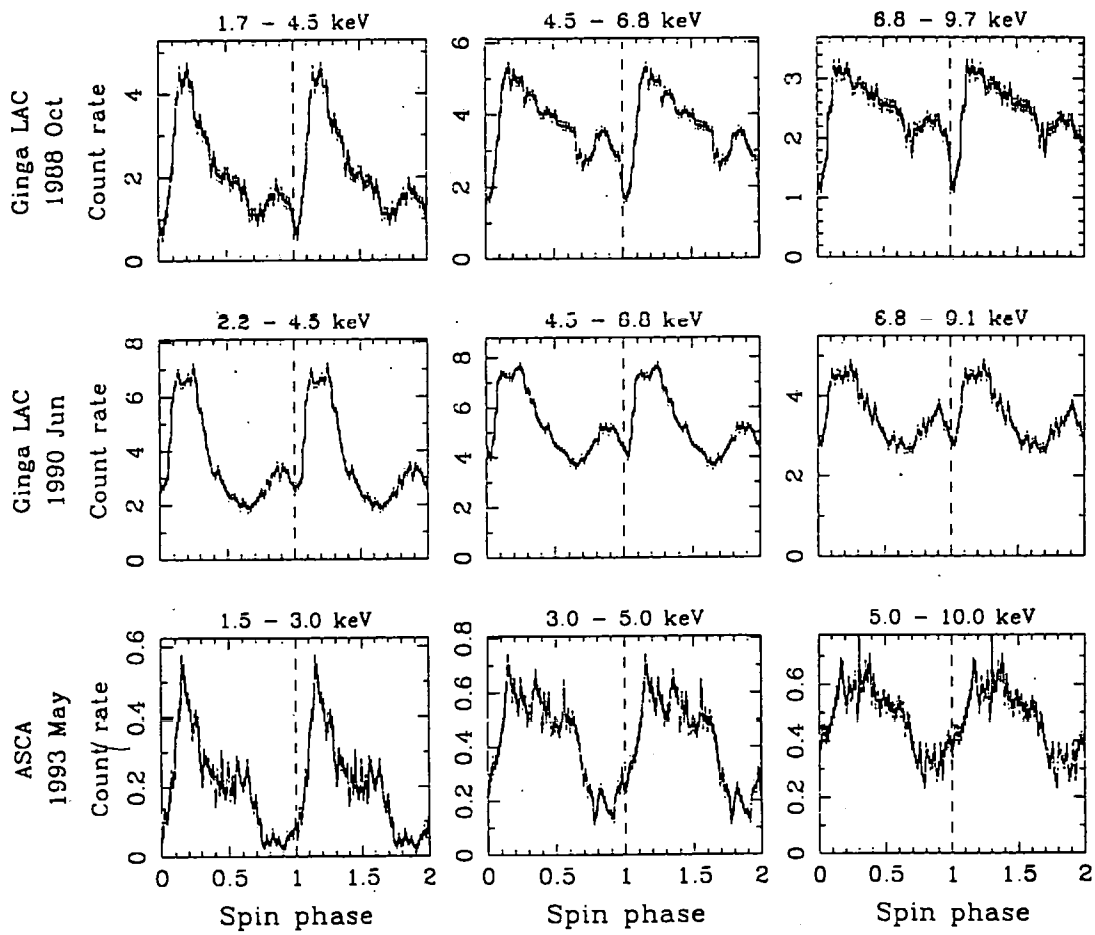

Figure 2.6: Spin pulse profile for FO Aqr, considered at different epochs. (From Beardmore et al, 1997.)

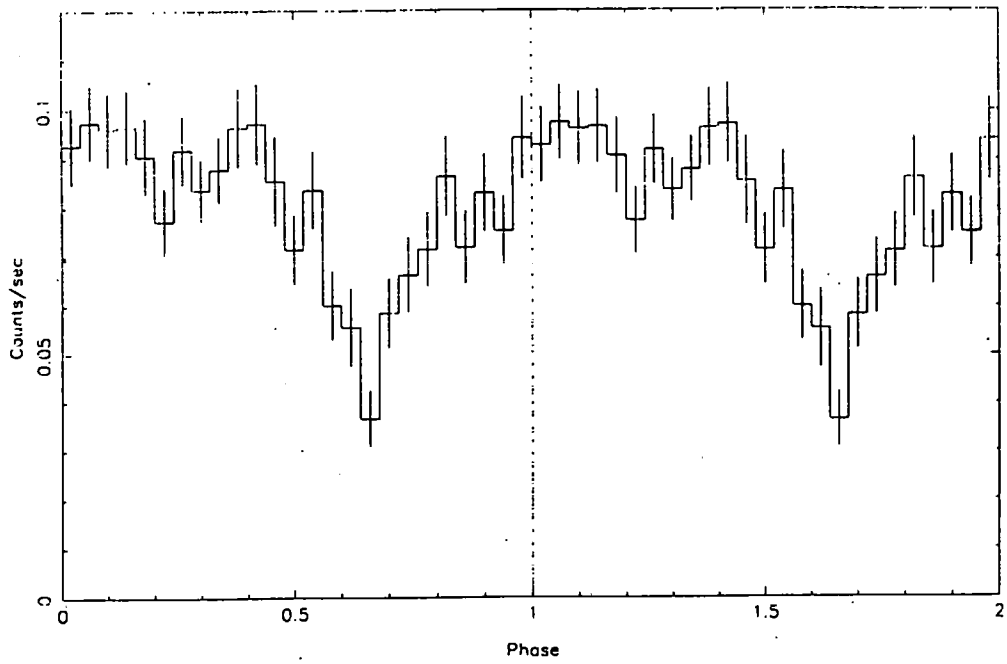

Figure 2.7: Spin pulse profile for TX Col. (ROSAT *HRI*)

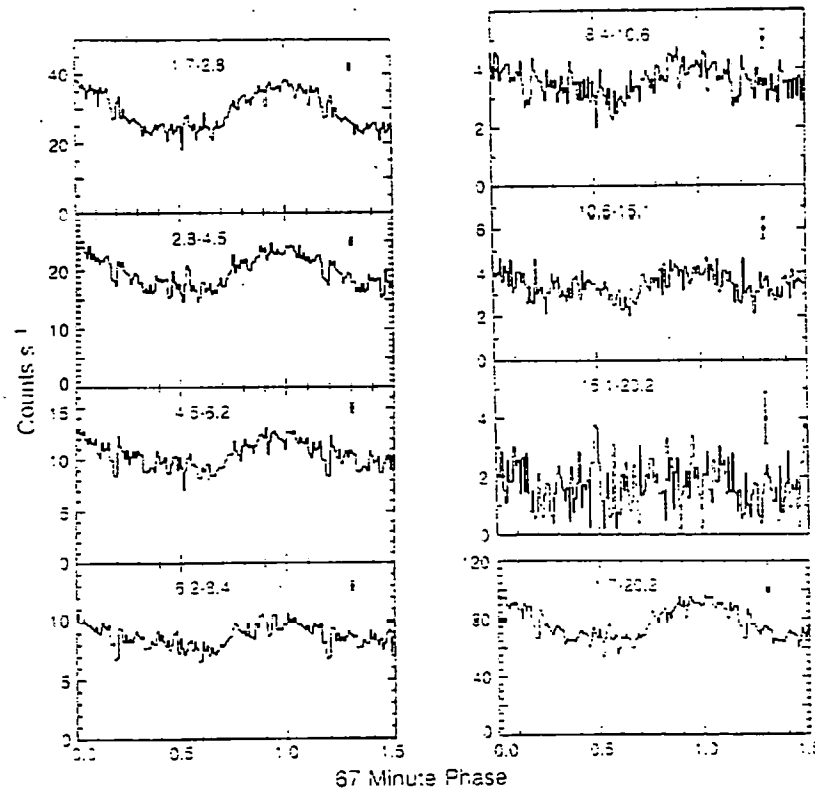

Figure 2.8: Spin pulse profile for EX Hya. (*Ginga*)

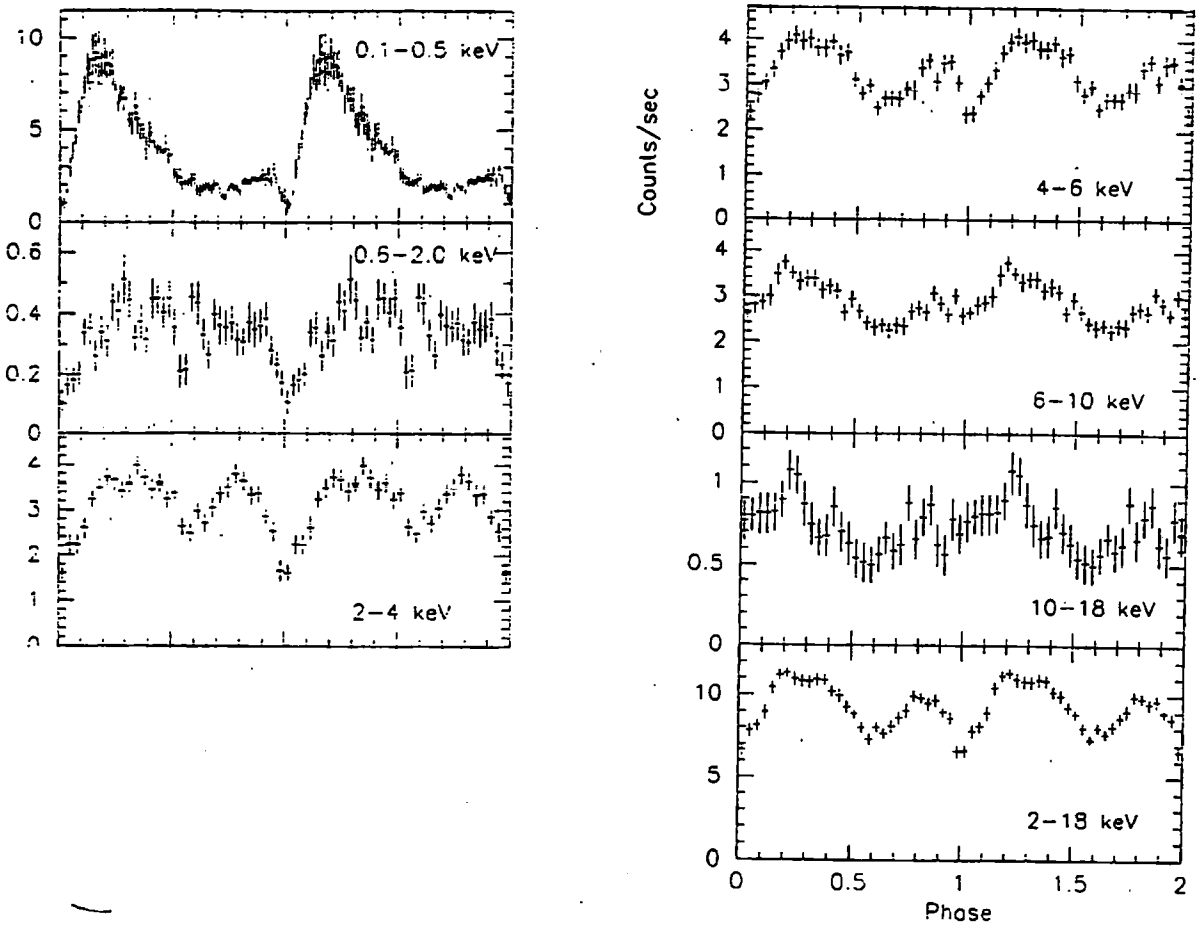

Figure 2.9: Spin pulse profile for PQ Gem (X-ray name RE0751+14) (ROSAT PSPC & *Ginga*, from Duck et al, 1994).

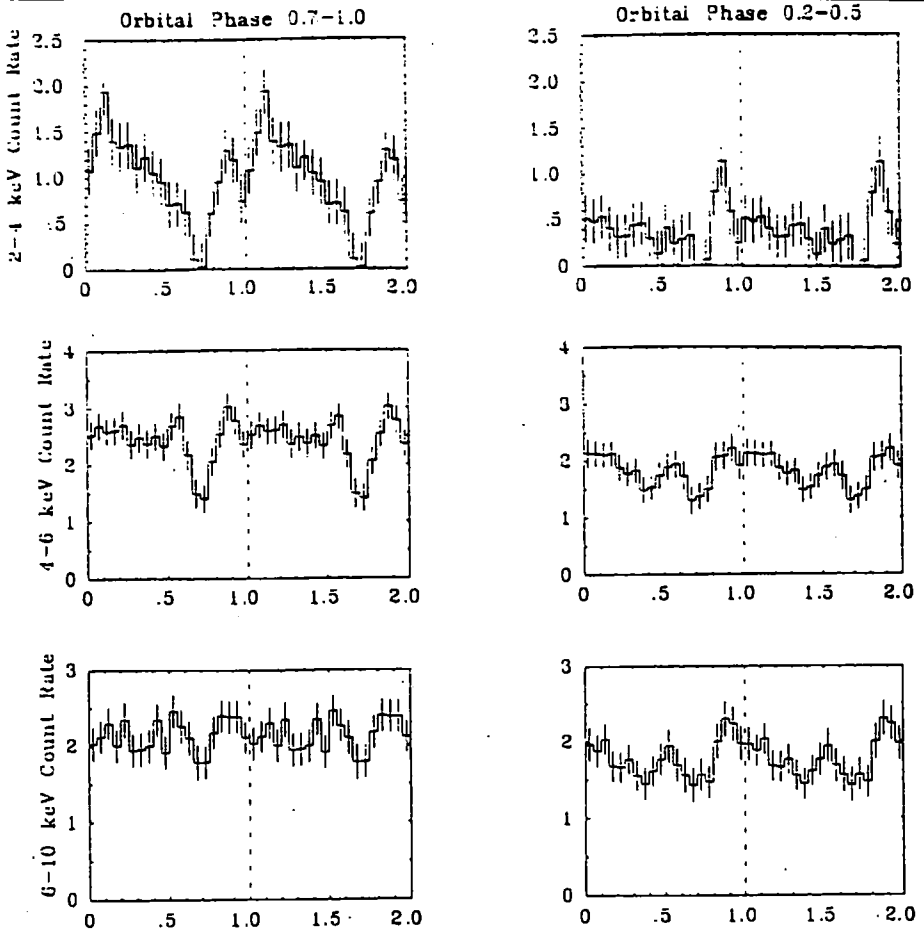

Figure 2.10: Spin pulse profile for BG Cmi (*Ginga*, from Norton et al, 1992).

alternative expression.

In the case of FO Aqr, whilst its spin profile is asymmetric at some epochs, it can be considered to be an (approximate) sinusoid with a notch, and the fitting curve is applied to the sinusoid.

Now let the total optical depth at pulse maximum be τ_{min}, and at pulse minimum be τ_{max}, so τ_{max} corresponds to minimum observed luminosity, and vice versa. These include the interstellar column and the absorber intrinsic to the white dwarf. Also let the interstellar column have optical depth τ_I. To allow for the case of a partial absorber, let the uncovered fraction be F_1 and the covered fraction be F_2, so $F_1 + F_2 = 1$.

Using this information, and letting the minimum and maximum observed luminosities be X_{min} and X_{max}, we can deduce information about the column densities of the absorber at different spin phases, as follows:

$$X_{max} = X_0(F_1 \exp(-\tau_I) + F_2 \exp(-\tau_{min})), \quad (2.3)$$

$$X_{min} = X_0(F_1 \exp(-\tau_I) + F_2 \exp(-\tau_{max})), \quad (2.4)$$

where X_0 is the intrinsic brightness of the source, whence

$$MD = \frac{X_{max} - X_{min}}{X_{max} + X_{min}} \tag{2.5}$$

$$= \frac{F_2(\exp(-\tau_{min}) - \exp(-\tau_{max}))}{2F_1\exp(-\tau_I) + F_2(\exp(-\tau_{min}) + \exp(-\tau_{max}))}$$

$$= \frac{(1 - \exp(-\Delta\tau))}{1 + \exp(-\Delta\tau) + 2\frac{F_1}{F_2}\exp(\tau_{min} - \tau_I)} \tag{2.6}$$

where $\Delta\tau = \tau_{max} - \tau_{min}$.

The local absorber will be a plasma, and its absorption will have a component of electron scattering, and one of photoelectric absorption. In the energy range 0.53 – 10.0 keV, the photoelectric component depends on photon energy by

$$\tau_{pe} = 10^{-21.4}E^{-2.7}N_H$$

$$= 4.0 \times 10^{-22}E^{-2.7}N_H, \tag{2.7}$$

whereas the scattering component is energy independent, and can be expressed as

$$\tau_{es} = 6.65 \times 10^{-25}N_H \tag{2.8}$$

using the Thomson cross-section.

In the simplified case of a total absorber, with $F_1 = 0$, $F_2 = 1$,

$$MD = \frac{1 - \exp(-\Delta\tau)}{1 + \exp(-\Delta\tau)}. \tag{2.9}$$

$$\text{Also } \tau = \tau_{es} + \tau_{pe}$$

$$= 10^{-25}(6.65 + 4000E^{-2.7})N_H,$$

$$\text{so } \Delta\tau = 6.65 \times 10^{-25}(1 + 600E^{-2.7})\Delta N_H. \tag{2.10}$$

Differentiating MD with respect to $\Delta\tau$ gives

$$\frac{dMD}{d\Delta\tau} = \frac{2\exp(-\Delta\tau)}{(1 + \exp(-\Delta\tau))^2}$$

hence MD increases as $\Delta\tau$ increases. However the latter decreases as E increases, so modulation depth decreases with increasing energy.

The general expression can also be differentiated, with respect to E. To reduce the complexity, assume $\tau_I << \tau_{min}$, being effectively zero, and let N_{min} be the value of N_H at the absorption minimum of the spin cycle, and N_{max} be its value at the maximum absorption.

Then, using the exponent of E to be -3 rather than -2.7 for simplicity,

$$MD \simeq \frac{(1-\exp(-\Delta\tau))}{1+\exp(-\Delta\tau)+2\frac{F_1}{F_2}} \tag{2.11}$$

$$\text{and} \quad \frac{\mathrm{d}MD}{\mathrm{d}E} \simeq \frac{2.4\times10^{-21}E^{-4}}{V^2}[-\Delta N\exp(-\tau_{max}-\tau_{min})+F_1/F_2]. \tag{2.12}$$

In the above, $V = \exp(-\tau_{min})+\exp(-\tau_{max})+2F_1/F_2$. The expression is transcendental, but numerical investigation shows that it has a zero at the order of 1 keV for plausible values of the N_H, when $0 < F_1 < 1$. The graph of the function for MD confirms this, showing a maximum at this point. For example, putting $F_1 = 0.6$, $N_{max} = 4\times10^{21}$, and $N_{min} = 10^{21}$, $\frac{\mathrm{d}MD}{\mathrm{d}E} = 0$ at $E \simeq 0.9$ keV; with $N_{max} = 4\times10^{22}$, and $N_{min} = 10^{22}$, $\frac{\mathrm{d}MD}{\mathrm{d}E} = 0$ at $E = 1.9$ keV. Norton & Watson (1989) also derive this prediction from partial covering assumptions. The modulation depth maximum is observed in the testing (Chapter 5) when partial covering is simulated.

With sufficient quality coverage over a range of energies, it can be determined whether a partial absorber is necessary to fit the data.

Considering the effect of energy, it may be noted that below ~3–4 keV, τ_{pe} dominates τ_{es} by a factor > 10, while the reverse is true for energies above ~10 keV. Thus above 10 keV, absorption can be considered to be dependent on N_H alone.

2.5 Orbital profiles

In some systems the light curve shows directly that an orbital modulation exists, for example the *Ginga* observation of FO Aqr in figure 2.2. When we look at the orbital profiles, it appears that these modulations come in two types: a roughly sinusoidal variation over the whole orbital cycle; and dips which last over a brief fraction of the cycle, starting at approximately the same phase, and lasting about 0.1–0.2 periods. The explanation for these two effects is likely to be different. The former, for example, may be an absorber fixed in the orbital plane and extending the whole way round the system, varying with azimuthal angle. The latter, on the other hand, while also being orbitally fixed, may be sharply localised. One possible model of this is material thrown up out of the orbital plane where the stream (from the L1 point) hits the disc. This requires the inclination angle to be within certain limits, else the line of sight would not pass through such an absorber. If the inclination angle is near the critical value, there may also be an orbitally extended absorber which only

affects the observed flux in a small range of phases, as the line of sight grazes the material.

The next chapter has a more detailed study of two intermediate polars, AO Psc and V1223 Sgr, in which some of these effects, along with the spin profiles, are shown and discussed.

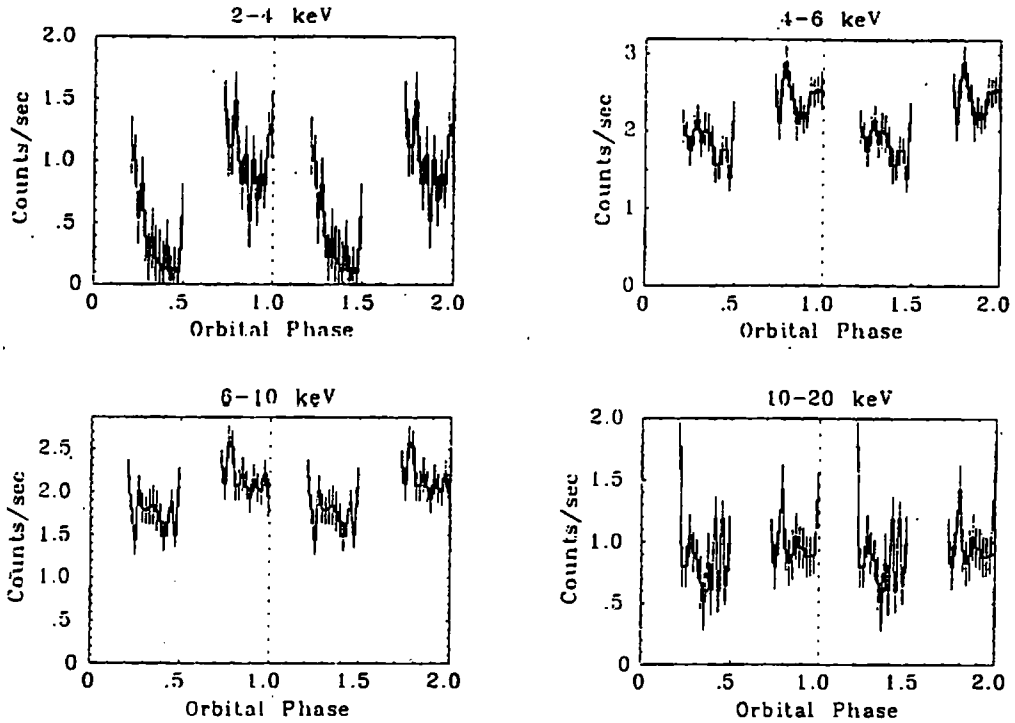

Figure 2.11: Orbital pulse profile for BG Cmi (Norton et al, 1992b).

2.6 Spectroscopy

The theory of accretion on to white dwarfs predicts that the main cause of emission will be optically-thin thermal bremsstrahlung, of characteristic temperatures $kT \sim 30$ keV (Frank, King & Raine, 1992). Various researchers have attempted to fit this model to spectral data, see for instance Ishida (1991). This study found broad similarities among the various sources in the X-ray spectra above $\gtrsim 6$ keV, but differences in the band below this. Also, most showed a strong iron K-emission line at 6-7 keV. Ishida tried several models to fit data from *Ginga*, including bremsstrahlung and power-law with photoelectric absorption. However, fits with a single emission component were poor in all but two of the cases, the bremsstrahlung being better than the power-law. Addition of a model iron-line (a gaussian

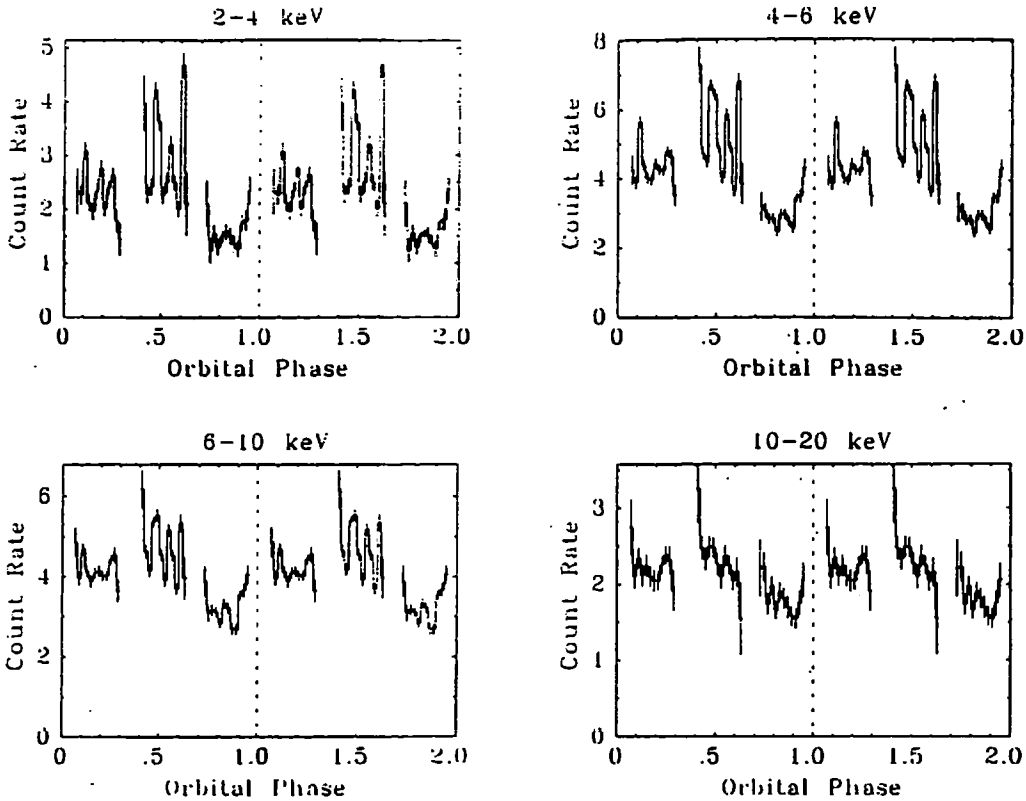

Figure 2.12: Orbital pulse profile for FO Aqr. (Norton et al, 1992a).

centred on ~ 6.8 keV) was better, but still gave fits below the 90 per cent confidence level.

The residuals in Ishida's data were greater at low energies, and the bremsstrahlung model gave a more acceptable fit for energies above ~ 10 keV. This is consistent with the optically-thin thermal bremsstrahlung model, at least for the hard X-ray band. Temperatures obtained ranged from ~10–40 keV, broadly as expected.

The variation at softer energies may be due to using a single component in the photoelectric absorption. This would be expected to affect lower energies more due to the strong correlation ($\propto\sim E^{-3}$) of absorption with energy.

2.7 Discussion

The rôle of observations is twofold: to identify systems which are members of the class of intermediate polars, and to provide data enabling different models of the processes to be postulated or refined, for example ruling out simple models based on single-component

emission as above.

The identification of intermediate polars is not always a simple task; the detection of appropriate periods in the optical or X-ray band is a good indicator. A system showing a period of several hours together with periods of several minutes (especially if two such shorter periods were linked as being sidebands) would be a good candidate for a member of the class. The short periods would be difficult to explain by a non-compact object.

Note that the period(s) need not be determined photometrically, but could be determined spectroscopically.

However, these are not always detected, and some systems have been classified on other grounds, one of which is a hard X-ray spectrum. It should be mentioned here that the various signatures of intermediate polars are usually not all present in any single system (see Patterson, 1994).

Chapter 3

X-ray studies of AO Psc and V1223 Sgr

In this chapter the results of observations of the IPs AO Piscium and V1223 Sagitarii using *ROSAT* and *Ginga* are presented. It is largely based on Taylor et al (1997) with some extra background analysis.

3.1 Introduction

We recall (from Chapter 1) that models of accretion in intermediate polars may be split into three broad classes: (i) The accretion may be via an accretion disc, the infalling material hitting the outer edge of the disc at a "hotspot", with some matter being thrown out of the orbital plane. After passing through to the inner edge of the disc, the material threads onto the magnetic field lines, and the result is an arc-shaped accretion curtain above the shock and a corresponding footprint on the white dwarf's surface (Rosen, Mason and Córdova 1988). (ii) If the field is too strong to allow a disc to form, the material accretes directly as a stream which falls from the inner Lagrangian point (see e.g. Hameury, King & Lasota 1986). At several radii above the white dwarf, the material threads onto the magnetic field lines and is channelled onto a region of the surface in the vicinity of one of the poles. (iii) A proportion accretes via a disc, whilst the rest accretes directly, skimming over the disc

Table 3.1: Observation log

Target	Instrument	Start time(UT)	Duration /hr	Exposure /ks	Mean flux(2-10 keV) /erg cm^{-2} s^{-1}
AO Psc	*Ginga* LAC	1990 Jly 10 18:00:00	24.0	29.7	5.6×10^{-11}
V1223 Sgr	*Ginga* LAC	1991 Oct 02 02:18:54	22.8	17.0	1.95×10^{-10}
V1223 Sgr	*ROSAT* HRI	1994 Oct 08 20:53:22	115.9	49.1	
AO Psc	*ROSAT* HRI	1994 Dec 17 09:48:32	84.8	51.8	

surface. This is known as a disc-overflow mechanism, described in Lubow (1989).

As previous chapters have mentioned, current problems in modelling these systems include whether a single column density can adequately fit the observations; what proportion of accretion is direct or via a disc; and, if orbital modulation is a common feature, what is its precise cause. Some of these are examined in the light of the observations discussed here.

3.2 The observations

The observations presented here are of two of the longest established intermediate polars, AO Psc and V1223 Sgr. AO Psc was first detected as an X-ray source (H2252–035) by *HEAO-1*, and its optical counterpart was identified as a 13th magnitude emission-line object. The X-rays were modulated at a period of 805s, recognised as the spin period of the compact object whilst the optical flux was modulated at two periods, 3.59 hours (the binary orbital period) and 858s (the beat period). See White & Marshall (1981), Patterson & Price (1981) and references therein.

V1223 Sgr, a 13th magnitude irregular variable star, was identified with the *Uhuru* source 4U1849–31 by Steiner et al (1981). The optical pulse period of 794s (the beat period of the system), and the 3.37 hour orbital period were firmly established by Warner & Cropper (1984). The 746s spin period of the white dwarf, predicted by Steiner et al (1981), was later detected using *EXOSAT* observations by Osborne et al (1985a, 1985b).

Both objects were more recently observed by the *ROSAT* High Resolution Imager and the *Ginga* Large Area Counter. Table 3.1 summarises the information about each observation.

For technical information regarding these instruments see Zombeck et al (1995) and Turner et al (1989) respectively.

The *ROSAT* HRI data were reduced using the Starlink *Asterix* package (Allen & Vallance 1992). For AO Psc source counts were averaged over a 1.8′ radius centred on the object, and the background count rate was determined from a 3.0′ radius annulus surrounding the source, which was then subtracted by proportion from the source area. The equivalent figures for V1223 Sgr were 3.0′ and 9.0′. The HRI has an energy range of 0.2 – 2.4 keV, with the largest proportion of sensitivity being between 0.5 and 2.0 keV.

The *Ginga* data were obtained from the archive at Leicester University and data analysis and background subtraction were done using standard software. As *Ginga* has no provision for a simultaneous background measurement, nearby off-source regions were observed so that suitable modelling of the X-ray background could be made. For AO Psc we used the local method described in Hayashida et al (1989) which involves three radioactive decay terms. For V1223 Sgr a variation on this was used, involving only one decay term (with e-folding time of 12.5 hours) due to passage through the South Atlantic Anomaly, as the background variability was found to be reduced towards the end of the *Ginga* mission (Butcher, private communication to A. P. Beardmore). After background subtraction, *Ginga* LAC lightcurves were created in four energy bands $1.7 - 4.1$, $4.1 - 6.4$, $6.4 - 9.8$ and $9.8 - 18.6$ keV.

3.3 Results

3.3.1 AO Piscium

The lightcurves for the two observations are shown in Figures 3.1 and 3.2. Orbital phases were calculated using the optical ephemeris from Kaluzny & Semeniuk (1988), whose phase zero corresponds to optical maximum. When extrapolated to the epochs of these observations, there is an uncertainty of ~ 0.11 cycles for the *ROSAT* data and ~ 0.07 cycles for the *Ginga* data.

Figure 3.1, the *ROSAT* lightcurve for AO Psc, shows a clear spin modulation, and also a pronounced dip in each orbital cycle at around orbital phase 0.5–0.8. The *Ginga* lightcurve (figure 3.2) also shows the spin modulation, but orbital dips are less apparent. Where

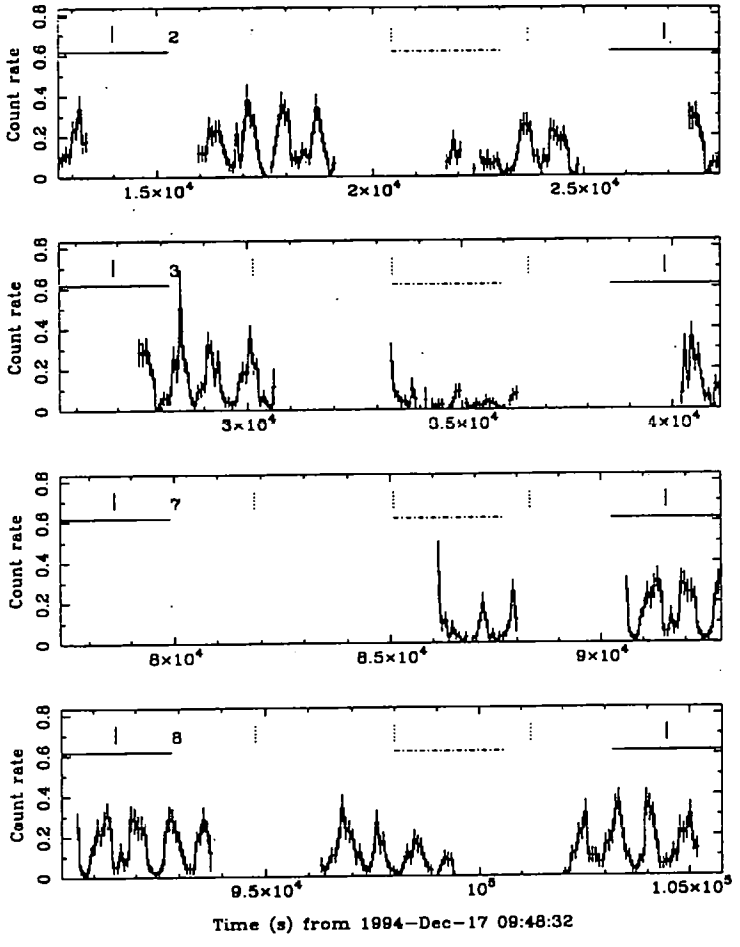

Figure 3.1: *ROSAT* HRI lightcurve for AO Psc (0.2 – 2.4 keV). Solid vertical tick-marks indicate orbital phase zero; dotted tick-marks indicate quarter phases. The phase range around orbital maximum used for the spin folded data is indicated by solid horizontal lines; the range around orbital minimum is indicated by dashed and dotted horizontal lines. The panels are aligned by orbital phase for direct comparison between orbital cycles; the numbers in the panels indicate the orbital cycle from the beginning of the dataset. The cycles in which the target was on-source during the orbital minimum have been selected.

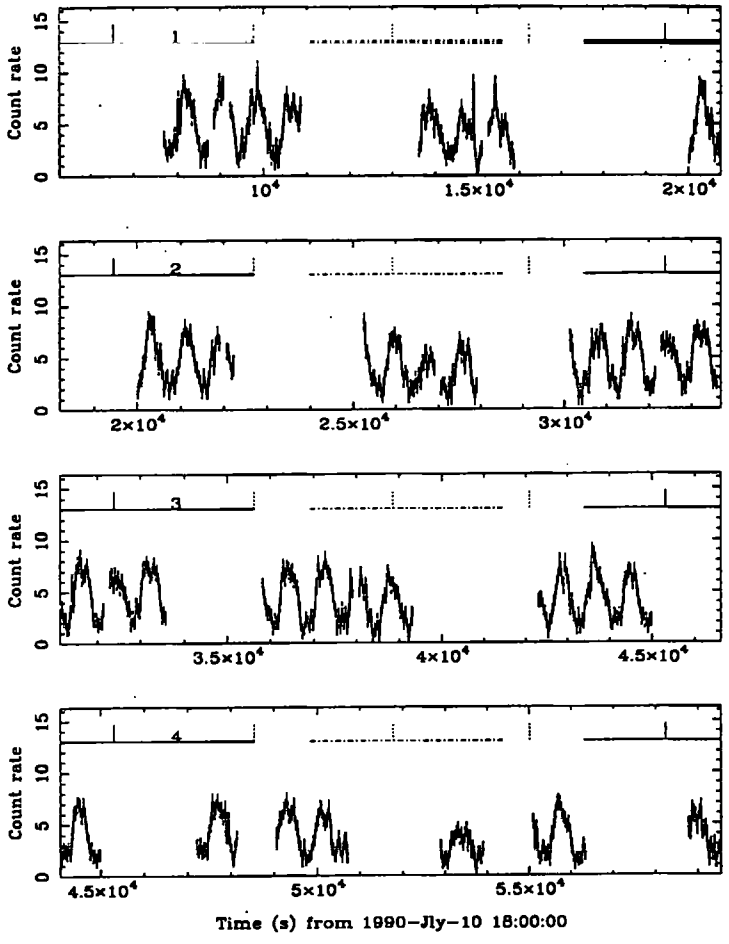

Figure 3.2: *Ginga* LAC lightcurve for AO Psc in the energy range 1.7 – 4.1 keV. Horizontal lines and vertical tick-marks are as for figure 3.1.

present, they are clearest in the lowest energy band, shown here, at around the same phase as in the *ROSAT* data.

Figure 3.3 shows the power spectrum from the *Ginga* observation of AO Psc. The tickmarks in the CLEANed spectrum indicate periods and sidebands, and show a strong signal at the spin frequency (1/805.2 s). There is no discernible signal at the beat frequency (the tickmark just prior to the largest peak), but a signal shows at the orbital frequency (the first tickmark), and at multiples of the spin frequency. The absence of a beat signal suggests that the accretion is predominantly via a disc. There may be a weak signal at the $\omega - 2\Omega$ sideband, just above the noise level. (Although this spectrum covers the 2–10 keV range, others were obtained for the ranges ~2–4, ~4–6, ~6–10 and ~10–20 keV, but only the lowest range showed the sideband feature.)

Figure 3.4 shows the power spectrum from the *ROSAT* observation of AO Psc. Again there are strong signals at the spin and orbital frequencies but this time there is a small signal at $\omega - \Omega$, and a larger one at $\omega + \Omega$. The difference could be simply the trend noted in the *Ginga* data, with the beat effect more prominent at lower energies, but it should be noted that the *ROSAT* data dates from four years after the *Ginga* data, giving the possibility of a slightly larger stream-fed component (though still predominantly disc-fed).

The weak sideband signals suggest that there is some amplitude modulation of the spin pulse, say by an absorber fixed in the orbital frame (Norton, Beardmore & Taylor 1996). However, theory suggests that if this *is* the cause, the sidebands should have the same amplitude, hence either an extra effect is present, or the inequality suggests that there are noise effects in the spectrum.

Figure 3.5 shows these lightcurves folded at the orbital period, using the ephemeris above. Bearing in mind the relative phase uncertainty, the X-ray orbital maximum is approximately in phase with the optical maximum. There is a well-defined modulation in the *ROSAT* data, but this is less clear in the *Ginga* data, although still present. At even higher energies, there is little evidence for an orbital modulation. This is consistent with the findings of Hellier, Cropper & Mason (1991) from the earlier *EXOSAT* observations (1983 and 1985), each of which spanned fewer orbital cycles than these observations.

We have extracted subsets of the signal from ranges of orbital maximum and orbital minimum for separate analysis, folding them at the spin period, to allow comparison of modula-

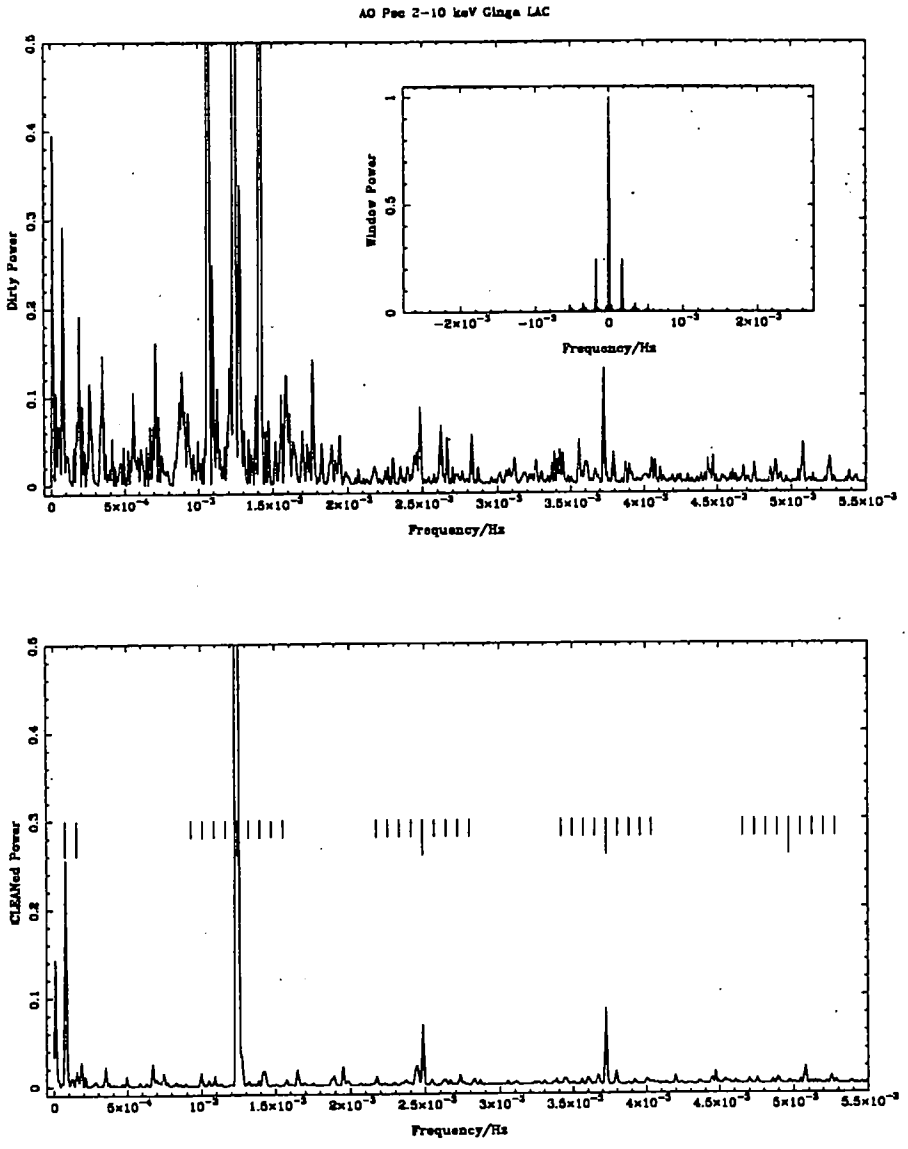

Figure 3.3: *Ginga* Power spectrum for AO Psc in the energy range 2.0 – 10.0 keV. Top panel is the dirty spectrum, the bottom panel is the CLEANed spectrum.

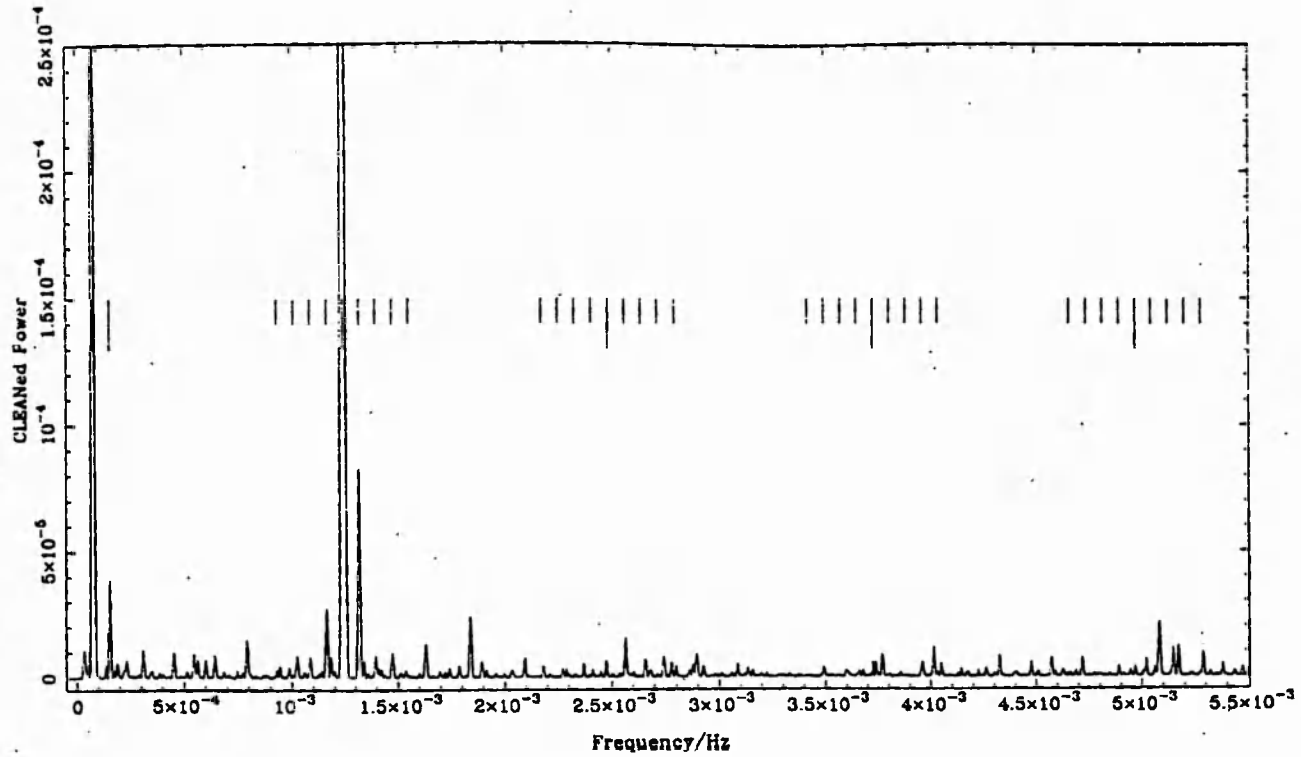

Figure 3.4: *ROSAT* Power spectrum for AO Psc in the energy range 0.2 – 2.0 keV.

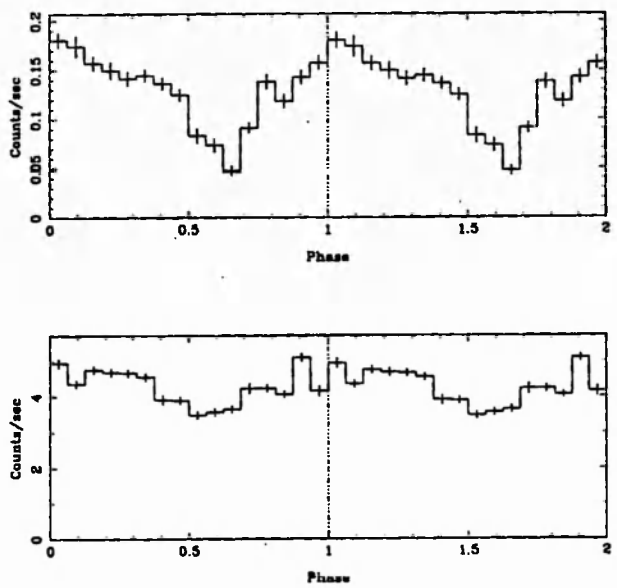

Figure 3.5: AO Psc data folded at the orbital period. The upper panel shows the *ROSAT* data and the lower panel shows the *Ginga* data in the energy range 1.7 – 4.1 keV. The binsize is approximately one spin cycle in length.

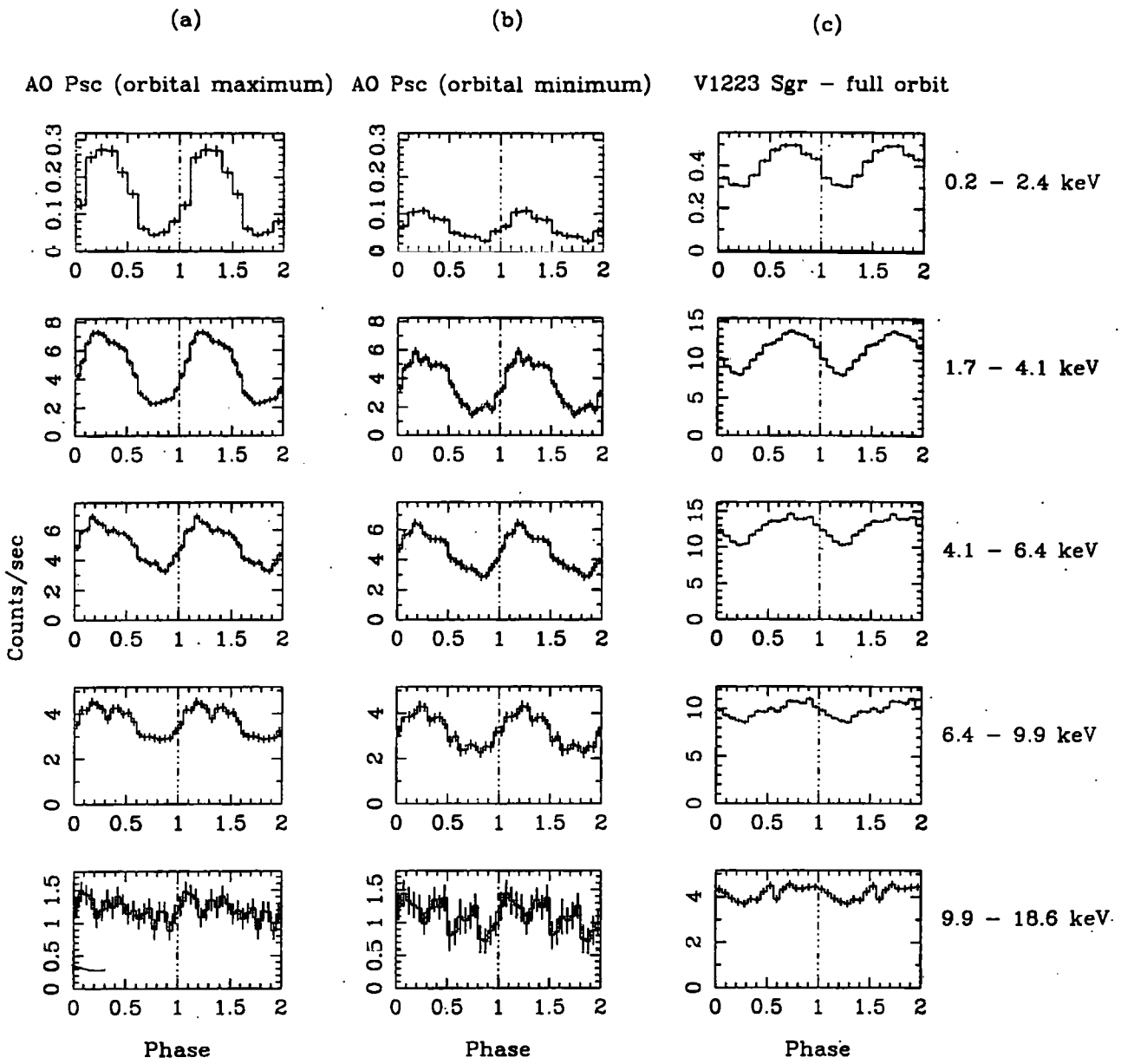

Figure 3.6: AO Psc and V1223 Sgr data folded at the spin period. The first row is from *ROSAT*, the rest are four successive energy bands from *Ginga*. Columns (a) and (b) are for AO Psc, from orbital maximum and orbital minimum respectively; column (c) for V1223 Sgr, from the whole orbital cycle. Columns (a) and (b) use the same vertical scale to enable comparison, column (c) is independent.

tion depths at orbital maximum and minimum (figure 3.6). The published spin ephemeris of Kaluzny & Semeniuk was found to have uncertainties greater than half a spin period when extrapolated to the epochs of these observations. Spin phase zero in figure 3.6 is therefore arbitrary, although the two sets of data (at different epochs) have been aligned by sinusoidal fitting.

3.3.2 V1223 Sagittarii

Figures 3.7 and 3.8 show the lightcurves for V1223 Sgr obtained with *ROSAT* and *Ginga* respectively. Figure 3.7 displays a strong modulation at the spin period. Using the orbital ephemeris of Jablonski & Steiner (1987), phases are plotted on the figures (accurate to ~ 0.1 cycles in the case of the *ROSAT* data when extrapolated to this epoch). Phase zero of this ephemeris corresponds to optical maximum. Intermittent dips are clearly seen in the *ROSAT* data, occurring at orbital phase $0.75 - 0.85$ in cycle 1, $0.73 - 0.81$ in cycle 3, and $0.64 - 0.80$ in cycle 29. Elsewhere, these dips are less prominent, but may be present in, for example, cycles 2 & 28. When folded at the orbital period, the *ROSAT* lightcurve shows no consistent pattern of modulation, which is to be expected given the cycle-to-cycle variation in dips apparent in figure 3.7.

The *Ginga* lightcurve is shown in figure 3.8; it has quite sparse coverage, showing a clear modulation at the white dwarf spin period, but the sparseness makes it difficult to ascertain whether any modulation or dips are evident at the orbital period.

The *ROSAT* power spectrum (figure 3.9) shows a small signal at the orbital frequency, but little evidence of sidebands is present. The dominant signal is the spin frequency. The *Ginga* power spectrum (figure 3.10) shows no evidence for a signal at the orbital frequency, although given the sparse coverage this is not surprising. As with AO Psc, there is little evidence for a beat signal in the power spectra of each data set.

The lightcurves folded at the spin period of the white dwarf are shown in figure 3.6 (column (c)). As the spin ephemeris of Jablonski & Steiner cannot be extrapolated successfully to the epochs of these V1223 Sgr observations, the phasing in column (c) of figure 3.6 is arbitrary. Since clear orbital maxima and minima are not present in these datasets, we show only one set of spin folds.

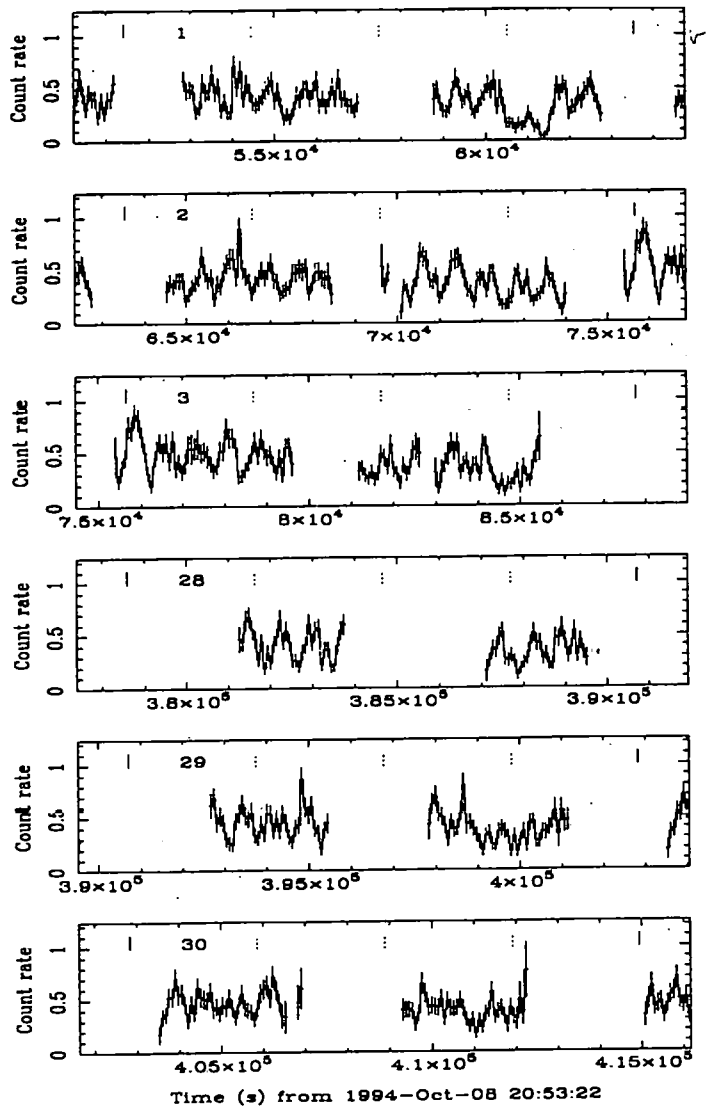

Figure 3.7: The *ROSAT* HRI lightcurve for V1223 Sgr in the energy range 0.2 – 2.4 keV. Vertical tick-marks are as for figure 3.1 and the numbers indicate orbital cycle from the start of the observation. The telescope was off source during orbital cycles 4 to 27.

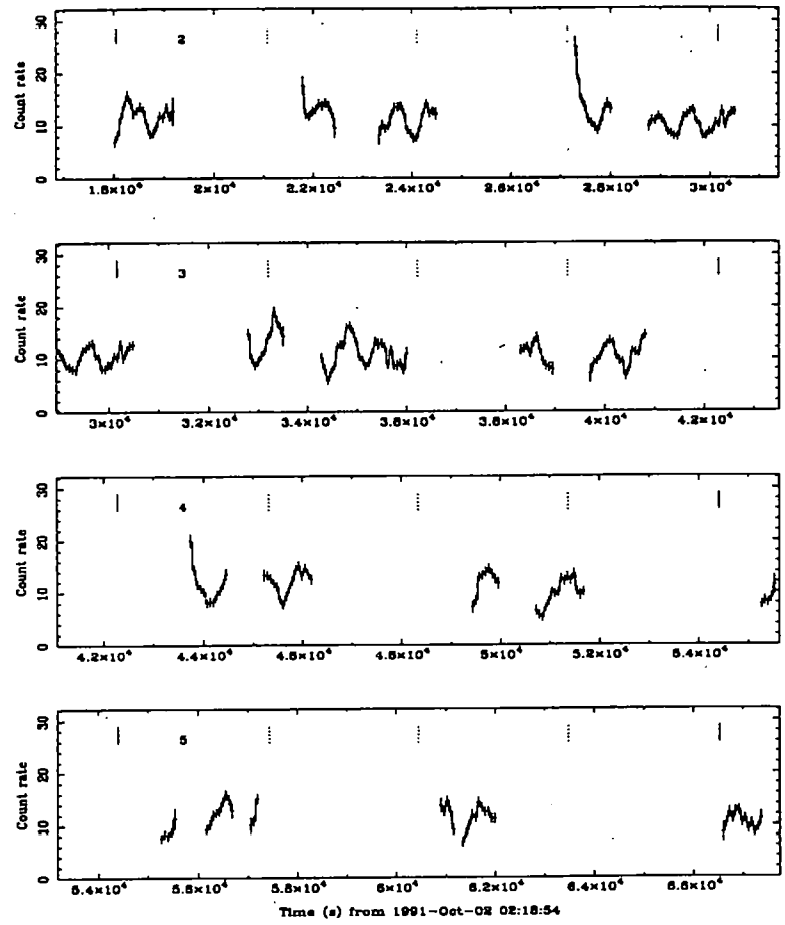

Figure 3.8: The *Ginga* lightcurve for V1223 Sgr in the energy range 1.7 – 2.4 keV. Vertical tick-marks are as for figure 3.1 and the numbers indicate orbital cycle from the start of the observation.

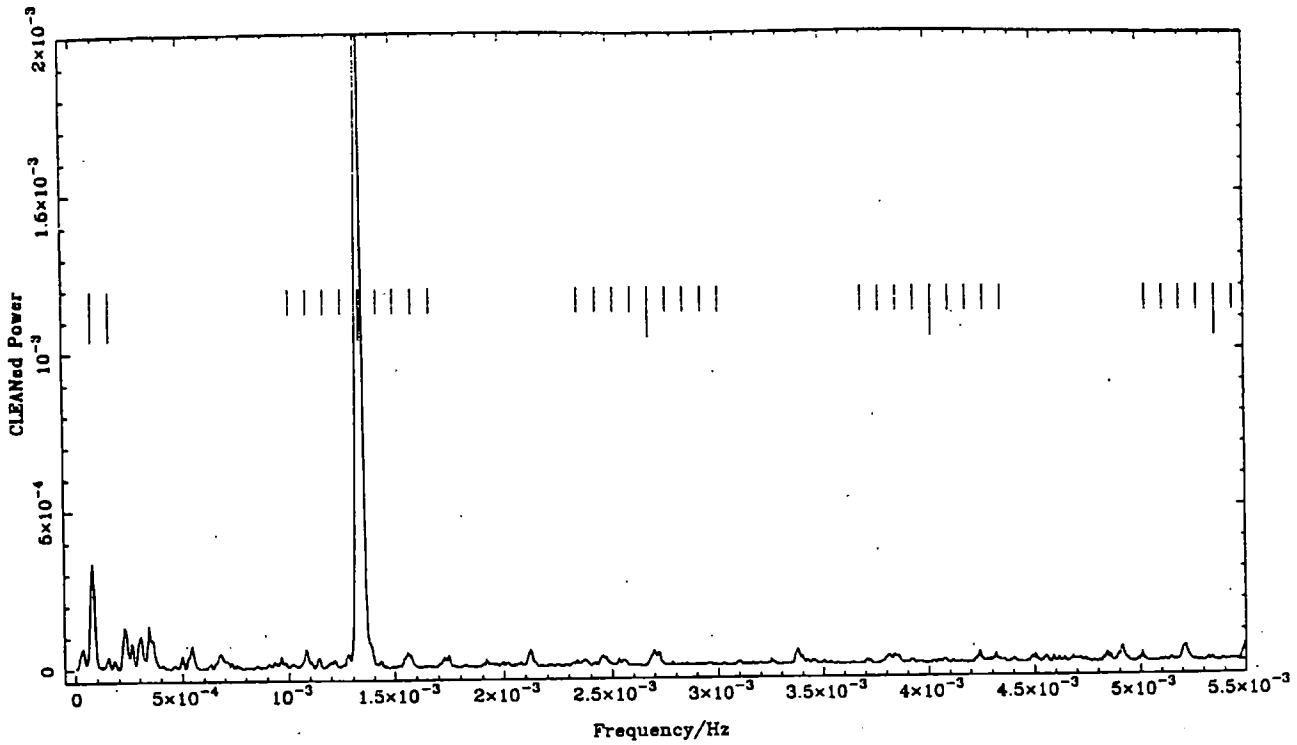

Figure 3.9: *ROSAT* Power spectrum for V1223 Sgr in the energy range 0.2 – 2.0 keV.

3.4 Interpretation

3.4.1 Spin pulse modulation depths

The modulation depths for the pulse profiles illustrated in figure 3.6 were calculated by finding the best fit sinusoid to each, using the Marquardt algorithm as described in Bevington & Robinson (1992). The fitting parameters are given in table 3.2, and the calculated modulation depths are listed in table 3.3.

Taking as an example the *ROSAT* observation of AO Psc at orbital maximum (the first line in table 3.2), with the fitting curve $A\sin(\omega t - \phi) + B$, putting X_H = flux maximum value and X_L = flux minimum value, the modulation depth is:

$$\begin{aligned} MD &= \frac{X_H - X_L}{X_H + X_L} \\ &= \frac{A}{B} \\ &= (0.121 \pm 0.01)/(0.153 \pm 0.007) \\ &= 0.79 \pm 0.07. \end{aligned} \tag{3.1}$$

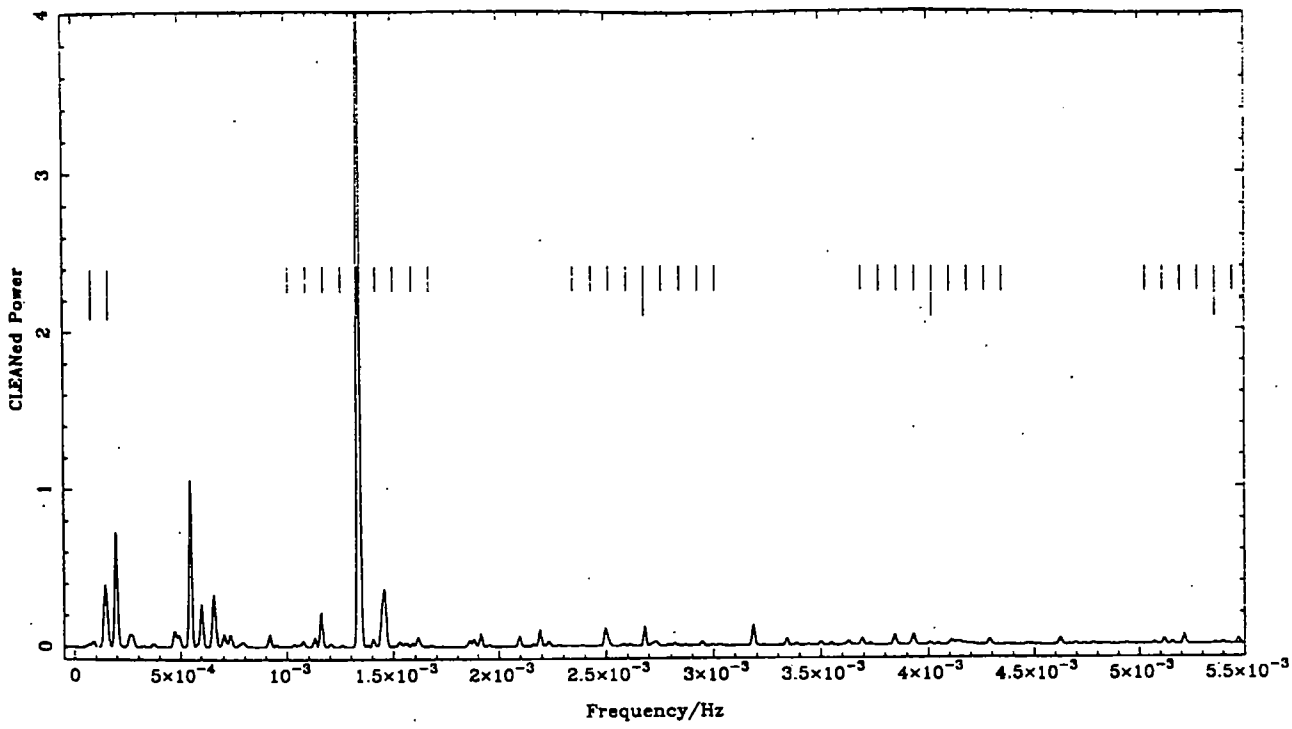

Figure 3.10: *Ginga* Power spectrum for V1223 Sgr in the energy range 1.7 – 4.1 keV. The peaks from about 5×10^{-4} to 7×10^{-4} are thought to be a consequence of the intermittent coverage (c.f fig 3.7) of the signal, which has not been completely removed by CLEAN.

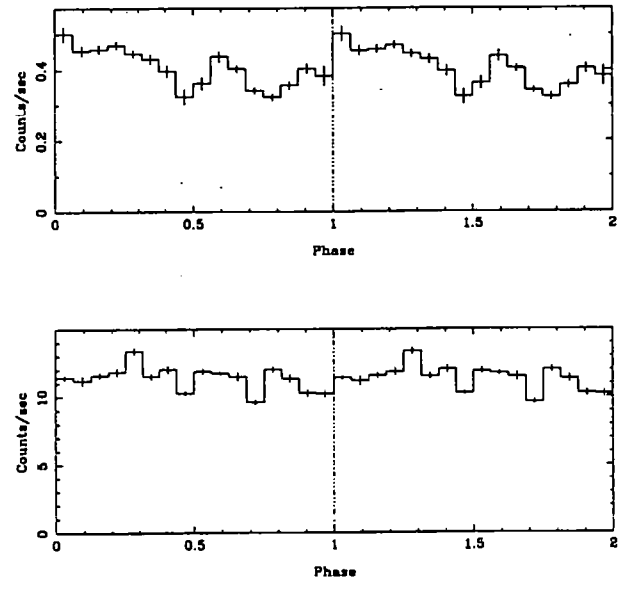

Figure 3.11: V1223 Sgr data folded at the orbital period. The upper panel shows the *ROSAT* data and the lower panel shows the *Ginga* data in the energy range 1.7 – 4.1 keV.

Table 3.2: AO psc Sinusoid fit parameters

Spin fold	Energy range /keV	Amplitude	Average	dof	χ^2_ν
AO Psc[1]	0.2 – 2.0	0.121 ± 0.010	0.153 ± 0.007	7	2.556
AO Psc[1]	1.7 – 4.1	2.638 ± 0.119	4.717 ± 0.084	17	2.327
AO Psc[1]	4.1 – 6.4	1.544 ± 0.111	5.066 ± 0.079	17	3.215
AO Psc[1]	6.4 – 9.8	0.759 ± 0.099	3.655 ± 0.070	17	1.476
AO Psc[1]	9.8 – 18.6	0.116 ± 0.088	1.203 ± 0.062	17	1.035
AO Psc[2]	0.2 – 2.4	0.037 ± 0.008	0.065 ± 0.006	7	1.009
AO Psc[2]	1.7 – 4.1	1.983 ± 0.148	3.604 ± 0.107	17	1.739
AO Psc[2]	4.1 – 6.4	1.533 ± 0.141	$4.523 \pm 0.1.2$	17	1.881
AO Psc[2]	6.4 – 9.8	0.907 ± 0.126	3.230 ± 0.091	17	1.200
AO Psc[2]	9.8 – 18.6	0.170 ± 0.114	1.102 ± 0.083	17	0.564
V1223 Sgr	0.2 – 2.4	0.100 ± 0.008	0.407 ± 0.006	7	1.867
V1223 Sgr	1.7 – 4.1	2.633 ± 0.138	11.238 ± 0.097	13	4.255
V1223 Sgr	4.1 – 6.4	1.816 ± 0.126	12.687 ± 0.089	13	5.648
V1223 Sgr	6.4 – 9.8	0.923 ± 0.113	9.829 ± 0.080	13	3.514
V1223 Sgr	9.8 – 18.6	0.307 ± 0.097	4.162 ± 0.069	13	1.459

[1] Orbital max

[2] Orbital min

Table 3.3: Percentage spin modulation depths=$(X_H - X_L)/(X_H + X_L) \times 100\%$. Uncertainties quoted are at the 68% confidence level.

Energy range/ (keV)	AO Psc (orb. max.)	AO Psc (orb. min.)	V1223 Sgr
0.2 – 2.4	79 ± 7	57 ± 13	25 ± 2
1.7 – 4.1	56 ± 3	55 ± 4	23 ± 1
4.1 – 6.4	31 ± 2	34 ± 3	14 ± 1
6.4 – 9.8	21 ± 3	28 ± 4	9 ± 1
9.8 – 18.6	10 ± 7	15 ± 10	7 ± 2

The large relative errors for the highest energy band indicate the poor quality of the data, or that these spin folds are not well fit by a sinusoid. Figure 3.12 shows the fitting for two profiles.

For both objects, the modulation depths decrease with increasing energy, a trend to be expected if photoelectric absorption is a dominant cause of the spin modulation. However, for both systems we find that it is not possible to model the dependence of the modulation depth on energy using a single absorber whose density varies with spin phase. For example, taking the AO Psc modulation depth (0.79 ± 0.07) at orbital maximum from the low energy band, and averaging E at $\sim$1.5 keV,

$$\Delta\tau = 6.65 \times 10^{-22}(1 + 600E^{-2.7})\Delta N_H, \quad (3.2)$$

$$= 1.3 \times 10^{-20}\Delta N_H. \quad (3.3)$$

From the modulation depth equation,

$$\exp(-\Delta\tau) = (1 - MD)/(1 + MD)$$

$$= (0.21 \pm 0.07)/(1.79 \pm 0.07)$$

$$= 0.12 \pm 0.04.$$

$$\text{so } -\Delta\tau = \ln(0.12 \pm 0.04)$$

$$\Delta\tau = 2.1^{+0.4}_{-0.3}, \quad (3.4)$$

$$\text{giving } \Delta N_H = 7.7 \times 10^{18} \times 2.1^{+0.4}_{-0.3}\text{cm}^{-2}$$

$$= 1.6^{+0.3}_{-0.2} \times 10^{19}\ \text{cm}^{-2}. \quad (3.5)$$

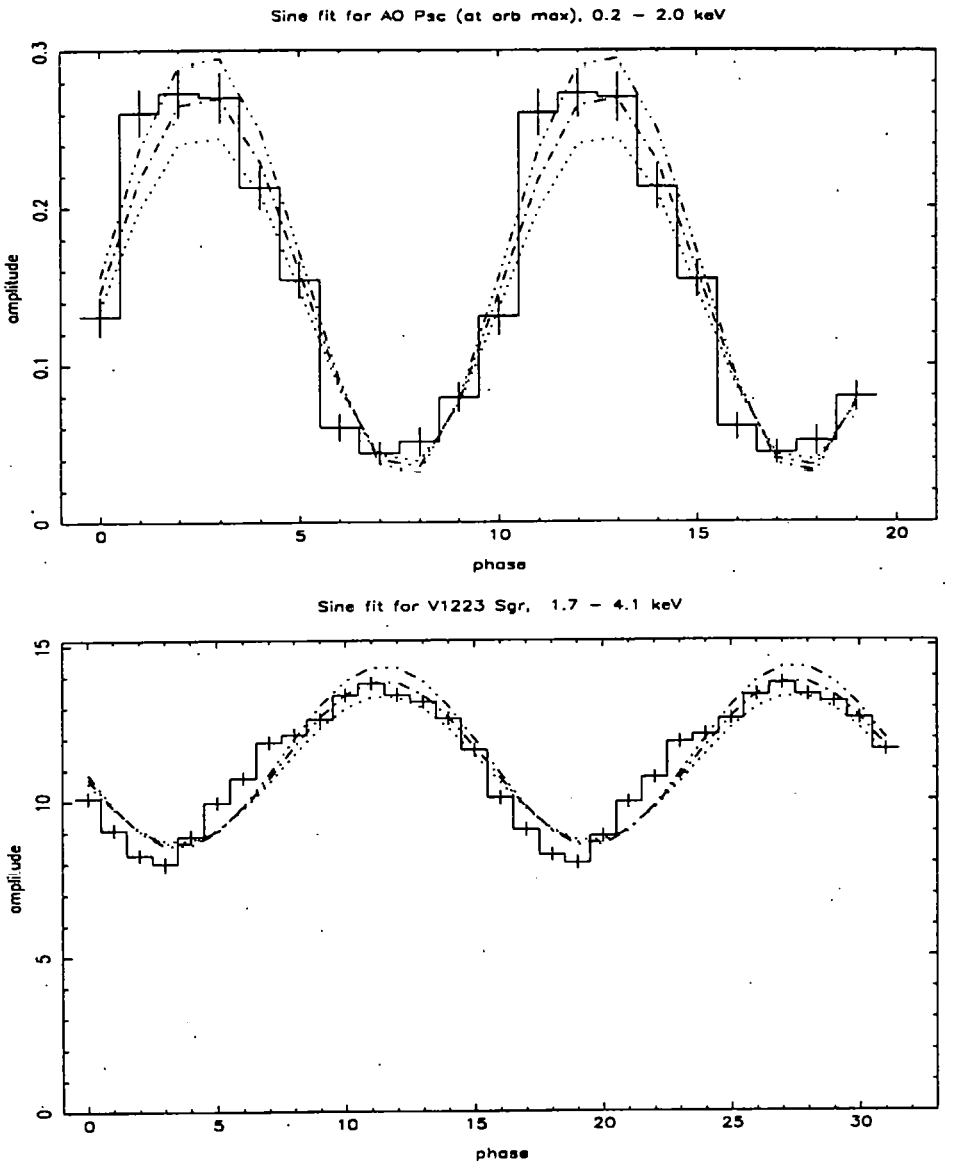

Figure 3.12: Sinusoid fits for (top figure) the (*ROSAT*) spin profile of AO Psc at orbital maximum, energy range 0.2 – 2.0 keV, $\chi^2_\nu = 2.56$; (bottom figure) the *Ginga* spin profile of V1223 Sgr, energy range 1.7 – 4.1 keV, $\chi^2_\nu = 4.25$.

In contrast, taking the fourth modulation depth for AO Psc at orbital maximum, that is in the energy band 6.4 - 9.8 keV (averaging at ~8 keV), the modulation depth is 0.21 ± 0.03, and a similar calculation gives

$$\Delta N_H = 2.0 \pm 0.3 \times 10^{20} \text{ cm}^{-2}. \quad (3.6)$$

Thus the maximum column density consistent with the low energy data is 1.9×10^{19} cm^{-2}, while the minimum consistent with the other band is 17×10^{19} cm^{-2}.

Thus the change in density required to produce the observed modulation at high energies would predict much greater modulation depths (approaching 100 %) in the *ROSAT* band. Conversely, the change in density needed to produce the low energy modulation would give a far lower modulation depth in the higher energy *Ginga* bands than is observed. This discrepancy cannot be explained by the fact that the two datasets for each object were obtained at different epochs, since the *Ginga* pulse profiles are themselves inconsistent with a single phase-varying absorbing column. We conclude that effects such as occultation and/or partial covering of the source of the emission must be included to explain these results. This is similar to conclusions based on earlier *EXOSAT* observations of intermediate polars, including both AO Psc and V1223 Sgr (Norton & Watson 1989).

Recently, Hellier et al (1996) have found that partial covering is required to model their far superior *ASCA* data for AO Psc. In such a model, some of the emission emerges through a non-varying absorbing column, whilst the remainder experiences an absorption whose effect varies as a function of spin phase.

For AO Psc, there is no evidence for a difference in the fractional modulation depths between orbital maximum and orbital minimum in the *Ginga* data. This is consistent with the orbital dips being caused by an additional photoelectric absorption that acts throughout the whole spin cycle, but over only a limited range of orbital phase. In the *ROSAT* data, however, there is marginal evidence for a difference in modulation depths.

3.4.2 Orbital modulation

The orbital folds derived from the *ROSAT* and *Ginga* AO Psc data (figure 3.5) show dips at phase ~ 0.8, which are similar to those noted by Hellier, Garlick & Mason (1993) using *EXOSAT*. However, these *ROSAT* data appear to show a dip superimposed on a roughly sinsusoidal shape which spans the whole cycle. Given its absence in the *Ginga* data this

sinusoidal feature may either be a transient phenomenon, or its amplitude may simply vary with energy.

An interpretation of this is that the dips are caused by a localized absorber above the disc plane, corresponding to the stream impact with the edge of the disc, and locked with respect to the binary period. Indeed the *ASCA* data of Hellier et al (1996) have recently confirmed this suggestion by showing that the dip spectrum requires an additional column density of 5×10^{21} cm^{-2}. The sinusoidal component to the modulation may be due to absorption in a structure that is azimuthally extended around the accretion disc: such a model is considered likely on physical grounds by Patterson (1994). The dip is coincident with the minimum of the sinusoidal modulation, which suggests that material is thrown up at the hotspot, from where it is spread by the magnetosphere. Patterson notes that this would not be expected to produce *stable* dips and indeed the *ROSAT* lightcurve for AO Psc shows tentative evidence that the dips vary from cycle to cycle.

The V1223 Sgr *ROSAT* orbital folds show no stable modulations. However, the dip at phase ~ 0.75, which was tentatively reported in the *EXOSAT* low energy band ($0.05 - 2$ keV) by Hellier et al (1993), is present during some cycles of the *ROSAT* lightcurve. This dip is not convincingly present in the *Ginga* data, so may be sensitive to energy or may reflect secular changes when the time gap between the two sets of observations is considered.

Again a possible model for the orbital dips in the *ROSAT* data is an absorber, fixed in the orbital frame, above the disc plane. However the data do not show an extended azimuthal effect. Considering this, and the inconsistent nature of these dips, it is possible that the inclination angle of V1223 Sgr is just sufficient to allow the fringes of the absorber to obscure the emission region during some cycles.

If the absorbing material is located around the rim of the disc, then the inclination angle of V1223 Sgr may be constrained somewhat using this scenario. Note, however, that the result will be speculative without firm values for the magnetic radius and the extent of the absorber above the disc plane. For example, using the estimates by Lubow (1989) for the height of the absorber ($\sim 2 - 3\times$ the disc thickness), say 10^9 cm, and assuming the outer disc radius to be $\sim 10^{10}$ cm, the inclination angle (i) is $\sim \arctan 0.9 = 84°$. However, no evidence for an eclipse by the secondary is seen in V1223 Sgr, suggesting that $i \sim 80°$ is an upper limit.

This estimate for i differs from that calculated by Penning (1985), who used spectroscopic analysis, in particular the (orbital) phase lag of the H and He II lines to infer a value for $q = M_s/M_p$ (where M_p, M_s = masses of primary, secondary respectively in his symbolism). He then argues for an inclination of from 15.2°–27.2°.

Considering this, and the fact that the large number of intermediate polars showing orbital dips implies that a disproportionate number require a high inclination, an alternative scenario may be that there is an orbitally-fixed absorber closer to the white dwarf. Such a possibility is suggested by Hellier (1997), wherein the stream impacts the magnetosphere (near the *inner* edge of the disc) and material is again thrown out of the disc plane. If this is so, the argument above used to obtain the inclination angle of V1223 Sgr is not valid, and that dips cannot be relied on to give reliable values for i. However, if this were to occur, we should expect a significant signal at the beat period, consistent with some disc-overflow accretion, and the data here show no firm evidence for this. Therefore we reject this possibility, and consider the results to indicate a higher inclination than that estimated by Penning.

In relation to this, Armitage & Livio (1996) used Smooth Particle Hydrodynamics simulations to study the disc-stream interaction, and calculate the density of the stream and its height (z) above the disc plane at various radii and azimuthal angles. In their simulation, the density falls off at high z values for smaller radii, so even granting a disc-overflow, the effect may not be significant. Their results indicate that the stream density would be sufficient to cause a dip at elevation angles (above the disc plane) of up to 12°, equivalent to $i = 78°$.

3.5 Conclusions

AO Psc and V1223 Sgr are remarkably similar systems in many respects. Previous studies, using *EXOSAT*, revealed that they both show clear X-ray modulations at their respective white dwarf spin periods, the amplitudes of which decrease with increasing energy. Searches for orbital modulation in the two systems suggested a possible difference, in that AO Psc showed definite orbital dips at around phase 0.8 in the orbital cycle, whilst the evidence for similar dips in V1223 Sgr was somewhat tentative (Hellier, Garlick & Mason 1993). The power spectra of both these systems show little evidence for a signal at the beat period, indicating that the accretion must be predominantly via a disc in both systems.

For AO Psc, we provide further evidence for dips at about orbital phase ~ 0.8 in the medium energy X-ray band. These dips can be modelled by an absorber above the disc plane, fixed in the binary frame. We find that similar dips occur in the *ROSAT* data at energies < 2 keV and, in addition, there is a sinusoidal component to the modulation at these energies. This provides evidence for an absorbing structure that extends around the whole circumference of the accretion disc.

The *ROSAT* data presented here provide the first firm evidence that V1223 Sgr also shows orbital dips in its lightcurve. The variable nature of these dips suggests that the absorption producing them is intermittent. This can be used to place limits on the system inclination angle by assuming that the line of sight just grazes the absorbing structure in some cycles. By making plausible assumptions for the extent of the disc structures, we determine an inclination angle of around 80°. The coverage provided by the *Ginga* data is insufficient to determine whether these dips are present at higher energies.

Our findings confirm that AO Psc and V1223 Sgr continue to show pulsations in the medium energy X-ray band (as for *EXOSAT*), and now provide the clearest detection of pulsations at energies < 2 keV in each system. Also we confirm that spin modulation depths continue to increase to lower energies and that single column densities which vary with spin phase are insufficient to produce the pulse profiles.

Chapter 4

The computer model

The aim of the work reported in this thesis is to simulate X-ray light curves of intermediate polars (using a FORTRAN program), and so to constrain physical parameters relating to accretion and emission mechanisms in them. This chapter considers details of the model, starting with a brief overview of the original program, and gives several enhancements to it, largely relating to tying the model as coded to physical models of intermediate polars as known. The factors described include geometrical situations, for instance the angle of the incoming stream to the magnetic field lines; optical depths (through the accretion curtain) in various directions; cell luminosity; offset dipoles; and accretion geometry as related to magnetic capture radii. At the end a description of the main functions of the program is given.

The next chapter looks at results.

4.1 Original program

The original program, from which the current project developed, is described in Norton (1993); an overview is provided here.

The idea is to define small "cells" within the accretion envelopes (the circular regions around the magnetic poles of the white dwarf close enough for accretion to take place at various phases), calculate which are visible at consecutive timesteps (i.e. incrementing the spin

phase slightly), then derive the optical depth through the accretion curtain along the line of sight, thus allowing attenuation of the original X-ray luminosity to be calculated. The results for individual cells are summed for a particular timestep, then for both poles, and the results output to a time series file.

4.1.1 Input parameters

The program firstly lists out default values for the run parameters, and invites the user to change any of these. These parameters were:

Symbol	Parameter	description
p_{spin}	PSPIN	White dwarf spin period (sec)
p_{orb}	PORB	System orbital period (sec)
i	ANGI	Inclination angle (degrees)
m_n	ANGM(N)	Magnetic colatitude (degrees)
N_H	NHSTREAM	Extra hydrogen column density due to accretion stream ($\times 10^{21}\mathrm{cm}^{-2}$)
	NPC	No. of polecaps
	PCQ	Polecap usage - 1: upper pole only; 2: lower pole only; 3: both used
	NTIME	No. of time bins in lightcurve
Δt	TBIN	Time bin size (seconds)
	NPHASE	No. of phase bins in each fold
ΔA	DELA	Fraction of surface area covered by a single cell
E	ENERGY	Pseudo energy value to get varying absorption (keV)
	FLUX(N)	Relative flux per unit area from the emission regions
f	FRAC(N)	Fraction of surface area covered by polecap discs
f'	RFRAC(N)	Fraction (0–1) of rings emitting (to get number of annuli)
f''	CFRAC(N)	Fraction(0–1) of each annulus emitting (to get azimuthal spread of arcs)
	SCEN(N)	Angle of centre of distribution of cells in any ring with respect to the line between axis and centre of region (degrees)

Parameter table continued...

Symbol	Parameter	description
δ	AMAX†	Maximum possible fraction of total accretion onto any single pole at any instant ($0.5 < \mathrm{AMAX} < 1.0$)
	†	Original symbol 'FLIP'; changed to more descriptive name

After this initialisation, it calculates various quantities which remain constants through the run, then loops through a number of timesteps (NTIME) in which the spin and orbital phases alter according to p_{spin} and p_{orb}.

Each accretion envelope – a circle centred on a magnetic pole – is analysed into a number of cells, small circles of equal area which are arranged in concentric rings around the pole. Each cell has a "ring number", and a "cell-number" within the ring. This is shown schematically in figure 4.1, where the approximation to a flat circle is used.

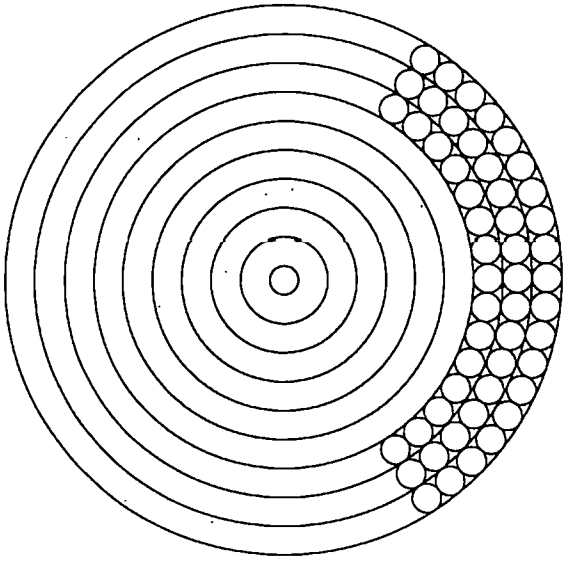

Figure 4.1: The geometry of the accretion envelope, with the annuli and accreting cells shown. In this case the value of f' would be ~ 0.3, reflecting the number of annuli accreting, and the value of f'' would be $\frac{1}{3}$, giving an azimuthal spread of 120°. For the parameters used in testing (Chapter 5) the accretion actually takes place starting at around the 28th annulus or thereabouts.

These enable azimuth and colatitude angles in the magnetic pole frame to be allocated, which are then used in the transformation to the observer's frame. The number of rings depends on the area of the emission region and the area of each cell (both of which give the relevant angular size). Each cell subtends an angle

$$\Delta\phi = \arccos(1.0 - (2.0\Delta A)) \tag{4.1}$$

at the white dwarf centre. The number of rings up to the inner and outer edges of the arc is

$$NRINGS(q) = \mathrm{INT}((\beta_{pq}/\Delta\phi) + 0.5), \tag{4.2}$$

where β_{pq} is the angle of the accretion arc edge from the magnetic pole, as subtended at the white dwarf centre. (p is the pole number; q=1 for the inner edge and 2 for the outer edge.) The number of cells within ring number n works out as

$$NCELLS(n) = 2n - 1. \tag{4.3}$$

Not all of these cells will be accreting in the arc-shaped accretion model. Further, some or all may be occulted by the limb of the white dwarf, and at some inclinations are never visible (in the case of the lower pole).

At each timestep phase-dependent calculations are carried out, particularly the position of each cell in the observer's frame, and as a consequence the line of sight through the absorbing curtain. This allows the attenuation due to absorption from the cell to be calculated. The transformation is described in the next subsection, and a discussion of the absorption calculation is given in section 4.7, with the modifications done since 1993.

The parameter $AMAX$ (symbol "δ") is defined so that the amount of disc and stream-fed accretion is determined by a single parameter as follows: assume the fraction of material accreting via the disc is D, which takes a value between 0 (stream-fed only) and 1 (disc-fed only), and the fraction accreting via the stream is S, so $D + S = 1$. It is assumed that the disc-fed proportion feeds the same amount to each pole, so each receives $0.5D$ at all times, since there is no reason to favour either pole. The stream-fed proportion, however, varies in the amount feeding to each pole depending on the beat phase. For example, if it is assumed to feed 100% to the (currently) nearer pole (so "flips" at each $\frac{1}{2}$-beat cycle), the nearer pole receives a fraction $0.5D + S$ of the total accretion, whereas the farther pole gets $0.5D$. Thus $AMAX$, the maximum fraction of the accretion either pole can possibly receive at any phase, is $\delta = 0.5D + S$. Thus when $\delta = 0.5$ implies $S = 0$ and $D = 1$, whereas $\delta = 1.0$ implies $S = 1$ and $D = 0$. Values of δ between 0.5 and 1.0 (the only valid values) give the

corresponding disc/stream-fed proportions, with $D = 2(1-\delta)$ and $S = 2\delta - 1$. How the stream-fed distribution varies with the beat phase is not known; the original model had it varying as the cosine of the angle between the line joining the stars and the dipole axis, but we consider later the possibility of it depending on the angle between the stream and the magnetic field at the capture radius (Section4.5).

4.1.2 Transformation of frames

The transformation as described applies to both the old and new versions of the model. The location of any cell is first of all specified in relation to its magnetic pole, using angles ϕ_{cell} and θ_{cell}. The x_m-z_m plane is determined by the lines from the white dwarf centre (the origin) to the spin and magnetic poles, with the spin pole coincident with the z_m-axis. Three transformations are carried out to obtain its aspect in the observer's frame.

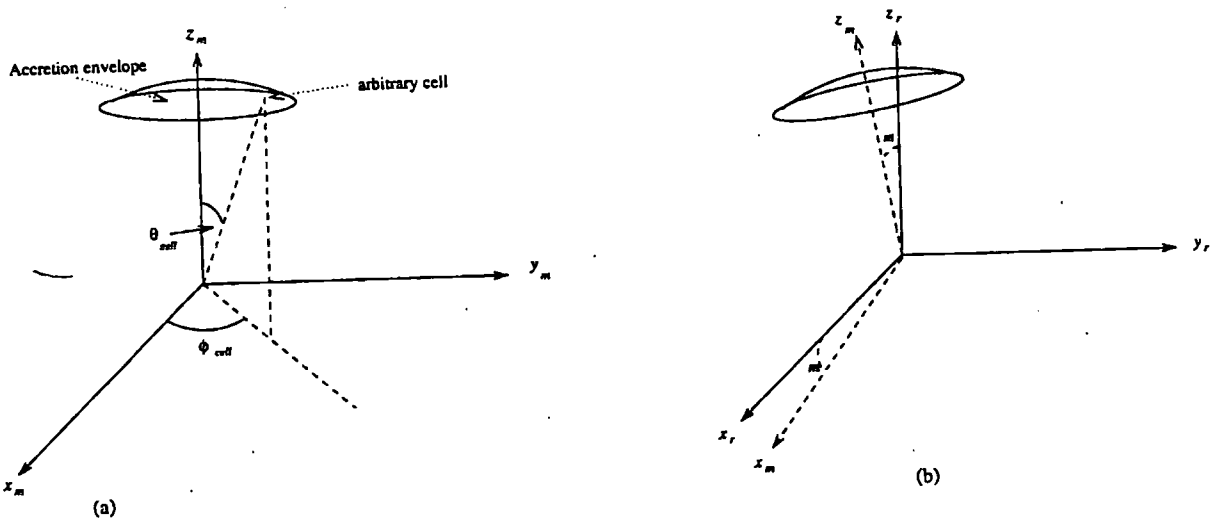

Figure 4.2: (a) Location of cell in magnetic frame. (b) Transformation from magnetic pole frame to spin frame: rotate about the y_m-axis through m.

(1) The location in the magnetic frame has cartesian coordinates (Figure 4.2 (a)) :-

$$x_m = \cos\phi_{cell} \sin\theta_{cell}$$

$$
\begin{aligned}
y_m &= \sin\phi_{cell}\sin\theta_{cell} \\
z_m &= \cos\theta_{cell}.
\end{aligned}
$$

(2) The system is transformed to the spin (rotational) frame. (Figure 4.2 (b).)

$$
\begin{aligned}
x_r &= x_m\cos m + z_m\sin m \\
y_r &= y_m \\
z_r &= -x_m\sin m + z_m\cos m.
\end{aligned} \tag{4.4}
$$

(3) Then it is rotated through the spin phase angle, $\phi_{spin} = \omega_s t$, where $\omega_s = 2\pi/p_{spin}$ and

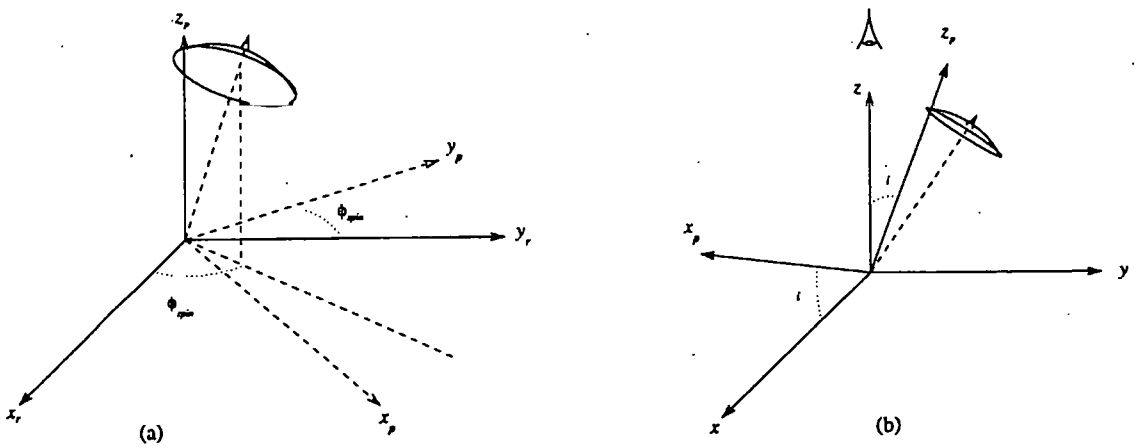

Figure 4.3: (a) Rotate about the z_r-axis through spin phase angle. (b) Transform to observer frame: rotate about y_p-axis through i.

$t = \Delta t \times$ the current timestep. (Figure 4.3 (a).)

$$
\begin{aligned}
x_p &= x_r\cos\omega_s t - y_r\sin\omega_s t \\
y_p &= x_r\sin\omega_s t + y_r\cos\omega_s t \\
z_p &= z_r.
\end{aligned} \tag{4.5}
$$

(4) The spin axis is rotated through the inclination angle so that the new z-axis coincides with the line of sight. (Figure 4.3 (b).)

$$
x = x_p\cos i - z_p\sin i
$$

$$
\begin{aligned}
y &= y_p \\
z &= x_p \sin i + z_p \cos i.
\end{aligned} \tag{4.6}
$$

Transformations (1), (3) and (4) are passive transformations, i.e. simply changes of frame, whereas (2) is a rotation of the system.

The next several sections discuss the updates to the model and the theory behind them.

4.2 A symbol reference list

Much of the following is algebraic manipulation. For convenient reference we list here a summary of the symbols used throughout the chapter.

The variables used in the calculations by the program are:-

Angles

ϕ_{spin}	Spin phase angle
ϕ_{orb}	Orbital phase angle
ϕ_{beat}	Beat phase angle
i	Inclination
m_p	Magnetic colatitude of pole p
γ	Lower pole azimuthal lag
ϵ	Stream incident angle to radius (fig 4.8)
ϕ_{cell}	Azimuthal angle of current cell in magnetic pole frame
θ_{cell}	Colatitude of cell in magnetic pole frame
ψ	Angle of stream to magnetic field at R_{mag}
λ	Line of sight to cell in magnetic pole frame
μ	Elevation angle of line of sight from cell relative to white dwarf surface
ξ_p	Angle between magnetic pole p and x-axis in section 4.5.2
α	Half-angle subtended by accretion arc at magnetic pole
Λ_{mn}	Angles to corners of arc (used in calculation of λ)

β_{pq} Angle of edge of accretion arc from pole
(p=polecap; q=1: inner edge; q=2: outer edge)

ζ_{pq} Incident angle of above to white dwarf surface

Areas

f_p Polecap area relative to white dwarf surface area
(=total accretion area in the filled cylinder case)

f'_p Fraction of rings accreting; the size of each ring
is determined by the size of ΔA.

f''_p Azimuthal spread of accreting arc relative to a full circle;

A_p Area of emission region. Choosing $f'_p = f''_p = 1.0$ makes
the emission region a filled circle rather than an arc.

Terminology: Polecap area (or accretion envelope) refers to the circular region
centred on the polecap in which the accretion takes place.
Emission region is the (arc-shaped) splashdown area, or "footprint"
of the accretion curtain,i.e. the high-temperature shock which
emits the X-rays. These are related by: $A = f\,f'\,(2 - f')\,f''$.

σ Emission area / polecap area: $\sigma = f'\,(2 - f')\,f''$.

Other variables

δ AMAX: the disc-stream parameter.

τ Optical depth in various directions:

- τ_h - horizontally (parallel to the white dwarf surface)

- τ_v - vertically (normal to the white dwarf surface) .

- $\tau(\mu)$ - at an arbitrary elevation angle μ.

M_* Mass of star in solar mass units.

$\dot{M}_{17}$ Accretion rate in units of 10^{17} g s^{-1}.

$R_{mag}(q)$ Magnetic capture radius:
$q = 1$ gives outer radius;
$q = 2$ gives inner radius;

R_* White dwarf radius (units = cm unless stated otherwise);

a_1 Distance of inner edge of emission region from magnetic pole;

a_2	....ditto for outer edge; note $a_q = \beta_q R_*$;
a	....ditto for an individual cell in the emission region.
d_x	Distance of cell from curtain edge (the subscript x differs depending which calculation is being done).
D_H	Horizontal distance from cell through the absorbing curtain along the line of sight; allows for re-entering the curtain at some angles. Used in section 4.10.

4.3 Magnetic colatitudes and capture radii

The original program simply gave the dimensions of the accretion arc as free parameters, in terms of f (the fractional area of the accretion envelope around the polecap), f' (the fraction of rings accreting, included for non-cylindrical accretion columns), and f'' (the angle subtended by the arc, relative to 360°). This gives a total of six free parameters, three for each pole, identifying the accretion geometry for the dipole case.

We now attempt to tie these parameters to what may be considered to be physical considerations, using the white dwarf radius, the inner and outer magnetic capture radii, and the magnetic colatitudes. These five system parameters should replace the six arbitrary original parameters.

Actually, the white dwarf mass is chosen to be the independent parameter, and its radius is determined by Neuenberg's empirical formula

$$R_*(/\mathrm{km}) = 7800\left[\left(\frac{1.44}{M_*}\right)^{2/3} - \left(\frac{M_*}{1.44}\right)^{2/3}\right]^{1/2}, \tag{4.7}$$

where R_* is the white dwarf radius, in this case in km, and M_* its mass in solar mass units. A more complete magnetohydrodynamic theory may be able to fix the capture radii in terms of magnetic moment and accretion rate, reducing the parameters by one again (as accretion rate is a necessary parameter already).

The essence of this method is to assume that the flow follows the (roughly dipole) field lines from the capture radii. In this we assume that the material threads on to field lines not at a unique radius, but over a range of radii, and define the inner and outer capture radii as limiting where the bulk of the accretion takes place. If the material then follows the field lines from these, the result will be the accretion curtain splashing down on the white dwarf

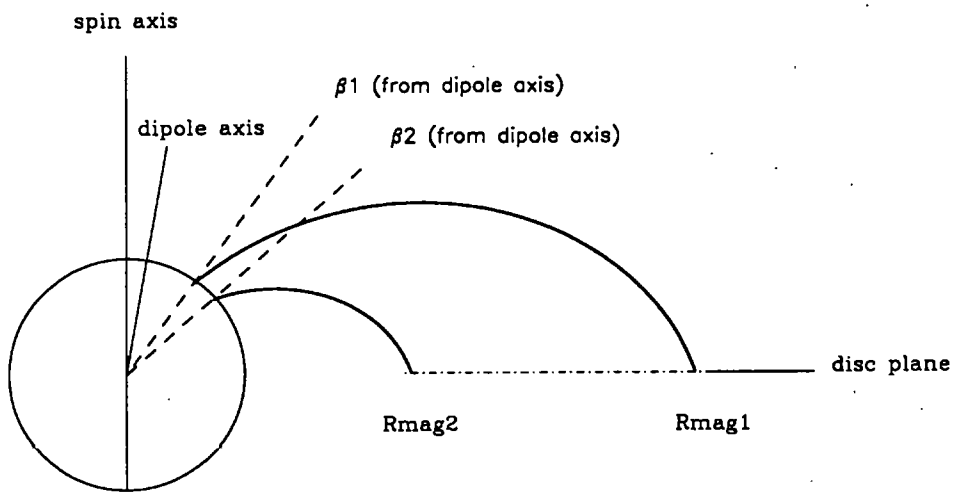

Figure 4.4: Relation between magnetic capture radii and β_1, β_2. Note that the *outer* capture radius corresponds with the *inner* edge of the accretion arc, and vice versa.

and defining the bright footprint, or emission region, which will be arc-shaped to match the cross-section of the curtain. It should also be noted that the *outer* capture radius ($R_{mag}(1)$) links to the *inner* edge of the arc, and vice versa (see figure 4.4). So to calculate the inner and outer edges of the arc from the pole, we use the dipole geometry, that is, given a dipole field line from the inner or outer capture radius, at any azimuth, we follow it down to the white dwarf surface, and calculate the angle β from the magnetic pole, which is given by

$$\sin^2 \beta = (R_*/R_{mag})(1 - \sin^2 m \cos^2 \phi_{azi}) \tag{4.8}$$

(adapted from Kim & Beuermann, 1994).

Here, m is the magnetic colatitude, R_{mag} the capture radius, and ϕ_{azi} is the azimuthal angle difference between the capture point and the pole, relative to the spin axis. In our simulation, we ignore the azimuthal angle as having a small effect, hence use

$$\begin{aligned} \sin^2 \beta_{pq} &= (R_*/R_{mag}(q))(1 - \sin^2 m_p) \\ &= (R_*/R_{mag}(q)) \cos^2 m_p, \end{aligned} \tag{4.9}$$

where $p = 1$ or 2 mark the poles, and $R_{mag}(q)$ ($q = 1$ or 2) are the outer and inner capture radii respectively (figure 4.4). This approximation is good, giving $\leq 14\%$ difference between any beat phases for $m \leq 20°$, but becoming progressively worse, and giving non-circular accretion envelopes for $m > 45°$. (The value of R_{mag} has little effect on this.) Hence any simulations with $m \geq 25°$ are suspect, having ≥ 20 percent difference between arc radii at different beat phases. Table 4.1 gives the differences from circularity centred on the pole for $R_{mag} = 5R_*$ and $R_{mag} = 15R_*$, representing the outer and inner edges of the accretion envelope.

Figure 4.5 shows how the accretion envelopes become non-circular (from $m \simeq 45°$ onwards); in particular this means that we cannot really use equation 4.8 to get β at high m, as the simulation assumes a circular arc anyway.

Now note the following geometric relations:

$$\begin{aligned} f_p &= \frac{1}{2}(1 - \cos \beta_{p2}); \\ f'_p &= 1 - \beta_{p1}/\beta_{p2}. \end{aligned}$$

Then for $m \lesssim 20°$, equation (4.9) gives the angles of the outer and inner edge of the accretion arc footprint from the magnetic poles, and we get

$$f_p = 0.5 \times (1.0 - \cos \beta_{p2}) \text{ and} \tag{4.10}$$

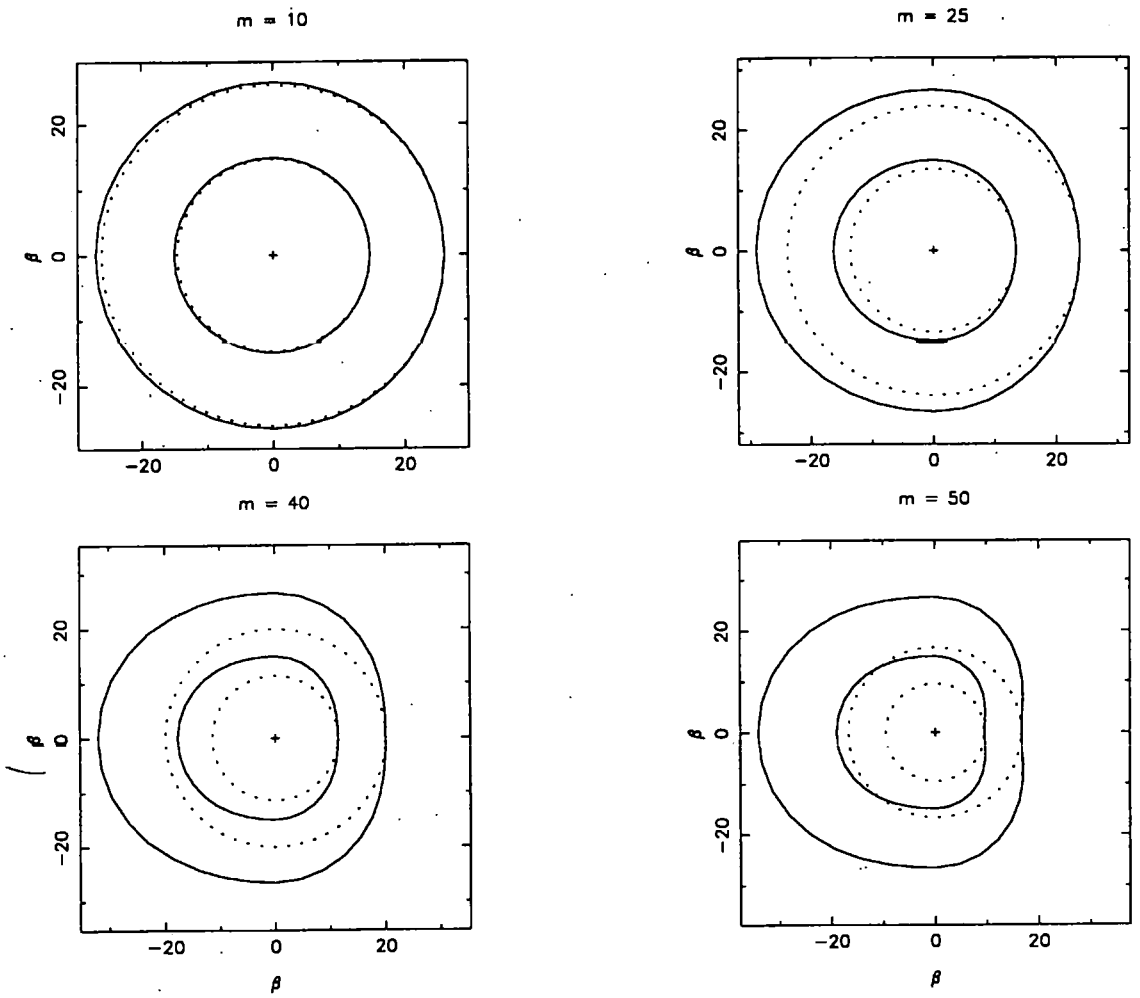

Figure 4.5: The accretion envelopes for various values of m. The full lines show the envelope as defined by equation 4.8; the dotted lines show it as given by the approximation, equation 4.9, which results in a circular region. The crosses mark the magnetic pole, and the axes label the angular spread on the surface.

Table 4.1: Maximum and minimum values of β during the beat phase, as a function of magnetic colatitude.

m	β_{min}	β_{max}	%-age difference	β_{min}	β_{max}	%-age difference
5.0	26.46	26.67	0.82	14.90	15.02	0.78
10.0	26.13	26.99	3.31	14.73	15.19	3.13
20.0	24.85	28.21	13.51	14.04	15.84	12.78
30.0	22.79	30.00	31.66	12.92	16.78	29.86
35.0	21.49	31.03	44.42	12.21	17.32	41.82
...	...	...	...	...	...	.....
85.0	2.23	39.14	1652.29	1.29	21.37	1557.59

Notes:

Columns 2–4 are for $R_{mag} = 5R_*$, columns 5–7 for $R_{mag} = 15R_*$

The values are calculated using equation 4.8; the (constant) value of β for the inner and outer edges using the approximate equation (4.9) are given by β_{min}, i.e. columns 2 and 5

$$f'_p = 1.0 - \beta_{p1}/\beta_{p2}. \tag{4.11}$$

The parameter f'' has now become two parameters, f''_s and f''_d, since it is plausible that stream and disc-fed arcs may not both have the same angular spread. These are still input as independent parameters, although in practice f''_d is usually considered to be 0.5, as the whole circumference of the inner disc edge is expected to feed the accretion curtain. This choice of parameters should allow new developments in theory (magnetohydrodynamics) to be incorporated.

4.4 Offset dipoles

For simplicity, models of intermediate polars tend to deal with one pole, or symmetrically-placed dipoles, although King & Shaviv (1984) did point out that with an occultation-only model, the poles would have to be either offset or of different strengths to avoid cancellation of spin-phase effects. This section considers whether this arrangement could result in all the kinds of spin profiles observed.

The raw light curves of intermediate polars in general will not be symmetric about phase zero over a single spin cycle, at least in the case of a stream-fed component, since the curves depend on factors which may differ in the first half of the cycle from the second half. For example the direction of the stream, amount of absorption (dependent on the aspect to line-of sight), etc. would depend on the orbital phase. However, as argued below, a simple model of such a system *would* produce a mirror symmetry in the spin pulse profile.

4.4.1 The effects of spin-folding.

For a system accreting from a stream, when observing the signal through one spin cycle, the first half of the cycle differs from the second half. The reason for this is that the stream is in a different position relative to the emission region; thus the brightness of the poles differs, as does the amount of absorption. It is not clear that these should balance out, hence we would expect in general that the light curve over a single spin cycle would be asymmetric, at least if there is a significant stream-fed component.

However, for any situation with the upper magnetic pole at some phase $|\phi_{spin}(1)|$ say, and stream entering at phase $|\phi_{orb}(1)|$ (see figure 4.6 (a)), there would be a mirror situation at some other time with the upper magnetic pole at phase $|\phi_{spin}(2)| = |2\pi - \phi_{spin}(1)|$, and stream entering at phase $|\phi_{orb}(2)| = |2\pi - \phi_{orb}(1)|$ (figure 4.6 (b)), to some arbitrary small level of error. This would be expected given a long enough observation, unless some sort of resonance effect prevented the "mirroring". In other words, effects not dependent on the spin phase should cancel out if sufficient cycles are folded, and the spin profile for each pole should be mirror symmetric about phase zero and phase 0.5. In this diagram the observer's viewpoint may include the lower pole, but on average the symmetry about spin phase zero still applies.

If two curves which are symmetric about the same axes are either multiplied or (in the case of diametric opposite poles) added together, the result is also symmetric.

Investigation using the program seems to confirm this (see Chapter 5).

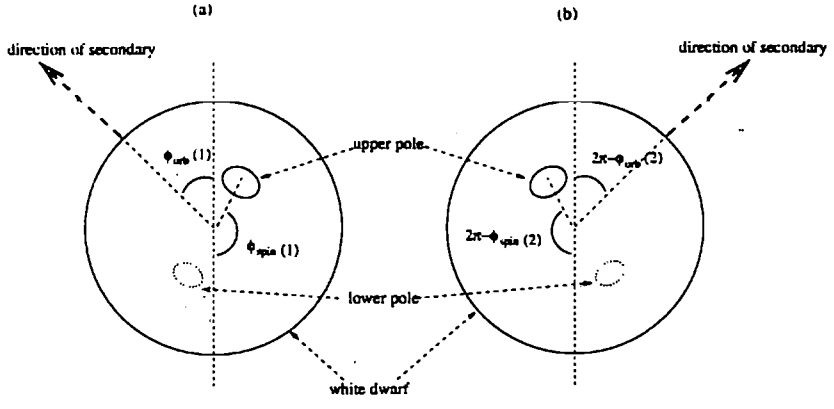

Figure 4.6: Possible configurations of spin and orbital phase for a symmetrically placed dipole: looking down the spin axis on the upper hemisphere. (a) A configuration in the first half of the spin cycle. (b) Its opposite in the second half.

4.4.2 Non symmetric spin folded curves.

The fact that some spin-folded curves (e.g. for FO Aqr) are not mirror symmetric about phase 0.5 suggests that the model using a symmetric dipole fails to match the situation in some intermediate polars.

Possible causes of asymmetry are:

(1) The spin-folded curve for each pole would, as noted above, be symmetric about phase 0.5 (using the model in the program). However if the poles were not diametrically opposite, and varied by an azimuthal angle different from 0° or 180°, the axes of symmetry would not match, hence the resultant sum of the spin-folded curves would in general lose its symmetry.

In the model we introduce the parameter γ, which is the "azimuthal lag" of the lower pole relative to the upper pole. Putting $\gamma = 180°$ (and $m_2 = 180° - m_1$) makes the poles diametrically opposite, which we call a symmetrically placed dipole.

Values of $\gamma \neq 180°$ have been tried using the program and the results do display asymmetry.

(2) The argument about how the spin-folded curve becomes mirror symmetric depends on the randomness of the direction of the stream for any spin phase, in the long run. Therefore if there is any resonance effect between spin and orbital periods, this could invalidate the argument. For example, suppose that the periods were linked by $p_{orb} : p_{spin} = 4 : 1$, in which case the primary would have the same phase as the secondary every $1\frac{1}{3}$ spin cycles $\equiv \frac{1}{3}$ orbital cycles; if the phases happened to coincide at (say) spin phase 0.25, they would also coincide at phases 0.57 and 0.92. If there were a substantial stream-fed component this could lead to a long-term asymmetry between the first and second half of the spin pulse profile.

A slight effect has been obtained using the program, but this is not sufficient to explain the amount of asymmetry seen in the real data.

Note: the system EX Hya shows a near resonance, with $p_{orb} : p_{spin}$ in a ratio of 3 : 2. However, the pulse profiles in this case *are* symmetric. This is still consistent with the previous argument, though, as the lack of a beat signal in this system argues for a predominantly disc-fed mode of accretion. (Caveat: this argument assumes that EX Hya is not in equilibrium.)

(3) An attempt was made to obtain an asymmetry based on the idea that the stream may be "dragged" around slightly between the time it encounters the magnetosphere and the time it hits the white dwarf, due to the white dwarf's rotation. The change of angle caused by this effect is estimated to be about 10° - 20°, using the free-fall time of the material.

The idea was that the function governing the amount of material going to each pole (which depends on $\phi_{spin} - \phi_{orb}$) would not be quite in phase with the function giving the aspect of the accreting regions to the observer (which would be altered by about 15° due to the effect described). The absorption functions would keep phase with the latter. Hence the resulting spin profile would be asymmetric. This has been tried using the program, but the results indicate that any such effect is too small to be significant.

Related to this is the effect of ϵ, the angle of the stream to the line joining the stars. Figure 4.6 assumes the incoming stream to be radial, but it is likely that it will come in at an angle, possibly destroying the symmetry.

(4) As noted in (2), the argument for symmetry depends on the random nature of the stream direction for any spin phase. If a selection effect occurs whereby one part of the orbital cycle

is observed more than the other, this could have an effect.

(5) Our model only takes into account the accretion onto the white dwarf when calculating the light curve, so if the "hot-spot" on any accretion disc were to have an effect at X-ray frequencies this would not be reflected in the program. As the visibility of the hot-spot would vary at the orbital frequency, it seems unlikely to cause spin pulse modulation.

(6) The FO Aqr spin profile (see Chapter 2) at some epochs could be interpreted as roughly sinusoidal with a regular dip at some spin phase. It maight be possible to model this by positing an extra absorber fixed in the spin frame.

4.4.3 Conclusion

The most likely explanation for asymmetry seems to be the non-symmetric dipole. There is of course the possibility of more complicated situations, quadrupoles and so on, but for now it would seem more productive to stick to the simpler case.

To summarise, for the symmetrical spin pulse profiles we assume $\gamma = 180°$. Choosing $m_2 = 180° - m_1$ also would give a dipole with its axis through the white dwarf centre. For non-symmetric spin profiles we choose $\gamma \neq 180°$ or $0°$. Varying m_2 from $180° - m_1$ should not affect the symmetry, but would have other effects, shortening or lengthening the time the lower pole is visible.

4.5 Angle between stream and field lines

The original model had the stream-fed material to each pole varying as $\sin\psi$, where ψ is the angle between the dipole axis and the line joing the two stars. The disc-fed portion was assumed to be constant for the run and shared between the poles, and was (and is) determined in the model by the parameter δ, with $(1-\delta)$ feeding onto each pole via the disc, and $(2\,\delta - 1)$ (total) feeding onto the poles via the stream. (δ − the maximum possible accretion on to any pole.) Hence the amount feeding the upper pole would be $(1-\delta)+(2\delta - 1)\cos^2\psi$, with $(1-\delta)+(2\delta-1)\sin^2\psi$ feeding the lower pole.

It is more plausible, however, that the proportion of stream-fed accretion on to each pole

varies according to the angle of incidence at which the stream meets the magnetic field lines at the magnetic capture radius. This angle may also be called ψ since the original definition is no longer in use, and ψ is calculated at each timestep. Also, options are included to allow the variation to be (1) "flipping" (100 per cent to one pole or the other); (2) sinusoidal ($\propto \cos\psi$); or (3) in between, chosen to be $\propto \cos^{0.1}\psi$, an arbitrary function to provide a variation which is continuous but closer to a step function than a sinusoid. Figure 4.7 shows how these vary in the amount of stream-fed accretion to the upper pole. The lower pole accretion is this subtracted from 1.

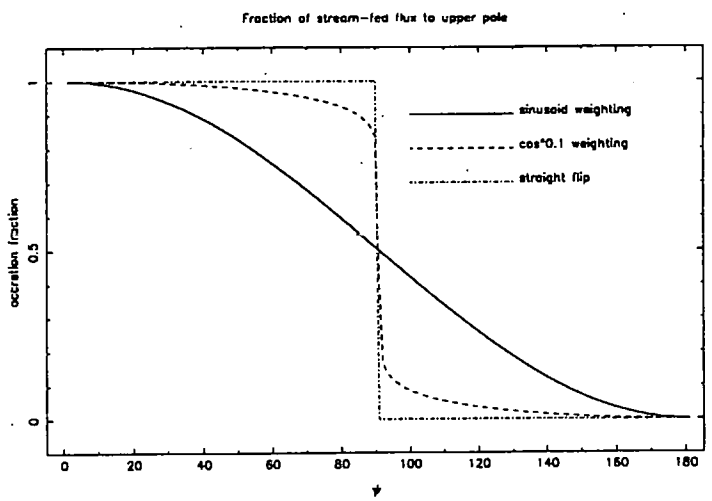

Figure 4.7: The proportion of stream accretion to the upper pole, as a function of the incident angle of the stream to the field, using three different weightings.

The calculation of ψ is now described.

4.5.1 Coordinate system and strategy of calculation

The coordinate system is such that:

(i) The z-axis coincides with the orbital rotation axis (See figure 4.8); the coordinates are fixed in the orbital frame.

(ii) The x-axis is chosen so that the point R at which the stream encounters the magnetosphere is on the x-axis, i.e. has position vector $\mathbf{r} = (r, 0, 0)$ where $r > 1$.

(iii) From (i) the coordinate system rotates at the orbital angular velocity; time zero is

chosen when the "upper" magnetic pole lies in the x-z plane, hence the white dwarf rotates at angular speed $\omega = \omega_{spin} - \omega_{orb}$ in this frame.

(iv) The white dwarf is assumed to have unit radius.

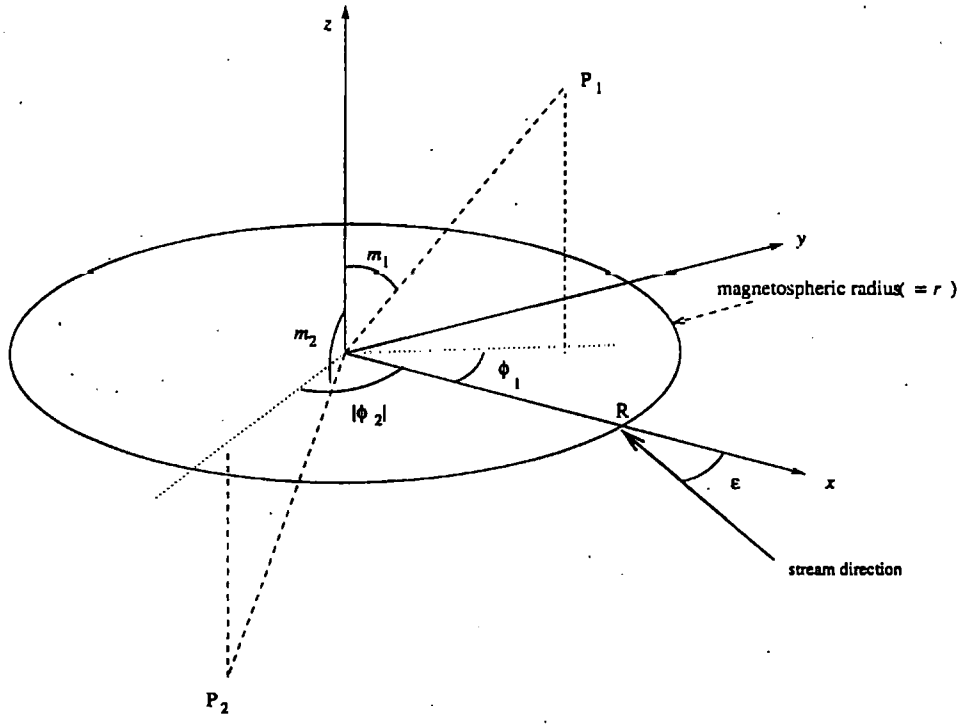

Figure 4.8: Frame used in calculation of ψ; the axes are fixed in the orbital frame, with the stream hitting the magnetosphere at a fixed point (r,0,0), at an angle ϵ to the radius. Note: $\gamma = \phi_1 - \phi_2$.

The calculation takes place within the orbital frame, that is the magnetic poles precess at the beat frequency, and the impact point of the stream at the magnetospheric radius is fixed at r.

The magnetic field B at the point r is calculated at time t, taking account of the precession of the poles. The unit vector $\hat{\mathbf{B}}$ in the field direction is obtained from this, and with the unit vector in the direction of the stream, the incident angle ψ is calculated. This is done for the general case where the stream approaches at an angle ϵ to the radial direction; the

radial inflow case can be obtained by putting $\epsilon = 0$.

4.5.2 The incident angle - general case

The first step is to find the magnetic field at $\mathbf{r}$.

To analyse this situation, we place the "poles" at

$$\mathrm{P}_1 = (1, \phi_1(t), m_1) \tag{4.12}$$

$$\text{and at } \mathrm{P}_2 = (1, \phi_2(t), m_2) \tag{4.13}$$

in spherical polar coordinates,

$$\text{where } \phi_1 = \omega t, \tag{4.14}$$

$$\text{and } \phi_2 = \omega t - \gamma. \tag{4.15}$$

(See figure 4.8).

The symmetric dipole case can be recovered in two ways, either with

$$m_2 = m_1 + 180^\circ \text{ and } \gamma = 0^\circ; \tag{4.16}$$

or, using the standard polar coordinate representation, with

$$m_2 = 180^\circ - m_1 \text{ and } \gamma = 180^\circ. \tag{4.17}$$

So, in the frame as defined, the poles at P_1 and P_2 have the position vectors

$$\mathrm{p}_1 = (\sin m_1 \cos\phi_1, \sin m_1 \sin\phi_1, \cos m_1), \tag{4.18}$$

$$\text{and } \mathrm{p}_2 = (\sin m_2 \cos\phi_2, \sin m_2 \sin\phi_2, \cos m_2). \tag{4.19}$$

We are interested in the direction of the magnetic field at the point R, as the points P_1 and P_2 move around in an anticlockwise direction at the rate ω.

Call the angles between the line OR - or the x-axis - and the lines OP_1, OP_2, respectively ξ_1 and ξ_2 (figure 4.9). Then we have

$$\cos\xi_1 = \mathrm{p}_1.(1,0,0)$$

$$= \sin m_1 \cos\phi_1, \tag{4.20}$$

$$\cos\xi_2 = \sin m_2 \cos\phi_2$$

$$= \sin m_2 \cos(\phi_1 - \gamma). \tag{4.21}$$

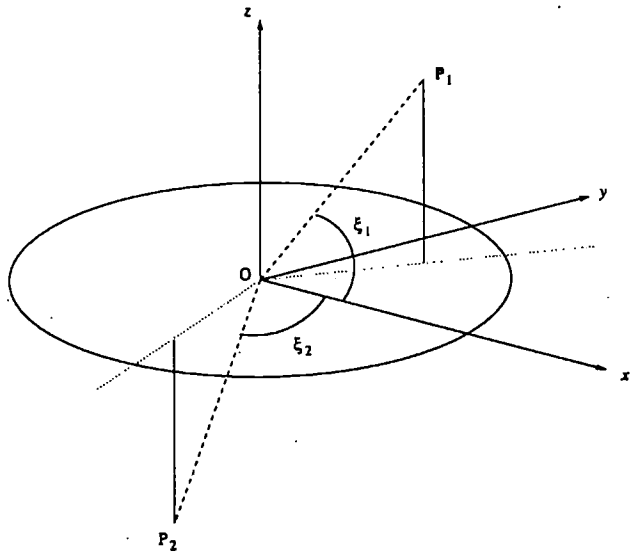

Figure 4.9: The angles between the x-axis (stream direction) and the magnetic pole radius vectors.

Then, by the cosine rule (or vector algebra if preferred), the distances of P_1 and P_2 from R are given by :-

$$\begin{aligned} l_1 &= \sqrt{1 - 2r\cos\xi_1 + r^2} \\ &= \sqrt{1 - 2r\,\sin m_1 \cos\phi_1 + r^2}, \qquad (4.22) \\ l_2 &= \sqrt{1 - 2r\cos\xi_2 + r^2} \\ &= \sqrt{1 - 2r\,\sin m_2 \cos\phi_2 + r^2}. \qquad (4.23) \end{aligned}$$

Note that ξ_1 and ξ_2 are dependent upon time, hence so are l_1 and l_2.

Now define $\mathbf{l}_1$ and $\mathbf{l}_2$ to be the vectors joining P_1 to R etc.

Then

$$\mathbf{l}_1(t) = \mathbf{r} - \mathbf{p}_1(t) \qquad (4.24)$$

$$\mathbf{l}_2(t) = \mathbf{r} - \mathbf{p}_2(t), \qquad (4.25)$$

with the time dependence stated explicitly. Hence, using equations (4.14) and (4.15) we have

$$\mathbf{l}_1(t) = \mathbf{r} - (\sin m_1 \cos\omega t, \sin m_1 \sin\omega t, \cos m_1) \qquad (4.26)$$

$$\mathbf{l}_2(t) = \mathbf{r} - (\sin m_2 \cos(\omega t - \gamma), \sin m_2 \sin(\omega t - \gamma), \cos m_2). \qquad (4.27)$$

To get the magnetic field direction at R, we calculate the vector sum of the magnetic fields caused by imagined monopoles (of equal and opposite polarity) at P_1 and P_2, i.e. work out the dipole field here from first principles. This is more convenient for our parametrisation, although less elegant, than taking the dipole field directly and finding the appropriate rotation transforms. Hence, the magnetic field vector at R has a component due to P_1 and a component due to P_2, given by

$$\mathbf{B}_1(t) = \frac{\mathbf{l}_1(t)}{l_1(t)^3}, \qquad (4.28)$$

$$\mathbf{B}_2(t) = -\frac{\mathbf{l}_2(t)}{l_2(t)^3} \qquad (4.29)$$

(where, since only the direction is of interest, a constant of proportionality has been left out). The negative sign in the expression for $\mathbf{B}_2$ is based on the assumption of opposite polarity. This assumes poles of equal strength of course.

So the field is

$$\mathbf{B}(t) = \mathbf{B}_1(t) + \mathbf{B}_2(t)$$

$$= \frac{\mathbf{r}-\mathbf{p}_1(t)}{l_1(t)^3} - \frac{\mathbf{r}-\mathbf{p}_2(t)}{l_2(t)^3}$$

$$= r(1,0,0)\left(\frac{1}{l_1(t)^3} - \frac{1}{l_2(t)^3}\right) - \frac{\mathbf{p}_1(t)}{l_1(t)^3} + \frac{\mathbf{p}_2(t)}{l_2(t)^3}. \tag{4.30}$$

So the components are

$$B_x(t) = \frac{r}{l_1(t)^3} - \frac{r}{l_2(t)^3} - \frac{\sin m_1 \cos \omega t}{l_1(t)^3} + \frac{\sin m_2 \cos(\omega t - \gamma)}{l_2(t)^3} \tag{4.31}$$

$$B_y(t) = -\frac{\sin m_1 \sin \omega t}{l_1(t)^3} + \frac{\sin m_2 \sin(\omega t - \gamma)}{l_2(t)^3} \tag{4.32}$$

$$B_z(t) = -\frac{\cos m_1}{l_1(t)^3} + \frac{\cos m_2}{l_2(t)^3} \tag{4.33}$$

The magnitude of $\mathbf{B}$ is

$$B_{norm} = \sqrt{{B_x}^2 + {B_y}^2 + {B_z}^2}. \tag{4.34}$$

The unit vector in the direction of $\mathbf{B}$ is therefore $\hat{\mathbf{B}} = \mathbf{B}/B_{norm}$.

Finally, in order to calculate ψ, we note that the unit vector in the direction of the stream (see figure 4.8) is:-

$$\hat{\mathbf{s}} = (-\cos\epsilon, \sin\epsilon, 0) \tag{4.35}$$

where ϵ is arbitrary.

Therefore, the angle that $\mathbf{B}$ makes with the stream (see figure 4.10) is ψ, where :

$$\cos\psi = \hat{\mathbf{s}}.\hat{\mathbf{B}} \tag{4.36}$$

$$\text{so } \cos\psi = -\frac{B_x \cos\epsilon}{B_{norm}} + \frac{B_y \sin\epsilon}{B_{norm}}. \tag{4.37}$$

So equation 4.37 gives the final expression for ψ, the angle between the stream and field lines. As figure 4.10 shows, ψ has a range of values straddling 90°, hence $\cos\psi$ has a range of positive and negative values.

Taking $m_2 = 180° - m_1$ and $\gamma = 180°$ gives the symmetric dipole, and $\epsilon = 0$ gives a radial stream. If we choose both the above, the results agree with the symmetric dipole and radial stream case.

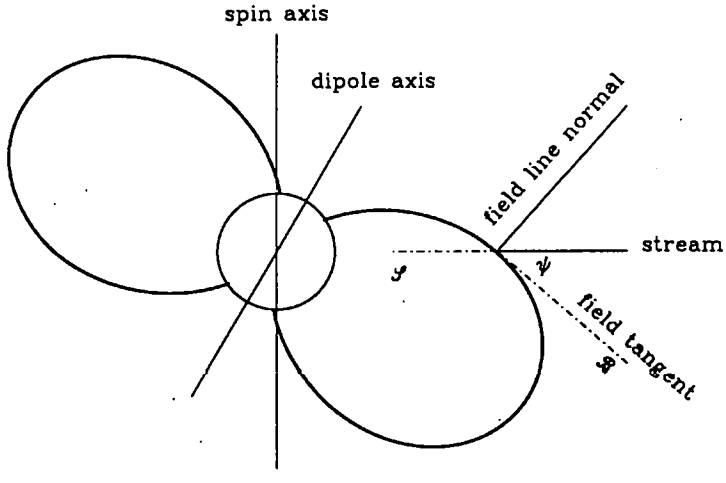

Figure 4.10: The angle ψ of the stream to the magnetic field. $\mathcal{B}$ is the unit vector in the direction of the field line; $\mathcal{S}$ is that for the stream direction.

4.6 Cell luminosity

The original program did not calculate the cell luminosity, and simply regarded them all as some standard value. However, due to the difference in disc and stream-fed accretion, in both accretion rate and footprint area, different cells cannot be assumed to have the same brightness. Hence the physics of the situation requires this calculation; also the density of the absorber from disc and stream-fed components can differ, so this too is calculated.

The white dwarf mass is chosen to be the independent parameter; its radius is determined by Neuenberg's formula (equation 4.7). The mass and radius are used to calculate the energy release and therefore the luminosity of the accreting cells.

The luminosity of the accreting cells depends also on the accretion rate ($\dot{M}$), which is a new parameter to the program. (Actually the parameter is M17DOT, i.e. the accretion rate in units of 10^{17} g s^{-1}.) This was left out by Norton (1993) as the luminosity only varies linearly with $\dot{M}$ and was therefore lost as the end results are normalised anyway. However, the absorption effects also depend on this parameter, and these vary exponentially, hence its inclusion.

To calculate the luminosity and the density of the pre-shock accretion stream we use the relations

$$L_{acc} = 1.3 \times 10^{34} \dot{M}_{17} M_* R_9^{-1} \,\mathrm{erg\,s^{-1}}, \tag{4.38}$$

$$\rho = 1.5 \times 10^{-9} \dot{M}_{17} f_{-2}^{-1} M_*^{-1/2} R_9^{-3/2} \,\mathrm{g\,cm^{-3}}, \tag{4.39}$$

where M_* is the white dwarf mass in units of solar mass. The first is adapted from Frank, King and Raine (1992), (equation 1.4a), and the second from King & Shaviv (1984). (In the program the factor 10^{34} in the luminosity formula is replaced by 10^3, giving a relative luminosity of order unity for reasonable values. As pointed out above, this isn't critical; the density cannot be so treated, however.)

The luminosity per accreting cell is then calculated simply by dividing the number of cells (from the accretion arc geometry) into the luminosity. This calculation may be done twice, once for the disc-fed accretion areas, at the start of the run, and for stream-fed areas at each timestep, since the latter can be expected to vary as the beat phase. These are added to provide a luminosity for each visible cell.

4.7 Optical depth calculation - horizontal and vertical components

Here a preliminary look at the calculation of optical depth in various directions is taken, particularly in regard to the non-constant horizontal distance from a cell to the edge of the accretion curtain (now arc-shaped). Previously this distance was taken as an average from the centre cell, and assumed constant.

In the rest of this section we calculate more realistic values for τ_h and τ_v in the case of arc-shaped accretion and consider how they may be combined to estimate the total optical depth along a line of sight. Then in section 4.8 we carry out an explicit calculation of the optical depth at arbitrary elevation angles. In section 4.10 we calculate the distance of an arbitrary cell from the edge of the accretion curtain in any direction (corresponding to the line of sight), and use this and the elevation angle to obtain the optical depth.

The original calculation of the optical depth (τ), in Norton (1993), used equation (3) in King & Shaviv (1984) (hereafter called KS84), following Fabian et al (1976) (hereafter referred to as FPR76). These were based on the assumption of cylindrical inflow, hence the optical depth in any particular direction was calculated using two parameters, τ_h and τ_v, the horizontal and vertical optical depths respectively. A sine-squared weighting was used, that is, if the elevation angle to the line of sight was μ, the optical depth was given by

$$\tau_1(\mu) = \tau_h \cos^2 \mu + \tau_v \sin^2 \mu \tag{4.40}$$

(see figure 4.11).

Wynn & King (1992) use a slightly different sinusoidal weighting:

$$\tau_2(\mu) = \tau_h |\cos \mu| + \tau_v (1 - |\cos \mu|). \tag{4.41}$$

There are two problems with these: (1) for an arc-shaped accretion column it is doubtful that a single value of τ_h is sufficient; (2) the sine or sine-squared weightings do not give an accurate dependence on μ.

The authors (KS84 and FPR76) do a preliminary calculation of τ_v and τ_h assuming the only cause is electron-scattering (energy independent), then modify to get the energy dependent photo-electric absorption term:

$$\tau_{pe} \simeq 600 \tau_{es} E^{-3}. \tag{4.42}$$

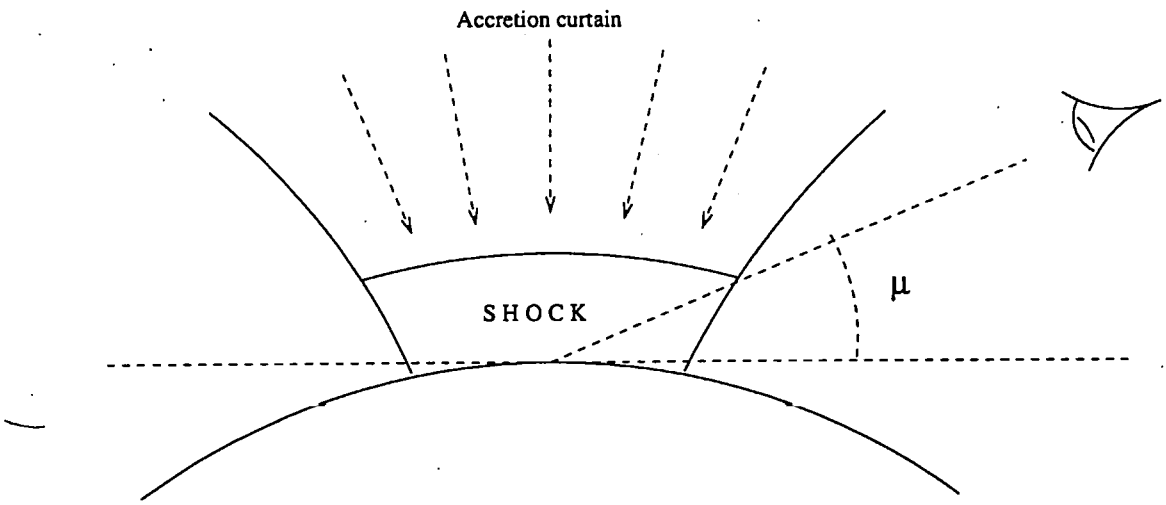

Figure 4.11: The accretion column - cylindrical case.

The first task here is to do a recalculation of τ_h in different directions, obtaining a maximum and minimum value (averaged out over the accretion region), to determine whether the resulting (different) optical depths do require the explicit calculation in section 4.10. The assumed area of the emission region is also modified, as the density of the obscuring material affects the calculation, hence τ_v will be affected as well as τ_h.

Assumptions :-

(1) The formula for density of the accreting material is taken from FPR76, which depends on $\dot{M}$ and f. This is then modified: f is replaced by A, the fractional area of the emission region; f is the polecap (fractional) area.

(2) The emission region is arc-shaped, so the (average) minimum and maximum distances through the arc can be estimated. The arc subtends an angle α at the magnetic pole, where

$$\alpha = f''/2\pi. \tag{4.43}$$

For disc-fed accretion, modelled by a long thin arc, the minimum distance is expected to be in the direction to the outer or inner edge of the arc, and the maximum distance along the arc, as in figure 4.12.

However, in stream-fed accretion the angle α may be much smaller, and the maximum and minimum distances may be reversed, depending on the value of $a_2 - a_1$. Hence the distances are labelled d_{rad} and d_{trans}, for radial and transverse.

(3) Since the photoelectric contribution is proportional to the electron scattering contribution at any particular energy, the latter is calculated first, and the results modified later by equation (4.42) to give the total (energy-dependent) optical depth.

Also, τ_v is recalculated, using A in place of f. Hence three limits for τ are obtained, called here τ_{rad}, τ_{trans}, and τ_v. These are expressed in terms of τ_h as obtained by FPR76, to give a comparison.

4.7.1 The horizontal optical depth according to FPR76

FPR76 give the above-shock density of accreting material as (adapting their notation) :

$$\rho_1 = 1.5 \times 10^{-9} \dot{M}_{17} f_{-2}^{-1} M_*^{-1/2} R_9^{-3/2} \,\mathrm{g\,cm^{-3}}. \tag{4.44}$$

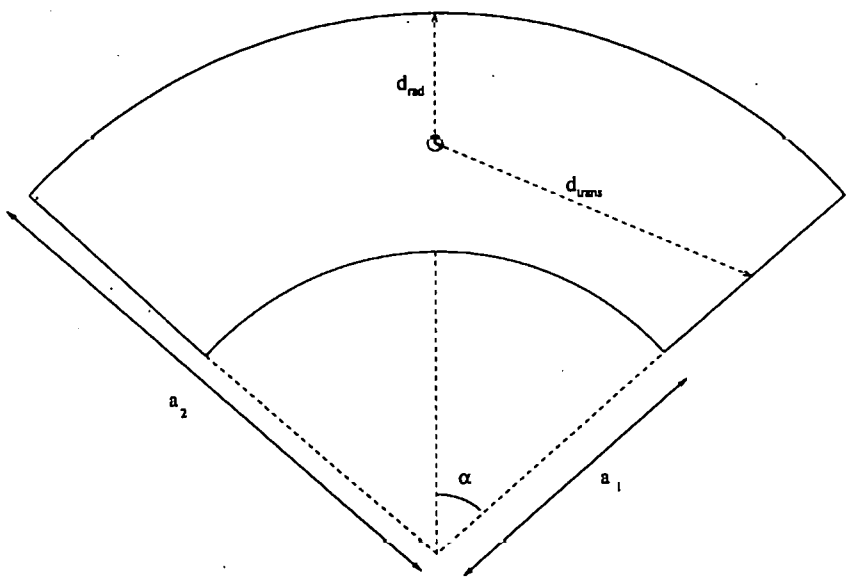

Figure 4.12: Directions giving limiting (horizontal) distances through the accretion arc from the centre of the emission region.

They also give an expression for the optical depth due to electron scattering, which can be generalised to

$$\tau_{es} = 0.2(1+X)\int_a^b \rho(x)dx, \tag{4.45}$$

where X is the hydrogen mass fraction, which they take to be 0.7. The expression $0.2(1+X) = \sigma_T n_e/\rho$ has units cm^2 g^{-1}.

Putting the figures in, and assuming the density is constant, the horizontal optical depth is

$$\tau_{es}(d) = 0.51 \times 10^{-9} \dot{M}_{17} f_{-2}^{-1} M_*^{-1/2} R_9^{-3/2} d \tag{4.46}$$

where d is the average horizontal distance (i.e. the radius of the accretion *cylinder*). They then use the approximation $d \approx \sqrt{2} f R_*$. (They have introduced an error here: it should read $2R_*\sqrt{f}$, which is equivalent to $2 \times 10^8 R_9 f_{-2}^{1/2}$. The following analysis uses the corrected term.) Using this, the formula simplifies to

$$\begin{aligned} \tau_{es}(d) &= 0.51 \times 10^{-9} \dot{M}_{17} f_{-2}^{-1} M_*^{-1/2} R_9^{-3/2} \times 2 \times 10^8 R_9 f_{-2}^{1/2} \\ &= 0.1 \dot{M}_{17} f_{-2}^{-1/2} M_*^{-1/2} R_9^{-1/2} \end{aligned} \tag{4.47}$$

Let us refer to this as T_H, the horizontal optical depth due to electron scattering only, as calculated by FPR76.

4.7.2 Arc-shaped accretion regions

We now extend the calculation to consider arc-shaped accretion regions.

From the definitions of f, f', and f'',

$$f = 0.5(1 - \cos(a_2/R_*)), \tag{4.48}$$

$$f' = (a_2 - a_1)/a_2, \tag{4.49}$$

$$f'' = 2\alpha/2\pi = \alpha/\pi, \tag{4.50}$$

(see figure 4.12), where a_2, a_1 are the radii of the outer and inner circles respectively defining the accreting annulus, R_* is the white dwarf radius, and α is the semi-angle of the azimuthal range of the arc. Hence f is now the fractional area of the circular *accretion envelope* round the polecap, rather than the area of the arc-shaped emission region. The latter is given the

symbol A. Let $\sigma = f'(2-f')f''$, i.e. the fractional area of the footprint compared to that of the circle. Then the total fractional accreting area is

$$A = \sigma f. \tag{4.51}$$

So equation (4.44) converts to

$$\rho_1 = 1.5 \times 10^{-9} \dot{M}_{17} A_{-2}^{-1} M_*^{-1/2} R_9^{-3/2}, \tag{4.52}$$

$$\text{where } A_{-2} = \sigma f_{-2}. \tag{4.53}$$

Thus our value for ρ_1 differs from FPR's by a factor σ^{-1}, for the same value of f.

For horizontal optical depths (τ_{es}), assume ρ is constant. Then, using (4.46), with d now signifying the distance of an emitting cell from the edge of the accretion curtain, we have

$$\tau_{es}(d) = 0.51 \times 10^{-9} \dot{M}_{17} A_{-2}^{-1} M_*^{-1/2} R_9^{-3/2} d. \tag{4.54}$$

4.7.3 Limits on horizontal distances through the arc

From our point of view, we need d_{trans} and d_{rad}, as shown in figure 4.12, to obtain limits on τ_{es} (assumed here from a central position in the accretion arc).

Then,

$$d_{rad} = (a_2 - a_1)/2, \tag{4.55}$$

$$\frac{d_{trans}/2}{(a_1+a_2)/2} \approx \sin(\frac{\alpha}{2}), \tag{4.56}$$

$$\text{i.e. } d_{trans} \approx (a_1+a_2)\sin(\alpha/2). \tag{4.57}$$

Using (4.48), a_2 is given exactly by

$$\cos(\frac{a_2}{R_*}) = 1 - 2f, \tag{4.58}$$

or approximately (for small f) by

$$a_2 \approx 0.2 R_* f_{-2}^{1/2}. \tag{4.59}$$

(This is accurate to within 2% for $f < 0.1$, that is for $\beta_2 \lesssim 37°$. Note that in radians, $\beta_q = a_2/R_*$.)

From (4.49),

$$a_1 = a_2(1-f'), \tag{4.60}$$

$$\text{hence } d_{rad} \approx 0.1 R_* f' f_{-2}^{1/2} \tag{4.61}$$

$$\text{and, since } \alpha = \pi f'', \tag{4.62}$$

$$d_{trans} \approx 0.2 R_* f_{-2}^{1/2}(2-f')\sin(\pi f''/2). \tag{4.63}$$

4.7.4 Limits on horizontal optical depths through the arc

We now define τ_{rad} to be the value of τ_h in the radial direction, towards or away from the magnetic pole; and τ_{trans} to be the value of τ_h perpendicular to τ_{rad}. (Both are averaged out over the accreting area, and consider electron scattering only).

Putting the values for d_{trans} and d_{rad} into equation (4.54), and replacing A^{-1} by $(f\sigma)^{-1}$,

$$\tau_{rad} \approx (0.51\times 10^{-9}\dot{M}_{17} f_{-2}^{-1} M_*^{-1/2} R_9^{-3/2}\sigma^{-1}) \times 0.1 R_* f' f_{-2}^{1/2} \tag{4.64}$$

$$\approx 0.05 \times \sigma^{-1} f' \,(\dot{M}_{17} f_{-2}^{-1/2} M_*^{-1/2} R_9^{-1/2}),$$

$$\text{and } \tau_{trans} \approx 0.1(2-f')\sin(\frac{\pi f''}{2})\sigma^{-1}\,(\dot{M}_{17} f_{-2}^{-1/2} M_*^{-1/2} R_9^{-1/2}). \tag{4.65}$$

Alternatively,

$$\tau_{rad} \approx 0.5\,\sigma^{-1} f' \times T_H, \tag{4.66}$$

$$\tau_{trans} \approx 1.0\,\sigma^{-1}(2-f')\sin(\pi f''/2)\times T_H$$

$$= (f'\ f'')^{-1}\ \sin(\pi f''/2)\times T_H. \tag{4.67}$$

4.7.5 Vertical optical depth

Finally, we calculate the vertical optical depth (τ_v) due to electron scattering. By equations (4.45) and (4.52), and assuming dipole geometry,

$$\tau_v = 0.2(1+X)\int_{R_*}^{\infty}\rho(r)dr \tag{4.68}$$

$$\text{where } \rho(r) = \rho_1(\frac{r}{R_*})^{-5/2}. \tag{4.69}$$

$$\text{Hence } \tau_v = 0.34\,\rho_1\int_{R_*}^{\infty}(\frac{r}{R_*})^{-5/2}dr$$

$$= 0.51\times 10^{-9}\dot{M}_{17}A_{-2}^{-1}M_*^{-1/2}R_9^{-3/2}R_*^{5/2}\int_{R_*}^{\infty} r^{-5/2}dr$$

$$= 0.34\,\dot{M}_{17}(\sigma f_{-2})^{-1} M_*^{-1/2} R_9^{-1/2} \quad (4.70)$$

$$= (0.1\dot{M}_{17} f_{-2}^{-1/2} M_*^{-1/2} R_9^{-1/2}) \times 3.4 f_{-2}^{-1/2} \sigma^{-1} \quad (4.71)$$

$$= 3.4 \times (f_{-2}^{-1/2}\sigma^{-1}) \times T_H. \quad (4.72)$$

4.7.6 Comparisons

Comparing with FPR76's analysis, we get the limits :-

$$\tau_{rad} = 0.5\,\sigma^{-1}\, f'\, T_H, \quad (4.73)$$

$$\tau_{trans} = (f'\, f'')^{-1}\, \sin(\pi f''/2)\, T_H, \quad (4.74)$$

$$\tau_v = 3.4\,\sigma^{-1}\, f_{-2}^{-1/2}\, T_H. \quad (4.75)$$

Putting in plausible values for disc-fed accretion, for example $R_{mag}(1) = 10R_*$, $R_{mag}(2) = 7R_*$, $f'' = 0.5$, and setting $m_1 = 10°$, we get $\beta_1 = 18.14°$ and $\beta_2 = 21.85°$, so

$$\begin{aligned} a_1 &= 0.32\,R_* \\ a_2 &= 0.38\,R_* \\ f &= 0.036 \\ \text{(i.e. } f_{-2} &= 3.6\text{)}, \\ f' &= 0.17 \\ \text{and } \sigma &\approx 0.16. \end{aligned}$$

These then give

$$\begin{pmatrix} \tau_{rad} \\ \tau_{trans} \\ \tau_v \end{pmatrix} = \begin{pmatrix} 0.54 \\ 8.32 \\ 11.5 \end{pmatrix} \times T_H. \quad (4.76)$$

If we also assume values $\dot{M}_{17} \approx 1.0$ and $M_* \approx 0.6$, we get $R_9 \approx 0.87$ (Neuenberg), and

$$T_H \approx 0.1 \times (0.6 \times 0.87 \times 3.6)^{-1/2} = 0.073, \quad (4.77)$$

so

$$\begin{pmatrix} \tau_{rad} \\ \tau_{trans} \\ \tau_v \end{pmatrix} = \begin{pmatrix} 0.039 \\ 0.61 \\ 0.84 \end{pmatrix} \quad (4.78)$$

The above value for f'' is an assumption for disc-fed accretion. For stream-fed accretion, f'' is expected to be less. So, for example, putting $f'' = 0.1$ and keeping the other values the same, $\sigma \approx 0.03$. It turns out that $d_{rad} = 0.0323$ and $d_{trans} = 0.109$. The optical depths are

$$\begin{pmatrix} \tau_{rad} \\ \tau_{trans} \\ \tau_v \end{pmatrix} \approx \begin{pmatrix} 0.2 \\ 0.67 \\ 4.36 \end{pmatrix} . \tag{4.79}$$

FPR76 only gave two values, with $T_V \approx 10 \times T_H$. In both the above cases, the different values for horizontal τ, spanning or being of close order to unity, suggest that τ_h cannot be treated as a constant.

4.8 The variation of optical depth with elevation angle

4.8.1 Theory - calculation by integration:

Previously the calculation of absorption/scattering at various angles assumes that the stream is cylindrical (FPR76 and KS84). Frank, King & Raine (1992) cover this, and mention the possibility of the inflow being a hollow cylinder.

At this point we present a re-analysis of the calculation of τ at various elevation angles ($\tau(\mu)$), as this is important in the program. This will be compared later to results by numerical integration; the theoretical formula will be used in the computer model, however. This will also be compared with the sinusoidal weighting mentioned in the previous section. Firstly a review of the calculations is given, and a recalculation of optical depth at different μ for the cylindrical case is carried out. These will later be compared with the different types of weighting assumed by Norton (1993) and Wynn & King (1992).

This is the electron scattering component; to get the total optical depth, including photo-electric absorption, King & Shaviv use equation (4.42) quoted earlier,

$$\tau_{pe} \simeq 600 \tau_{es} E^{-3},$$

giving the dependence on photon energy. This is an approximation; for a better correlation absorption edges should be taken into account.

We next discuss optical depths as a function of elevation.

4.8.2 Review of previous calculations

King & Shaviv (1984) give values for H_S (the shock height), d, the distance from the centre of the emission region to the edge of the accretion curtain, and the pre-shock density ρ_1 which are in agreement (to order of magnitude) with FPR76. As FPR76, they assume a dipole geometry, so that the density above the shock depends on r (the distance from the white dwarf centre) by the relation $\rho(r) = \rho_1(r/R_*)^{-5/2}$.

According to King & Shaviv then,

$$\rho_1 = 1.5 \times 10^{-9} \dot{M}_{17} f_{-2}^{-1} (M/M_\odot)^{-1/2} R_9^{-3/2} \quad (4.80)$$

$$H_S \lesssim 9.1 \times 10^{7} \dot{M}_{17}^{-1} f_{-2} (M/M_\odot)^{3/2} R_9^{1/2}. \quad (4.81)$$

$$d = 2 \times 10^{8} f_{-2}^{1/2} R_9. \quad (4.82)$$

$$\tau_v = 0.3 \dot{M}_{17} f_{-2}^{-1} (M/M_\odot)^{-1/2} R_9^{-1/2}. \quad (4.83)$$

$$\tau_h = 0.1 \dot{M}_{17} f_{-2}^{-1/2} (M/M_\odot)^{-1/2} R_9^{-1/2}. \quad (4.84)$$

Comparing King & Shaviv's calculations to FPR76's,

$$\begin{aligned} H_S(KS) &\lesssim 0.3 \times H_S(FPR), \\ \tau_v(KS) &\approx 0.3 \times \tau_v(FPR) \\ \tau_h(KS) &\approx \tau_h(FPR). \end{aligned} \quad (4.85)$$

(H_S is obtained in order to argue that the optical depth from the surface to the shock is small enough to be ignored.) The value for τ_v used in the next calculation is that from equation 4.70, essentially King & Shaviv's but with the adjustment σ on the accretion area.

4.8.3 Recalculation assuming dipolar inflow

The optical depth $\tau_3(\mu)$ for an arbitrary angle μ, is calculated by integrating along the line of sight from the shock upwards, and assumes a dipole stream, following the field lines at the surface. It assumes the angles of the accretion curtain walls to the surface (ζ_q) are constant (as in Figure 4.13). This is valid for $\mu << \zeta_2$ and $\mu >> \zeta_1$. In other cases, as μ approaches ζ_q, much of the line of sight passes through regions high above the surface, which have progressively less effect, assuming the reduction in density. (This is considered later, comparing the results from this approach to a numerical integration.)

Other assumptions are as the previous model.

The values of τ_v and τ_h (the latter now for $\zeta_2 \leq \mu \leq \zeta_1$ rather than $\mu = 90°$) are then obtained from the above, and compared with previous values.

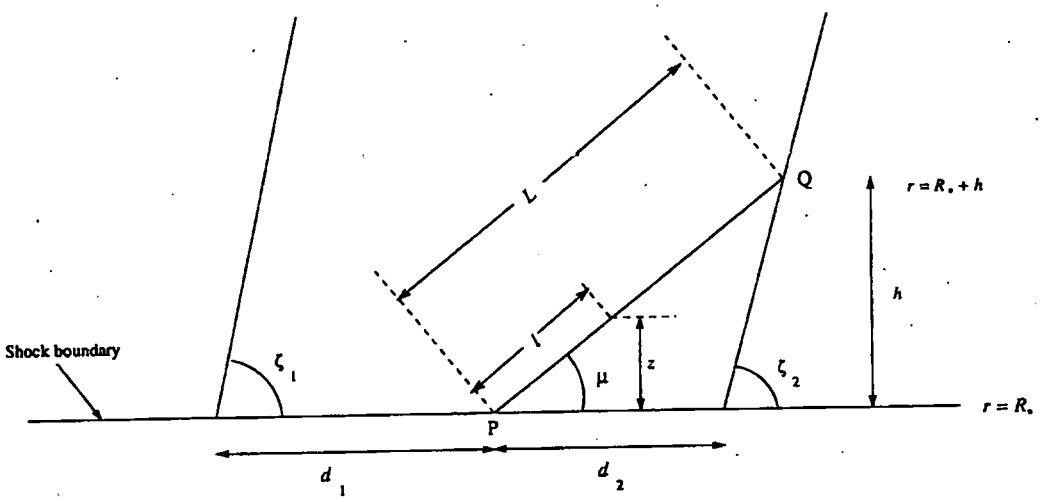

Figure 4.13: The accretion stream at the white dwarf surface (assuming dipole geometry). The shock boundary is approximated to a straight line, though it will curve to a few degrees of arc over the distance given; the radius at the shock boundary is approximated to R_*.

From figure 4.13, the angle the field lines make with the horizontal at the white dwarf surface at an angle β from the pole is ζ where, using dipole geometry,

$$\sin\zeta = \frac{2\cos\beta}{\sqrt{1+3\cos^2\beta}}. \tag{4.86}$$

Now, to obtain the optical depth, we integrate along the line of sight from P to Q (see figure 4.13).

As can be seen, there are three ranges for μ, (a) $\mu \leq \zeta_2$, (b) $\zeta_2 < \mu \leq \zeta_1$ and (c) $\mu > \zeta_1$.

Let the cell in question be at a distance d_1 from the inner edge, and d_2 from the outer edge

(as in figure 4.13). Then $d_1 + d_2 = a_2 - a_1$, the width of the emission region.

(a) For $\mu \leq \zeta_2$, integrate along the line of sight to get τ_3:

$$\tau_3(\mu) = 0.2(1+X)\int_{l=0}^{l=L} \rho(r)dl. \tag{4.87}$$

Here, X is the hydrogen mass fraction, taken to be 0.7 (as in FPR76), and r is the distance from the white dwarf centre. Putting $r = R_* + z$ as the appropriate independent variable, $l\sin\mu = (r - R_*)$, so $dl = dr/\sin\mu$, and the integral becomes

$$\begin{aligned}
\tau_3(\mu) &= \frac{0.2 \times 1.7 \times \rho_1}{\sin\mu}\int_{r=R_*}^{r=R_*+h} (r/R_*)^{-5/2}dr \\
&= \left(-\frac{2}{3}\right)\frac{0.2 \times 1.7 \times \rho_1 R_*^{5/2}}{\sin\mu}\left[r^{-3/2}\right]_{R_*}^{R_*+h} \\
&= \frac{0.23 \times \rho_1 \times R_*^{5/2}}{\sin\mu}(R_*^{-3/2} - (R_* + h)^{-3/2}) \\
&= \frac{\tau_v}{\sin\mu}\left[1 - \left(\frac{R_* + h}{R_*}\right)^{-3/2}\right].
\end{aligned} \tag{4.88}$$

This is using equation 4.52 to get ρ_1.

To get the upper limit requires h, and from the geometry

$$h = (d_2 + c)\tan\mu; \tag{4.89}$$

$$\text{also } h = c\tan\zeta_2. \tag{4.90}$$

$$\text{From these } h = d_2(\cot\mu - \cot\zeta_2)^{-1}, \tag{4.91}$$

$$\text{so } \tau_3(\mu) = \frac{\tau_v}{\sin\mu}\left\{1 - \left[1 + \frac{d_2}{R_*}(\cot\mu - \cot\zeta_2)^{-1}\right]^{-3/2}\right\}. \tag{4.92}$$

(b) In this region, $\zeta_2 < \mu \leq \zeta_1$, the integration is effectively through the column, so the upper limit is ∞; the result is therefore the same as FPR76's for τ_v.

(c) In the region $\mu > \zeta_1$, the integration is similar to that in (a), with $\mu \to \pi - \mu$ and $h = d_1(\cot\zeta_1 - \cot\mu)^{-1}$, reflecting the different geometry. This then gives

$$\tau_3(\mu) = \frac{\tau_v}{\sin\mu}\left\{1 - \left[1 + \frac{d_1}{R_*}(\cot\zeta_1 - \cot\mu)^{-1}\right]^{-3/2}\right\}. \tag{4.93}$$

A slightly easier integration modelling the inflow as a vertical cylinder results in the formula

$$\tau_4(\mu) = \frac{\tau_v}{\sin\mu}[1 - (1 + \frac{d}{R_*}\tan\mu)^{-3/2}]. \tag{4.94}$$

Summarising,

$$\text{(Norton, 1993)} \quad \tau_1(\mu) = \tau_h \cos^2\mu + \tau_v \sin^2\mu \tag{4.95}$$

$$\text{(Wynn \& King, 1992)} \quad \tau_2(\mu) = \tau_h \cos\mu + \tau_v(1-\cos\mu) \tag{4.96}$$

$$\tau_3(\mu) = \begin{cases} (\tau_v/\sin\mu)\left[1-(1+W_2 d_2/R_*)^{-3/2}\right] & \text{if } \mu \le \zeta_2, \\ \tau_v & \text{if } \zeta_2 \le \mu \le \zeta_1, \\ (\tau_v/\sin\mu)\left[1-(1+W_1 d_1/R_*)^{-3/2}\right] & \text{if } \mu \ge \zeta_1. \end{cases} \tag{4.97}$$

In the above,

$$W_1 = (\cot\zeta_1 - \cot\mu)^{-1},$$
$$W_2 = (\cot\mu - \cot\zeta_2)^{-1}.$$

(When $\mu = \pi/2$, $\cot\mu = 0$, so $W_1 = \tan\zeta_1$.)

4.8.4 Check by numerical integration:

To check the above, a short program was written to perform a numerical integration of optical depth through the absorber for various values of d_1 and d_2, with μ ranging from 0° to 180°. This was repeated for different values of $R_{mag}(1)$ and $R_{mag}(2)$, and the values of $\tau(\mu)$ obtained compared with those using the formulae above. The results from selected values of $R_{mag}(q)$ are shown in figure 4.14, along with the other methods of calculating τ.

It can be seen that the formula for τ_3, while not perfect, gives the best approximation. The diffence between the values of μ for peak τ using τ_3 and numerical integration probably lies in the fact that the latter method takes into account recrossing the (curved) accretion curtain later.

Since it is not feasible to use the numerical integration in the model (as the slight extra accuracy would not be worth the increase in the program run time), the formula for τ_3 is used.

In conclusion, the difference in the optical depths as calculated here, particularly the slow increase for smaller μ, suggests the integration method needs to be used rather than the sin/cosine weighting.

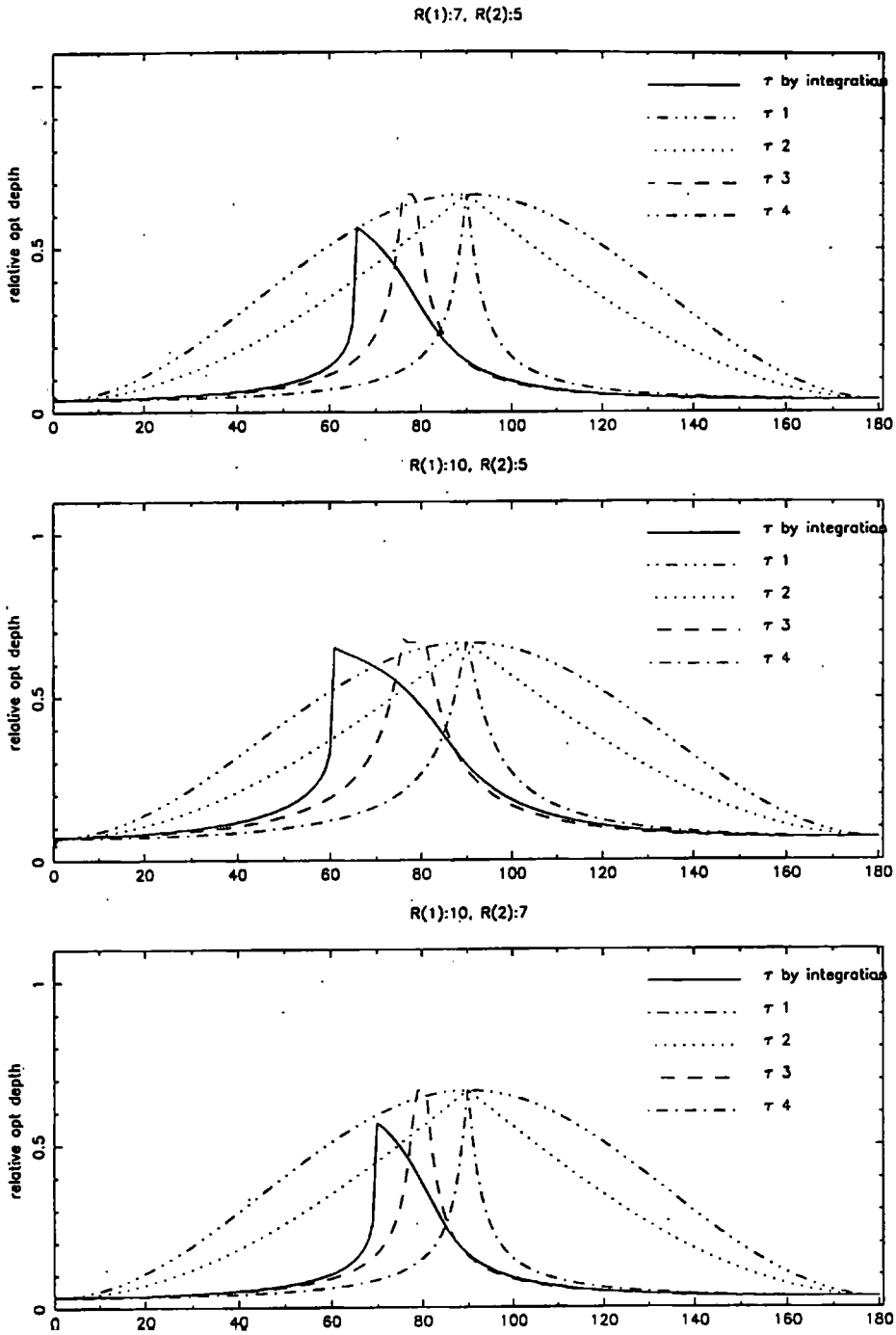

Figure 4.14: Plots of $\tau(\mu)$ for $m = 10°$ using numerical integration (solid line) and also τ_1 to τ_4.

4.9 Obtaining λ and μ

The line of sight angle (λ) and the elevation angle (μ) depend on the spin phase, and need to be calculated; this is done as follows: μ is simple enough, once we have Z, the z-coordinate of the cell in the line of sight frame (from section 4.1.2). As can be seen in figure 4.15, $\mu = \arcsin Z$. No problems arise for $Z < 0$ as then the cell is occulted.

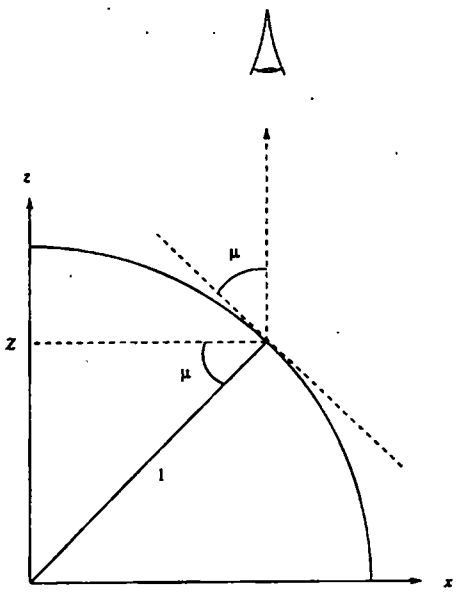

Figure 4.15: Calculation of μ.

To get λ, we need to work out the coordinates of the unit vector e, pointing to the observer, in the *midcell* frame, defined as follows: take the unit vector u, at the middle cell, tangential to the white dwarf surface and pointing along the arc joining the spin pole to this cell. (See Figure 4.16.) Also consider the vector v (not shown), again tangential to the surface, at right angles to u. These can be considered to define a frame, the *midcell* frame. Then λ_0 can be obtained once e is expressed in terms of the midcell frame. To do this, if we know the transform required conceptually to rotate the system bodily so that u, originally in the spin frame, now points along the x-axis (and v along the y-axis), this can then be applied to e as expressed in the line of sight frame.

In the spin frame, the coordinates of the middle cell are defined simply by ($\sin\beta\cos\phi$, $\sin\beta\sin\phi$,$\cos\beta$), where $\beta = m + 0.5(\beta_1 + \beta_2)$. ($\beta = m - 0.5(\beta_1 + \beta_2)$ for the lower pole.)

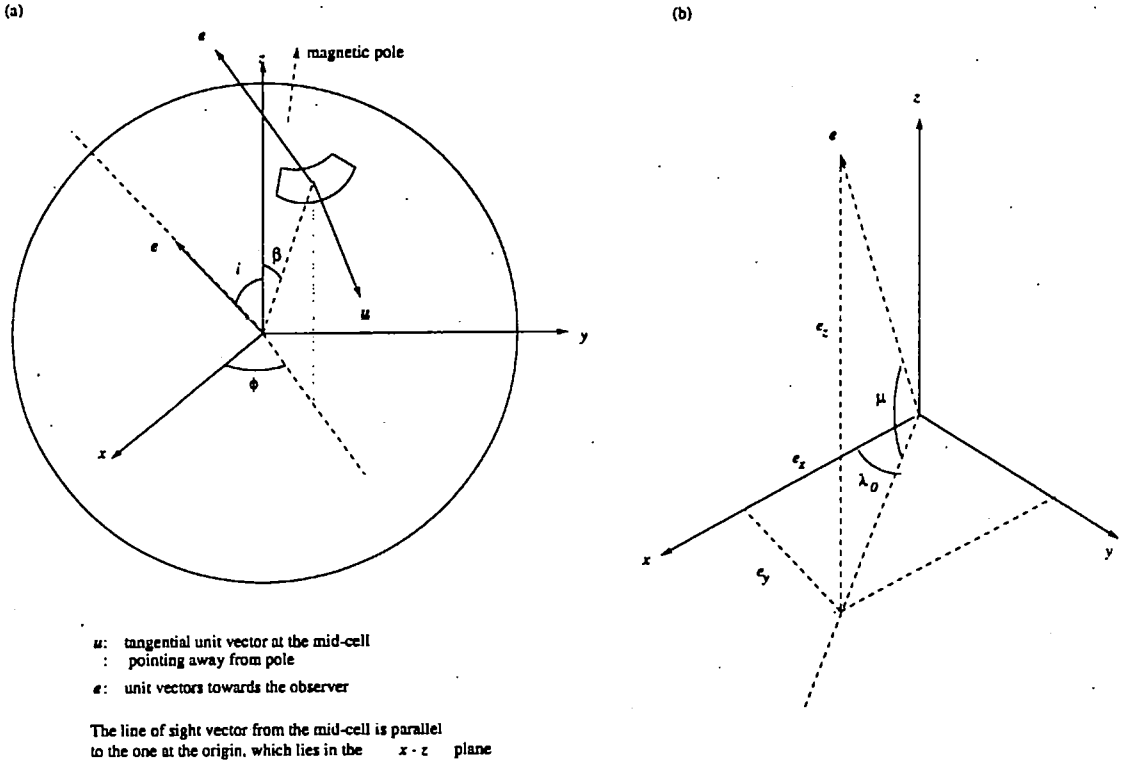

Figure 4.16: The line of sight in (a) the spin frame (b) the midcell frame.

The coordinates of **u** and **v** are not actually relevant, all that is required is to know that to transform them as above, we need first of all to rotate the system through $-\phi$ about the z-axis, then rotate it through β about the y-axis. In the spin frame, **e** has coordinates (e_{xs}, e_{ys}, e_{zs})= ($\sin i$, 0 ,$\cos i$), and it is to this that the above rotations need to be applied.

The rotation matrices are:

$$R_\phi = \begin{pmatrix} \cos\phi & \sin\phi & 0 \\ -\sin\phi & \cos\phi & 0 \\ 0 & 0 & 1 \end{pmatrix}, \tag{4.98}$$

$$R_\beta = \begin{pmatrix} \cos\beta & 0 & -\sin\beta \\ 0 & 0 & 1 \\ \sin\beta & 0 & \cos\beta \end{pmatrix}. \tag{4.99}$$

Applying these transforms to e, we get

$$e_x = \cos\beta\cos\phi\sin i - \sin\beta\cos i, \tag{4.100}$$

$$e_y = -\sin\phi\sin i, \tag{4.101}$$

$$e_z = \sin\beta\cos\phi\sin i + \cos\beta\cos i. \tag{4.102}$$

Now, in the midcell frame, $\mathbf{e} = (\cos\lambda_0\cos\mu, \sin\lambda_0\cos\mu, \sin\mu)$. (Recall that μ here is for the midcell, and may be slightly different for other cells.) Looking at figure 4.16(b), it is evident that care has to be taken in the calculation of λ when either e_x or e_y are non-positive. If both are zero λ_0 is indeterminate, but since from physical principles the line of sight will leave by the β_1 wall of the curtain, it is given the value π. So, taking the range of the arctan function into account, for the upper pole

$$\lambda_0 = \begin{cases} \arctan(e_y/e_x) & \text{if } e_x > 0 \text{ and } e_y > 0 \\ \pi/2 & \text{if } e_x = 0 \text{ and } e_y > 0 \\ \pi & \text{if } e_x = e_y = 0 \\ \pi + \arctan(e_y/e_x) & \text{if } e_x < 0 \\ 3\pi/2 & \text{if } e_x = 0 \text{ and } e_y < 0 \\ 2\pi + \arctan(e_y/e_x) & \text{if } e_x > 0 \text{ and } e_y < 0 \end{cases} \tag{4.103}$$

For the lower pole, λ_0 will differ from the above by π.

(This value for λ_0 actually applies to the midcell of the disc-fed region, which stays at the same position on the surface. The midcell for the stream-fed region "migrates" with the beat phase; this is calculated in the model, and λ_0 adjusted for this by the migration angle.)

4.10 Calculation of horizontal distances through arc-shaped curtain

4.10.1 Introduction

The previous two sections have shown that the electron scattering optical depths in various directions can have orders of magnitude from about 0.1 to 10. Since they also differ significantly in their maximum and minimum horizontal values, in the actual situation the distance through the absorbing curtain in the various horizontal directions needs to be calculated, and that is done here (symbol D_H). We then use the modified formula (4.97) to obtain a better value for $\tau(\mu)$.

D_H depends upon six parameters:-

a_1	radius of inner edge of accretion arc ($= \beta_1 R_*$);
a_2	radius of outer edge of accretion arc ($= \beta_2 R_*$);
α	half-angle subtended by arc;
a	distance of cell from pole;
θ	angle of line from centre to cell;
λ	angle of line of sight to cell.

It is assumed that the region is small enough to be treated as flat. The sector is oriented as in figure 4.17 , all angles being measured anti-clockwise from the x-axis. The quantities a_1, a_2 and α are fixed by the geometry of the accretion region; a and θ are fixed for a particular cell; and λ is dependent on the direction of observation. Also $a_1 < a < a_2$; and $|\theta| < \alpha$.

In most cases, the line of sight from the cell simply exits the region via the outer or inner arcs, or via an edge. In these cases the distance D_H is a single measurement. In a few cases, the line of sight may exit and re-enter the curtain. This is especially possible in the case where the arc extends to about 180° around the pole, as is assumed for the disc-fed component. When this happens, the line of sight re-enters the inner arc, and then exits either the outer arc or an edge. The strategy used in this case is to calculate the total distance to the final exit point, and subtract from it the distance travelled within the inner arc, that is the chord connecting the exit and re-entering points. The first problem is to determine which part of the region the line of sight exits, and whether it re-enters the inner

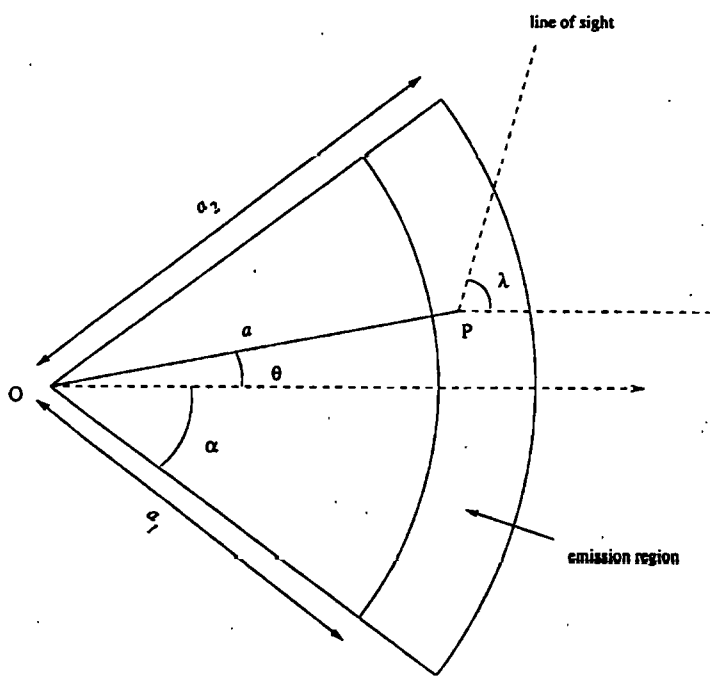

Figure 4.17: Variables involved in the calculation of D_H for a particular cell.

arc at all; the second problem is to calculate the relevent distances.

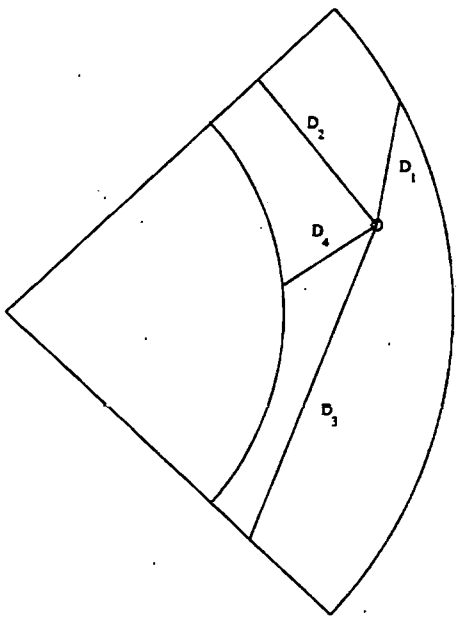

Figure 4.18: Basic distances not involving re-entering the accretion region.

Firstly, to list the possibilities, it can be seen that the distance D_H requires various methods of calculation, depending on the line of sight, which may:

(1)	exit the outer arc directly	$D_H = D_1$
(2)	exit the upper or lower edge	$D_H = D_2$ or D_3
(3)	exit the inner arc only	$D_H = D_4$
(4)	re-enter and exit the outer arc	$D_H = D_1 - \Delta D_4$
(5)	re-enter and exit an edge	$D_H = D_2 - \Delta D_4$ or
		$D_H = D_3 - \Delta D_4$

where the symbols D_n refer to specific distance calculations. Figure 4.18 shows examples of the first three cases, and figure 4.19 is an example of case (4). Note that the distance from a point to an arc may have two values; for the case of the inner edge the lower one is chosen, except that to obtain the length of the chord, in cases (4) and (5), ΔD_4 is the difference

between the two possible values of D_4.

The use of D_H thus obtained will be valid for low μ, but as μ increases, the extra distance due to re-entering the footprint would have less effect in reality (as the line of sight goes through the curtain at a higher point, therefore at a lower density, than it would if the distances were contiguous) as it does in the model.

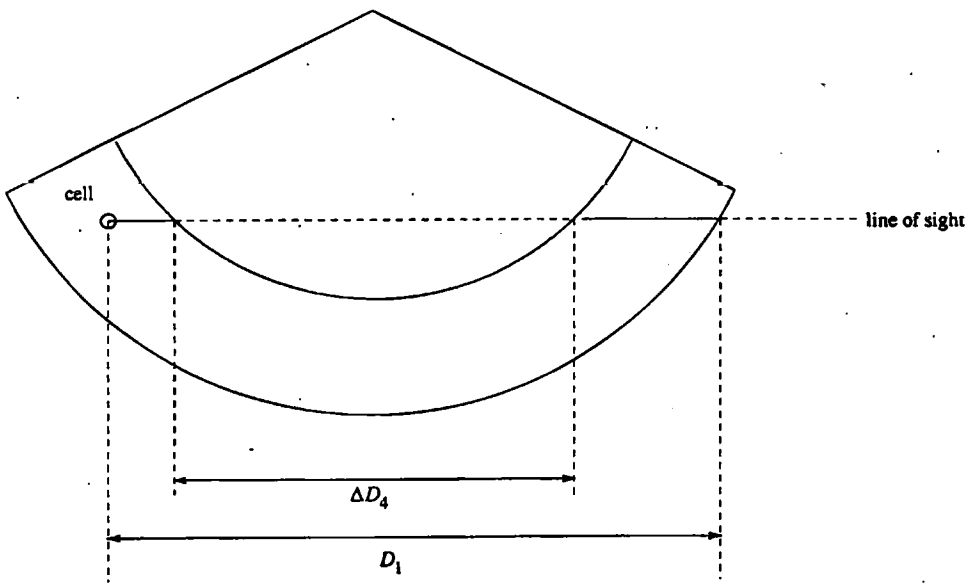

Figure 4.19: Distances required when the line of sight re-enters the accretion curtain.

To determine which of the above are needed, the following steps are taken:

Firstly, the delimiting angles, Λ_{1n}, for the inner arc are required (figure 4.20). These angles are specific to each cell in the accretion region, and are used with λ to discover whether the line of sight does pass/re-enter the inner arc. The labelling convention is that Λ_{10} and Λ_{14} give the grazing lines to the inner arc, Λ_{11} and Λ_{13} give the lines to the "corners" of the sector, and λ_{12} give the angle to the magnetic pole. Note that if the cell is far enough from the inner arc either of the grazing angles may not apply; figure 4.21 shows this, so that in region (i) the line of sight cannot re-enter the accretion arc, in region (ii) it can re-enter towards the lower edge, and so on.

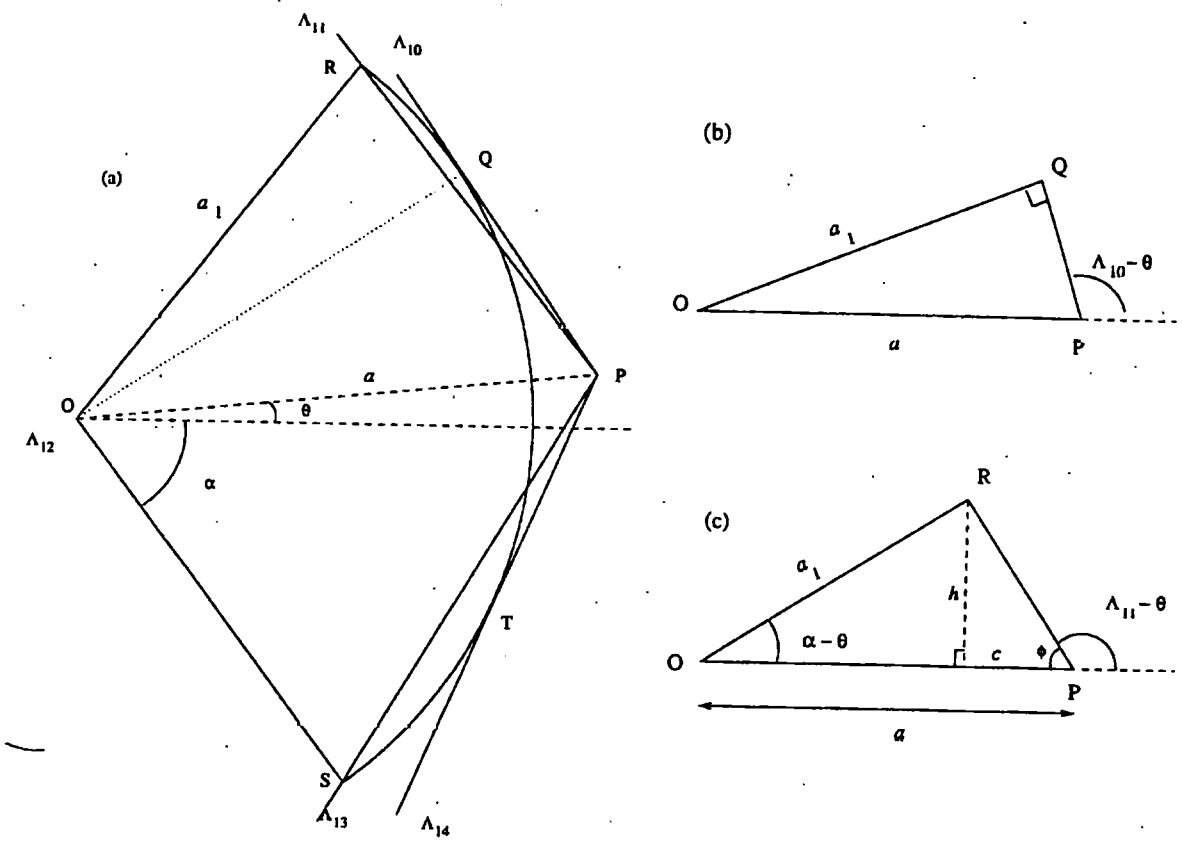

Figure 4.20: Delimiting angles for region (iv). The Λ_{1n} are anticlockwise relative to the horizontal axis, and label the lines in (a) instead of using usual angular labelling, to avoid congestion at P; (b) extracts the triangle for the grazing line of sight; (c) likewise for the one which cuts the upper corner.

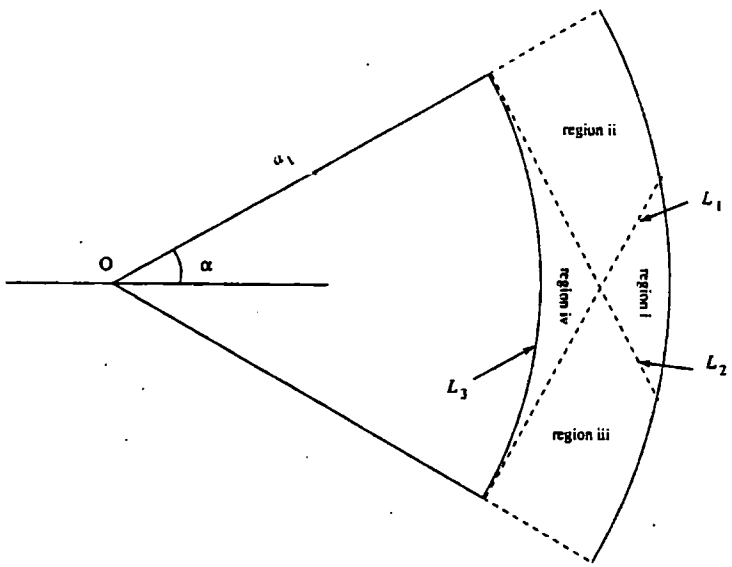

Figure 4.21: Regions of different ranges of Λ_{1n}.

Once the Λ_{1n} are known for the cell, and the line of sight angle λ, it can be determined whether we need to look at the outer arc geometry; thus if $\Lambda_{11} \leq \lambda \leq \Lambda_{13}$ (figure 4.20) the outer arc is irrevelant, as case (3) applies, and $D_H = D_4$. Otherwise the three delimiting angles, Λ_{2n}, for the outer arc, are required (figure 4.22). The labelling convention is similar to the Λ_{1n}, but the tangential angles do not apply. Which of D_1, D_2 or D_3 is required depends on λ and the Λ_{2n}.

Summarising, and assuming modulo 2π, the five cases are determined as follows:

inner arc ranges	outer arc ranges	Calculation	
$\Lambda_{14} \leq \lambda \leq \Lambda_{10}$:	$\Lambda_{23} \leq \lambda \leq \Lambda_{21}$	case (1)	D_1
	$\Lambda_{21} < \lambda \leq \Lambda_{22}$	case (2)	D_2
	$\Lambda_{22} < \lambda < \Lambda_{23}$	case (2)	D_3
$\Lambda_{11} \leq \lambda \leq \Lambda_{13}$:	Λ_{2n} irrevelant	case (3)	D_4
$\Lambda_{10} < \lambda \leq \Lambda_{11}$	$0 \leq \lambda \leq \Lambda_{21}$	case (4)	$D_1 - \Delta D_4$
	$\Lambda_{21} < \lambda \leq \Lambda_{22}$	case (5)	$D_2 - \Delta D_4$
$\Lambda_{13} \leq \lambda < \Lambda_{14}$:	$\Lambda_{23} \leq \lambda \leq 2\pi$	case (4)	$D_1 - \Delta D_4$
	$\Lambda_{22} < \lambda < \Lambda_{23}$	case (5)	$D_2 - \Delta D_4$

Now for the details of the calculations.

4.10.2 Finding the delimiting angles

For the inner sector

There are four distinct regions the cell can be in, in relation to the inner arc, and each region has a different set of Λ_{1n}. These regions are shown in figure 4.21. The simple case is region (i), from which the line of sight can exit the accretion region via the inner arc but cannot re-enter. The most complicated case is where the line of sight can cut the inner arc, and can leave and then re-enter the footprint. For example, from region (iv), any of the five cases may apply.

From region (ii), the line of sight cannot re-enter towards the upper edge, so $\Lambda_{10} = \Lambda_{11}$ for cells in this region. Likewise, from region (iii), $\Lambda_{13} = \Lambda_{14}$ for cells here. From region (i), $\Lambda_{10} = \Lambda_{11}$ and $\Lambda_{13} = \Lambda_{14}$.

Note: Λ_{12} is redundant, but is left in as the calculation was developed in parallel with the Λ_{2n}, where the corresponding angle Λ_{22} is used.

For convenience, define the different possible angular ranges (modulus 2π) to be:

$$\begin{aligned}
\mathcal{A} &: \Lambda_{14} \leq \lambda < \Lambda_{10} \text{ (can apply to all regions)} \\
\mathcal{B} &: \Lambda_{10} \leq \lambda < \Lambda_{11} \text{ (regions iii and iv only)} \\
\mathcal{C} &: \Lambda_{11} \leq \lambda < \Lambda_{13} \text{ (all regions)} \\
\mathcal{D} &: \Lambda_{13} \leq \lambda < \Lambda_{14} \text{ (regions ii and iv only).}
\end{aligned} \tag{4.104}$$

The regions are bounded by two straight lines (L_1 and L_2) and the arc L_3 (figure 4.21). Since L_1 has slope $(1/\tan\alpha)$ and passes through the point $(a_1\cos\alpha, -a_1\sin\alpha)$, and L_2 has slope $(-1/\tan\alpha)$ and passes through the point $(a_1\cos\alpha, a_1\sin\alpha)$, their equations are :-

$$L_1: \quad y = \frac{x}{\tan\alpha} - \frac{a_1}{\sin\alpha} \tag{4.105}$$

$$L_2: \quad y = -\frac{x}{\tan\alpha} + \frac{a_1}{\sin\alpha} \tag{4.106}$$

$$L_3: \quad a_1^2 = x^2 + y^2. \tag{4.107}$$

This assumes the euclidean approximation, and uses a standard cartesian frame with the

origin at O.

Given that the cell coordinates are $x = a\cos\theta$ and $y = a\sin\theta$, define the quantities

$$T_1 = a\sin\theta - \frac{a\cos\theta}{\tan\alpha} + \frac{a_1}{\sin\alpha} \tag{4.108}$$

$$\text{and } T_2 = a\sin\theta + \frac{a\cos\theta}{\tan\alpha} - \frac{a_1}{\sin\alpha}, \tag{4.109}$$

when the regions can be identified by :-

region (i) : $T_1 \leq 0$ and $T_2 \geq 0$,
region (ii) : $T_1 \geq 0$ and $T_2 \geq 0$,
region (iii) : $T_1 \leq 0$ and $T_2 \leq 0$,
region (iv) : $T_1 \geq 0$ and $T_2 \leq 0$.

As for working out the Λ_{1n}, we may as well calculate all five for region (iv) (see figure 4.20), as the others will be a subset of these. Firstly, it is easy to see that $\Lambda_{12} = \theta + \pi$. The remaining four angles are:

(a) $\underline{\Lambda_{10}}$

Given the situation in figure 4.20(b), we can see that

$$\sin(\pi - (\Lambda_{10} - \theta)) = a_1/a \tag{4.110}$$

$$\text{so } \Lambda_{10} - \theta = \pi - \arcsin(a_1/a). \tag{4.111}$$

Care has to be taken to select the correct angle; simplifying the left hand side of equation (4.110) to $\sin(\Lambda_{10} - \theta)$ would give the wrong answer.

(b) $\underline{\Lambda_{11}}$

This situation is depicted in figure 4.20(c), and the known quantities are a, a_1, α and θ. From elementary trigonometry two sides and an included angle determine the triangle uniquely, so the angle $\Lambda_{11} - \theta$ is obtainable. This is easier said than done, however, and we introduce the unknowns, the height h and the length c, temporarily. Using these,

$$h = c\tan\phi$$

$$h = (a - c)\tan(\alpha - \theta)$$

$$h = a_1\sin(\alpha - \theta).$$

$$
\begin{aligned}
c &= a - h\cot(\alpha-\theta) \\
\tan\phi &= h/c \\
&= \frac{(a_1/a)\sin(\alpha-\theta)}{1-(a_1/a)\cos(\alpha-\theta)}.
\end{aligned} \tag{4.112}
$$

Now define

$$\rho_1 = a_1/a \text{ and} \tag{4.113}$$

$$\Upsilon_{11} = \arctan\left\{\frac{\rho_1\sin(\alpha-\theta)}{\rho_1\cos(\alpha-\theta)-1}\right\}. \tag{4.114}$$

Υ_{11} will be negative, and is related to the obtuse angle $\Lambda_{11}-\theta$ by a difference of π. So

$$\Lambda_{11}-\theta = \Upsilon_{11}+\pi, \tag{4.115}$$

$$\text{giving} \quad \Lambda_{11} = \pi+\theta+\Upsilon_{11}. \tag{4.116}$$

In this case $a/a_1 > \cos(\alpha-\theta)$ always, so no problems arise with zero denominators.

(c) Λ_{13}

A similar rigmarole could be gone through as for Λ_{11}, but it is easier to note that it is the mirror image of Λ_{11}, with θ replaced by $-\theta$, and the final result subtracted from 2π. So, using the expression for Λ_{11} above,

$$\Upsilon_{12} = \arctan\left\{\frac{\rho_1\sin(\alpha+\theta)}{\rho_1\cos(\alpha+\theta)-1}\right\}, \tag{4.117}$$

$$
\begin{aligned}
2\pi-\Lambda_{13} &= \pi-\theta+\Upsilon_{12}, \\
\text{therefore} \quad \Lambda_{13} &= \pi+\theta-\Upsilon_{12}.
\end{aligned} \tag{4.118}
$$

(d) Λ_{14}

In a similar way we get Λ_{14} using the expression for Λ_{10} above. Hence, given $\Lambda_{10} = \pi+\theta-\arcsin(\rho_1)$ (4.111), $2\pi-\Lambda_{14} = \pi-\theta-\arcsin(\rho_1)$ so $\Lambda_{14} = \pi+\theta+\arcsin(\rho_1)$.

So, with the Υ_{mn} as defined in equations (4.114) and (4.117),

$$\Lambda_{10} = \theta+\pi-\arcsin(\rho_1) \tag{4.119}$$

$$\Lambda_{11} = \theta+\pi+\Upsilon_{11} \tag{4.120}$$

$$\Lambda_{12} = \theta+\pi \tag{4.121}$$

$$\Lambda_{13} = \theta+\pi-\Upsilon_{12} \tag{4.122}$$

$$\Lambda_{14} = \theta+\pi+\arcsin(\rho_1) \tag{4.123}$$

where Λ_{10} is applicable to regions (iii) and (iv); Λ_{14} is applicable to regions (ii) and (iv); and the other three are applicable to all regions.

For the larger sector.

The line of sight from a cell may exit the sector either through the upper radial edge, the lower radial edge, or through the arc (See figure 4.18). Since $0 \leq \Lambda_{21} < \Lambda_{22} < \Lambda_{23} \leq 2\pi$, the exit point is determined as follows: if $\lambda \geq \Lambda_{23}$ or $\lambda \leq \Lambda_{21}$, the line of sight crosses the arc; if $\Lambda_{21} < \lambda \leq \Lambda_{22}$ the line of sight crosses the upper edge; otherwise it crosses the lower edge. The method of calculation of the distance, D_1 or D_2 (as defined earlier) depends on which range it is.

For later convenience these ranges are defined as

$$\begin{aligned} \mathcal{E} &: \lambda \geq \Lambda_{23} \text{ or } \lambda \leq \Lambda_{21} \\ \mathcal{F} &: \Lambda_{21} < \lambda \leq \Lambda_{22} \\ \mathcal{G} &: \Lambda_{22} < \lambda < \Lambda_{23}. \end{aligned}$$

Looking at Figure 4.22(a), we can again see that $\Lambda_{22} = \theta + \pi$. For Λ_{21}, look at Figure 4.22(b), which extracts the triangle OPQ from 4.22(a). The calculation of Λ_{21} is similar to that for Λ_{11}, with the symbol $\rho_2 = a_2/a$ replacing ρ_1, and with the appropriate changes to get Υ_{2n}. Hence,

$$\begin{aligned} \rho_2 &= a_2/a, \\ \text{and} \quad \Upsilon_{21} &= \arctan\left\{\frac{\rho_2 \sin(\alpha-\theta)}{\rho_2 \cos(\alpha-\theta) - 1}\right\}. \end{aligned} \tag{4.124}$$

Then we have

$$\Lambda_{21} = \theta + \Upsilon_{21}. \tag{4.125}$$

In like fashion to Λ_{13}, we can obtain Λ_{23} from the expression for Λ_{21} with θ replaced by $-\theta$, and the final result subtracted from 2π. So, defining

$$\Upsilon_{22} = \arctan\left\{\frac{\rho_2 \sin(\alpha+\theta)}{\rho_2 \cos(\alpha+\theta) - 1}\right\},$$

we can write succinctly

$$\Lambda_{23} = 2\pi + \theta - \Upsilon_{22}. \tag{4.126}$$

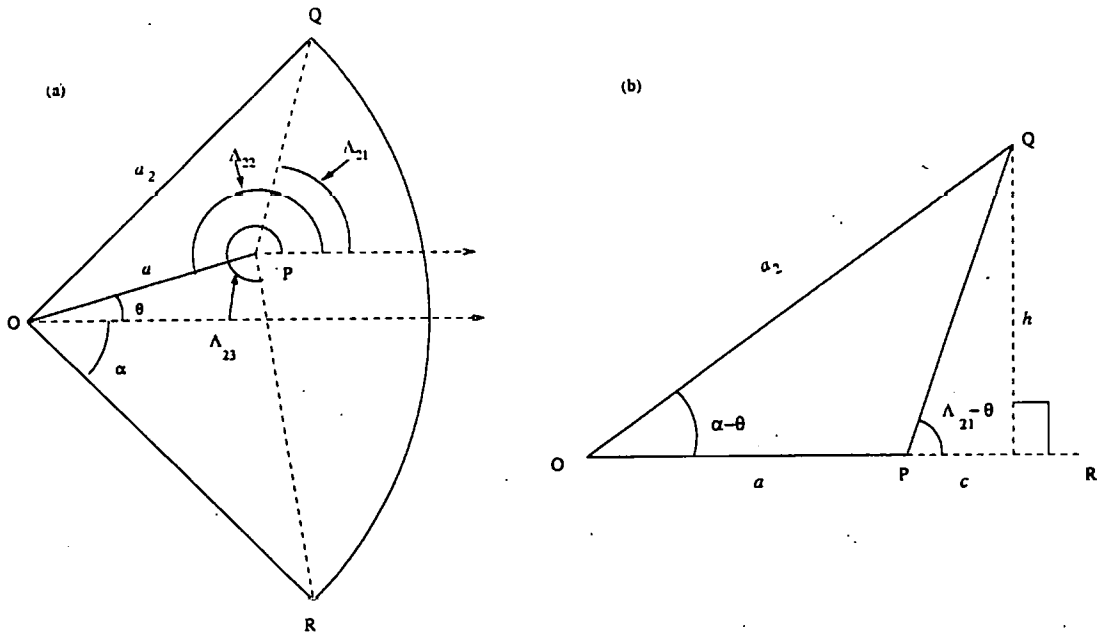

Figure 4.22: (a) Delimiting angles used in the calculation of D_L. (b) Triangle used to obtain Λ_{21}.

These differ from the Λ_{1n} in that they may be acute or right angles, so care has to be taken when the cell is directly below or to the right of the corner (in figure 4.22(b)), as then $\Lambda_{21} - \theta \geq \pi/2$, and problems arise in the calculations. So the above is modified in that, if $a/a_2 = \cos(\alpha - \theta)$, then $\Lambda_{21} = \theta + \pi/2$; and if $a/a_2 > \cos(\alpha - \theta)$, the arctan function returns the value required minus π (arctan returns values from $-\frac{\pi}{2}$ to $\frac{\pi}{2}$). In this case, $\Lambda_{21} = \theta + \pi + \Upsilon_{21}$. Similar considerations apply to Λ_{23}.

Summarising, and using the definitions in equations (4.124) and (4.126),

$$\Lambda_{21} = \begin{cases} \theta + \Upsilon_{21} & \text{if } 1/\rho_2 < \cos(\alpha - \theta) \\ \theta + \pi/2 & \text{if } 1/\rho_2 = \cos(\alpha - \theta) \\ \theta + \pi + \Upsilon_{21} & \text{if } 1/\rho_2 > \cos(\alpha - \theta) \end{cases} \tag{4.127}$$

$$\Lambda_{22} = \theta + \pi. \tag{4.128}$$

$$\Lambda_{23} = \begin{cases} \theta + 2\pi - \Upsilon_{22} & \text{if } 1/\rho_2 < \cos(\alpha+\theta) \\ \theta + 3\pi/2 & \text{if } 1/\rho_2 = \cos(\alpha+\theta) \\ \theta + \pi - \Upsilon_{22} & \text{if } 1/\rho_2 > \cos(\alpha+\theta) \end{cases} \tag{4.129}$$

4.10.3 Distances

Although for any particular cell and λ not all the following distances are required, in general any might be needed, so all must be worked out. The trigonometry may seem somewhat offputting, however it is based on several applications of calculating the distance from a point (the cell) to (i) a line; (ii) a circle, along the line of sight. The assumption is that the area is approximately flat.

Obtain D_1 (to the outer arc)

In this case, we use figure 4.23(b), where the knowns are two sides and an excluded angle. Using the cosine rule, and defining ρ_2 as before,

$$\begin{aligned} a_2^2 &= a^2 + D_1^2 + 2aD_1\cos(\lambda-\theta) \\ 0 &= D_1^2 + 2aD_1\cos(\lambda-\theta) + (a^2 - a_2^2) \\ \text{giving } D_1 &= -a\cos(\lambda-\theta) + \sqrt{a^2\cos^2(\lambda-\theta) - (a^2-a_2^2)} \\ &= a\left[-\cos(\lambda-\theta) + \sqrt{\rho_2^2 - \sin^2(\lambda-\theta)}\right]. \end{aligned} \tag{4.130}$$

When the positive root is chosen this expression gives the correct distance for any value of λ.

Since the square root occurs often in these calculations, it is convenient to define η_i by

$$\eta_i = \sqrt{\rho_i^2 - \sin^2(\lambda-\theta)}, \tag{4.131}$$

when the above becomes $D_1 = a[-\cos(\lambda-\theta) + \eta_2]$.

Obtain D_2 and D_3 (to an edge)

Here we use figure 4.23(c), where the knowns are two angles and one side. The lower edge can be dealt with in a similar fashion to the upper edge, with appropriate changes.

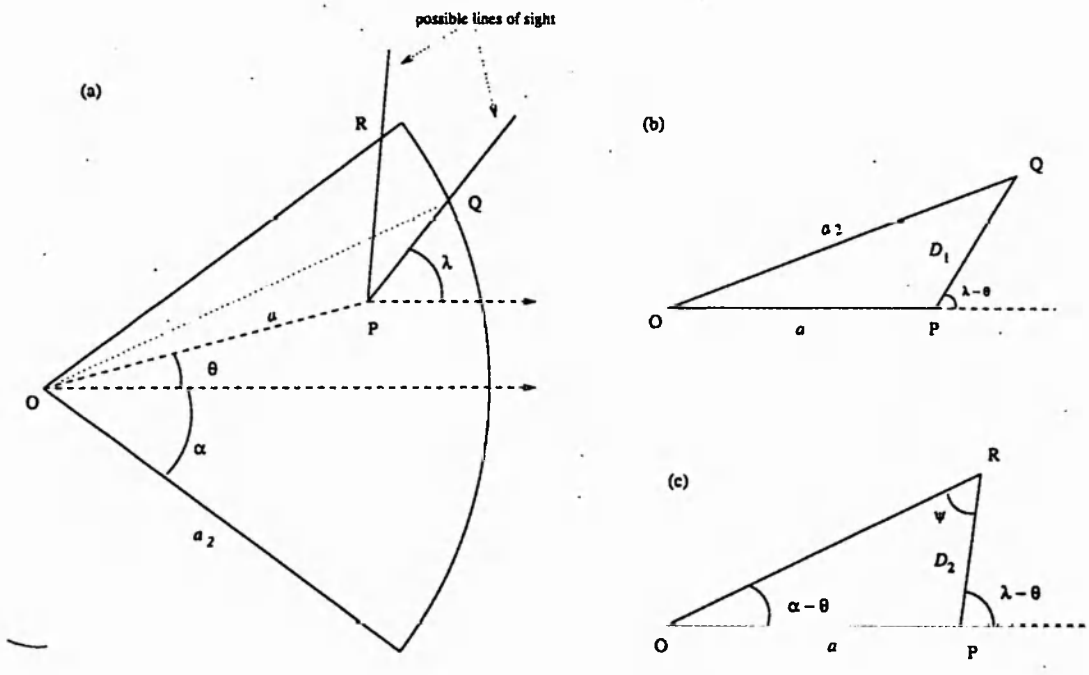

Figure 4.23: Triangles used to obtain D_1 or D_2. (a) shows two possible lines of sight, one exiting via the arc, the other via the upper edge; (b) extracts the triangle for the former, (c) the triangle for the latter. (D_3 is obtained as a "mirror image" of D_2, see text.)

The known quantities are the angles $\alpha - \theta$, $\lambda - \theta$ and the side a. Since the upper angle $\psi = (\lambda - \theta) - (\alpha - \theta) = \lambda - \alpha$, the sine rule can be used:

$$\begin{aligned} \frac{D_2}{\sin(\alpha - \theta)} &= \frac{a}{\sin(\lambda - \alpha)} \\ \text{hence} \quad D_2 &= \frac{a \sin(\alpha - \theta)}{\sin(\lambda - \alpha)}. \end{aligned} \tag{4.132}$$

It should be noted that the denominator cannot be zero, since if $\lambda = \alpha$, the line of sight crosses the arc, not the upper edge, and if $\lambda = \pi + \alpha$, it crosses the lower edge, so we use the formula derived next.

For the lower edge, replace λ by $2\pi - \lambda$ and θ by $-\theta$. This gives the denominator as $\sin(2\pi - \lambda - \alpha) = -\sin(\lambda + \alpha)$, and the numerator as $a \sin(\alpha + \theta)$.

So, with η_i as defined above,

$$D_1/a = \eta_2 - \cos(\lambda - \theta) \tag{4.133}$$

$$\frac{D_2}{a} = \left| \frac{\sin(\alpha - \theta)}{\sin(\lambda - \alpha)} \right| \tag{4.134}$$

$$\frac{D_3}{a} = \left| \frac{\sin(\alpha + \theta)}{\sin(\lambda + \alpha)} \right| \tag{4.135}$$

Obtain D_4 (to the inner arc)

In case (3), all that is required is the smaller of the two possible distances to the arc. The basic situation is seen in figure 4.24(a), and figure 4.24(b) extracts the relevant triangle.

The cosine rule is used, as was done for D_1, and results in

$$\begin{aligned} D_4 &= -a \cos(\lambda - \theta) - a\sqrt{\rho_1^2 - \sin^2(\lambda - \theta)} \\ &= -a \cos(\lambda - \theta) - a\eta_1. \end{aligned} \tag{4.136}$$

Note that in this quadrant the cosine function is always negative, so the first term above is positive, and choosing the negative square root gives the lower value for D_4.

Obtain ΔD_4 (the chord across the inner arc)

In this case the calculation is simple, as it is the difference between the two possible values for D_4 above, and so is twice the magnitude of the square-root term. Hence

$$\Delta D_4 = 2a\sqrt{\rho_1^2 - \sin^2(\lambda - \theta)}$$

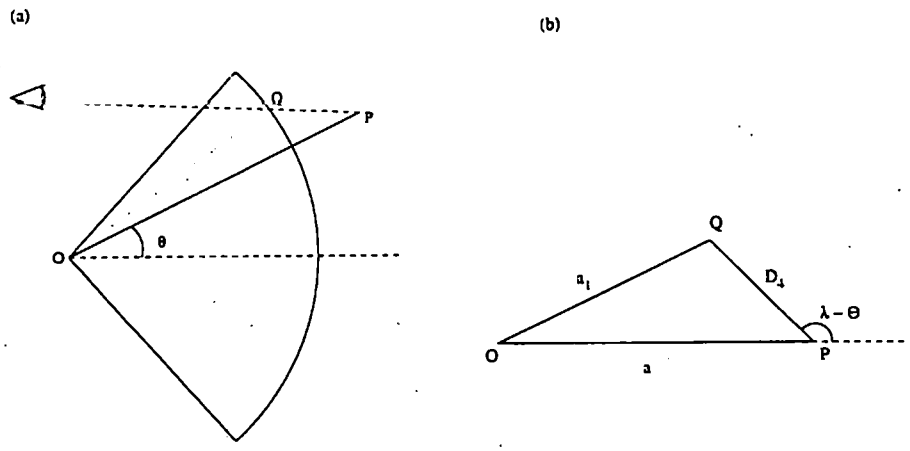

Figure 4.24: Triangles used to obtain D_4. (a) Shows the arc and line of sight. (b) Extracts triangle for this, showing the known values used to obtain D_4.

$$= 2a\eta_1. \tag{4.137}$$

Collating the distances, we get

$$D_1 = a[-\cos(\lambda-\theta)+\eta_2] \tag{4.138}$$

$$D_2 = a|\sin(\alpha-\theta)/\sin(\lambda-\alpha)| \tag{4.139}$$

$$D_3 = a|\sin(\alpha+\theta)/\sin(\lambda+\alpha)| \tag{4.140}$$

$$D_4 = -a[\cos(\lambda-\theta)+\eta_1] \tag{4.141}$$

$$\Delta D_4 = 2a\eta_1. \tag{4.142}$$

Finally, recalling the definitions of $\mathcal{A}$ etc.,

$\mathcal{A}$: $\Lambda_{14} \le \lambda < \Lambda_{10}$ $\quad$ $\mathcal{E}$: $\Lambda_{23} \le \lambda \le \Lambda_{21}$

$\mathcal{B}$: $\Lambda_{10} \le \lambda < \Lambda_{11}$ $\quad$ $\mathcal{F}$: $\Lambda_{21} < \lambda \le \Lambda_{22}$

$\mathcal{C}$: $\Lambda_{11} \le \lambda < \Lambda_{13}$ $\quad$ $\mathcal{G}$: $\Lambda_{22} < \lambda < \Lambda_{23}$

$\mathcal{D}$: $\Lambda_{13} \le \lambda < \Lambda_{14}$

where modulo 2π is assumed, the calculation of distance may be summarised:

$$D_H = \begin{cases} D_1 & \text{if } \lambda \in \mathcal{A}\&\mathcal{E} \\ D_2 & \text{if } \lambda \in \mathcal{A}\&\mathcal{F} \\ D_3 & \text{if } \lambda \in \mathcal{A}\&\mathcal{G} \\ D_4 & \text{if } \lambda \in \mathcal{C} \\ D_1 - \Delta D_4 & \text{if } \lambda \in \mathcal{B}\&\mathcal{E} \text{ or } \mathcal{D}\&\mathcal{E} \\ D_2 - \Delta D_4 & \text{if } \lambda \in \mathcal{B}\&\mathcal{F} \\ D_3 - \Delta D_4 & \text{if } \lambda \in \mathcal{B}\&\mathcal{G} \end{cases} \tag{4.143}$$

4.10.4 Use in the program

The program uses these formulae as follows: the values for a and θ, region numbers (1 to 4 $\equiv$ i to iv), and all relevant Λ_{mn} are stored for each cell in the initial procedures, as these are constant (once the accretion geometry is defined) for each run. Firstly, if the line of sight is up the column ($\zeta_2 \leq \mu \leq \zeta_1$) then the second formula for $\tau_3(\mu)$ (equation 4.97) is used, and the calculation of D_H is unnecessary, otherwise D_H is calculated as above. In this case, the program now checks which wall of the accretion column is intersected by the line of sight; this depends on λ and μ. The relevant formula for $\tau_3(\mu)$ (4.97) is then selected, using D_H in place of d_1/R_* or d_2/R_*. (The program actually uses $\beta_q = a_q/R_*$ rather than a_q for the distances, so calculates D_H as the fractional distance rather than the actual distance.)

To check effects of the D_H algorithm, the program has an option (TVAR) which is set to 1 as a default. If this is altered to 0, then the above calculation of D_H is not carried out, instead an average value is chosen, simulating a run with constant τ_h. Runs using both options have been carried out, and results are discussed in Chapter 5. It should be noted here that using the variable τ_h option leads to much "spikier" pulse profiles, which may indicate that the corners of the emission region are not so sharply defined as the model assumes.

4.11 Partial covering

It was mentioned in Chapter 1 that the accretion curtain may not be a simple homogeneous flow, and that it may have clumps of greater density, interspersed with gaps of lower density. Hence it has been proposed that the accretion has "multiple column densities" rather than a single column density, and that the absorption isn't a perfect cover, but that it ranges from more opaque to less opaque. The latter effect is usually referred to as "partial covering", see, for instance, Norton & Watson (1989) and Hameury, King & Lasota (1989).

This has an observable effect, in that the modulation depth of the spin pulse profile will not follow the theoretical dependence on energy if a single column density is used. Observations to date have confirmed this, and so models do assume partial covering and multiple column densities.

This possibility has been provided for in the program, and the parameter COV can take any value in the range 0–1, with 0 being always transparent and 1 meaning always covered.

The parameter CDEN is a switch, having the value 0 when a single column density is being simulated, and 1 for multiple column densities. If it is set to 1, a number is chosen from a gaussian distribution centred on zero, with standard deviation 0.5. The range is cut off at ± 3, this and the standard deviation being chosen arbitrarily. The number is then used as an exponent of 10, resulting in a multiplier ranging from 10^{-3} to 10^{3}, with the distribution carrying over from above. This is then used to multiply the density (as calculated in section 4.6) for the cell. (The process is carried out individually for each visible cell.)

4.12 Orbital dips

In view of the observations of several IPs (for example recent observations of AO Psc and V1223 Sgr) revealing orbital modulations in the form of quasi-sinusoidal variations and/or dips at particular orbital phases (typically around 0.7 from orbital maximum), three parameters have been introduced, replacing the old NHSTREAM. These are

N_{H_1} : the assumed extra N_H value causing the dip ($\times 10^{21}\mathrm{cm}^{-2}$);
N_{H_2} : the equivalent for the sinusoidal component;

ϕ_{N_H} : the phase lag for the sinusoidal component.

The cause of these effects is speculated to be material thrown up at the point where the stream from the secondary hits the outer (or inner) edge of the accretion disc. This would result in an absorber fixed in the orbital frame, and at high inclination angles would be expected to result in similar dips to those seen.

Since a complete theory of these is lacking, the above parameters are currently independent, and may be tailored to particular systems.

4.13 The revised model parameters

The program has been amended to allow input of parameters by a file if required. The user now has an option, input by file or by screen. Hence a series of runs can be made using files with the same basic parameters, varying a selected set.

Several parameters in the list in section 4.1.1 are no longer used, having been replaced by alternatives; and some new parameters have been introduced in accordance with advances in the theory.

The new set of parameters is:-

Symbol	Parameter	description
p_{spin}	PSPIN	White dwarf spin period(sec)
p_{orb}	PORB	System orbital period(sec)
i	ANGI	Inclination angle (degrees)
m_p	ANGM(P)	Magnetic colatitude(degrees); one for each pole
γ	GAMMA	Lower pole azimuthal lag(degrees)
δ	AMAX	(Unchanged from old parameter set)
M_*	MASS	Mass of white dwarf (R_* assumed correlated by use of Nauenberg's formula)
$\dot{M}_{17}$	M17DOT	Accretion rate in units of 10^{17}gm s^{-1}
	FLUXFUN	Pole switching function for stream-fed component (see section 4.5)
N_{H_1}	ORBNH_DIP	Extra N_H causing orbital dip ($\times 10^{21}$cm^{-2});

N_{H_2}	ORBNH_AMP	Extra N_H: sinusoidal component;
ϕ_{N_H}	ORBNH_PHS	The phase lag for the sinusoidal component.
	NPC	no. of polecaps
	PCQ‡	Polecap usage:
	NTIME†	No. of time bins in lightcurve
Δt	TBIN†	Time bin size (seconds)
	NPHASE†	No. of phase bins in each fold
ΔA	DELA†	Fraction of surface area covered by a single cell
E	ENERGY†	Pseudo energy value to get varying absorption (keV)
ϵ	EPSILON	Stream incident angle to radius
$R_{mag}(1)$	RMAG(1)	Outer magnetic capture radius
$R_{mag}(2)$	RMAG(2)	Inner magnetic capture radius
f_s''	CFRACS(P)	Fraction of cells emitting in each ring (stream-fed)
f_d''	CFRACD(P)	Fraction of cells emitting in each ring (disc-fed)
	CDEN	Switch to allow multiple column densities
	COV	Covering fraction if partial covering simulation
	PH†	Number of phase bins in pulse profiles
	OUTB†	Binning factor for time series
	NORM‡	Switch set if time series to be normalised
	ABSO‡	Zero for occultation only (no absorption)
	TVAR‡	Set to zero for constant τ_h

† These parameters are used for data analysis (so are not system parameters), for example simulating how the dataset is binned up, similar to the analysis of real data. The energy parameter would correspond to the maximum response window of a particular telescope.

‡ Used for testing the model, by comparing various effects separately, e.g. we can "switch off" absorption effects, etc. (Impossible in the real world!)

In the above, known parameters for systems include the spin and orbital periods, and in some cases limits on the inclination angle. The orbital extra N_H components may be estimated from orbital pulse profiles. Most of the rest are unknown. Values for $R_{mag}(1)$ and $R_{mag}(2)$ could be estimated from accurate measurements of the magnetic dipole and assumptions on $\dot{M}_{17}$, using Hameury, King & Lasota (1986), but for most systems they must be guessed

at. An assumption used is also that the capture radii are about the same for the disc and stream-fed components. As this may not be the case, a future enhancement may be to provide separate R_{mag} values for the two modes, thereby increasing the system parameters by two.

Assumptions used in most of the tests are that NPC = 2, $f_d'' = 0.5$ (that is the disc-fed accretion occurs from the whole inner edge, going to the nearest pole from each point), and $f_s'' < f_d''$, (f_s'' is usually taken to be 0.1 or 0.2), as the stream is expected to have a much smaller azimuthal spread. If evidence occurs for no stream-fed component, δ can be set to 0.5, otherwise an estimate within $0.5 < \delta \leq 1.0$ has to be used.

Summarising, there are thirty-four parameters, of which

23 are intrinsic, of which
- 2 parameters (p_{spin} and p_{orb}) are known,
- 1 is known if the spin profile is symmetric ($\gamma = 180°$),
- 3 parameters (ϕ_{N_H},N_{H_1},N_{H_2}) can be estimated from the orbital pulse profile ,
- 1 parameter (NPC) is assumed to have the value 2,
- 2 parameters ($f_d''(1)$ and $f_d''(2)$) are normally assumed to have the value 0.5,
- 1 (CDEN) is assumed to have the value 1 (i.e. multiple column densities) in general,
- 1 (ϵ) has little effect except in stream-fed accretion using the sharper weightings;

leaving 12 important but not known:

i, m_1 and m_2, δ, M_*, $\dot{M}_{17}$,
$R_{mag}(1)$, $R_{mag}(2)$, $f_s''(1)$, $f_s''(2)$, COV, FLUXFUN.

In cases where the stream-fed component is known to have little effect,
we can assume: $\delta = 0.5$ and FLUXFUN is irrelevant, as are $f_s''(1)$ and $f_s''(2)$.
Further, if constraints for i are known (from eclipse data for instance),
this can be put in the "known" category.

In the best case, then (stream-fed), there are seven independent parameters to manipulate, namely: m_1 and m_2, M_*, $\dot{M}_{17}$, $R_{mag}(1)$, $R_{mag}(2)$ and COV.

4.14 Program description

Here is presented a skeleton description of the program "lc_model", which is written in FORTRAN77, referencing the relevant equations used from this chapter.

4.14.1 Overview

The program has three major parts,

A: **Initialisation**, covering parameter input and calculation of run constants;

B: **Main timestep loop**, which calculates the theoretical observed X-ray flux at each timestep, storing as a simulated lightcurve;

C: **Termination**, in which the stored lightcurve is binned up and output to a file, along with various pulse profiles. Also a file of the parameters and run constants is output.

4.14.2 Processes in detail

Function title/process;	Source
A Initialisation	
1 Read input parameters	
- overwrite selected defaults.	
- calculate run constants.	
2 FOR each **POLECAP**:-	
define accretion geometry, i.e. calculate:	
NRINGS–number of rings	eqn 4.2
TOTCELLS–total accreting cells	eqn 4.3
β_i	eqn 4.8
α	eqn 4.43
ζ_i	eqn 4.86
τ_v(disc-fed)	eqn 4.70

For each **accreting cell**

Λ_{mn} *CALCDISC*

(These last are stored for each cell.) & *CALCSTREAM*

END of cell loop

END of **POLECAP** loop.

B. **Timestep Loop processes**

FOR each **TIMESTEP**

1 Calculate:

Phase-dependent fields

Stream–Mag field angle eqn 4.37

Hence flux to each pole (FLUXFUN) Section 4.5

λ_0–line of sight relative to

disc-fed region eqn 4.103

'Migration' angle for stream fed emission region.

(Function of beat phase)

2 Zeroise TOTFLUX.

2.1 FOR each **POLECAP**

calculate τ_v(stream-fed) eqn 4.70

TOTFLUX = TOTFLUX + *CALCFLUX(function)*

(Total flux for this polecap/timestep)

END **POLECAP** loop

2.2 Store TOTFLUX in lightcurve table.

END **TIMESTEP** loop.

C. **Termination**

Output:

a) Light-curve (binned up as per parameters);

b) Data folded at P_{spin};

c) Data folded at P_{orb};

d) Data folded at P_{beat};

e) Spin profile from orbital phase 0.75 – 0.25;

f) Spin profile from orbital phase 0.25 – 0.75;

g) File of system parameters and run constants.

4.14.3 Functions and subroutines

CALCFLUX

FOR each **accreting RING** :-

1 Calculate:

number of cells in ring ($ncell_r$)	eqn 4.3
number of cells accreting	($ncell_r \times f''$)

2 FOR each **CELL**

test1: accreting via disc and/or stream?

no – ignore & pass to next cell.

transform to observer's frame	*CALCZ*

test2: Is Z < 0 (i.e. occulted)?

yes – ignore & pass to next cell.

If accreting and visible, calculate:

LUM: luminosity (disc+stream)	eqn 4.38
μ - line of sight elevation	section 4.9

IF $\zeta_1 \leq \mu \leq \zeta_2$

THEN $\tau_{tot} = \tau_v$ (*down* the column)

ELSE $\tau_{tot} = CALCTAU$(function)

ENDIF

FLUX = FLUX + LUM$\times \exp(-\tau_{tot})$

END of **CELLS**

END of **accreting RINGS**

Value FLUX returned to timestep loop.

CALCZ

Get cartesian coordinates of

current cell in *magnetic* frame.

(Depends on ring number, cell number and Δ_ϕ)

Transform to *spin* frame	eqns 4.4
Rotate through current *phase*	eqns 4.5
Transform to *line of sight* frame	eqns 4.6

CALCDISC

Variables a_1, a_2, α, a, θ plus others are passed to this function. All delimiting angles are related to the disc-fed geometry.

For the current cell

calculate the delimiting angles Λ_{mn}	eqns 4.127 to 4.129 & 4.123
store all the Λ for later use in the function *HORIZDIST*	(section 4.10)

CALCSTREAM

As above, but for stream-fed sector parameters.

CALCTAU

Zeroise hdist_D & hdist_S

IF current cell disc fed,

calculate hdist_D	*HORIZDIST*

ENDIF

IF current cell stream fed,

calculate hdist_S	*HORIZDIST*

ENDIF

Calulate τ_D and τ_S eqn 4.97

- For τ_D use TAUV_DISC;
- For τ_S use TAUV_STREAM;

$\tau_{tot} = \tau_D + \tau_S$.

RETURN τ_{tot} as value of function.

HORIZDIST

A subroutine to calculate the horizontal distance from a cell through the accretion curtain.

Use stored Λ_{mn} to determine which distances required (see section 4.10.1);

Case (1):	$D_H = D_1$	eqn 4.138
Case (2):	$D_H = D_2$ or D_3	eqn 4.139 or 4.140

Case (3):	$D_H = D_4$	eqn 4.141
Case (4):	$D_H = D_1 - D_4$	eqns 4.138 and 4.141
Case (5):	$D_H = D_2 - D_4$ or $D_3 - D_4$	eqns 4.139 or 4.140 & 4.141

Chapter 5

Simulation of X-ray emission from IPs

5.1 Introduction

In this chapter the results of running the program with various parameter sets are described. The first stage is to check the reaction to parameters, and to examine the types of light curves and profiles to which these lead. After this a more detailed look at particular combinations is taken, with reference to observational data.

Results using different accretion modes (disc-fed, stream-fed or disc-overflow) are examined (this is partially done in the first stage of parameter testing), including examination of the resulting power spectra, for the different modes and for orbital/beat effects. Spin-fold modulation depths, and dependency on the energy "window" are examined. A look is taken at the orbital folds, with and without the use of orbital absorption parameters.

It should be noted that currently this is a "forward" model, so the testing has mainly been testing the effects of varying parameters, rather than formally fitting to data.

5.2 Parameter testing

Table 5.1 gives a set of ranges of parameter values used in testing the reaction of the model. A base set of parameters is used, and most are varied one at a time over a plausible range to get the different outputs. In some cases linked parameters (for instance $R_{mag}(1)$ and $R_{mag}(2)$) are tested in conjunction. Other combinations are δ, the disc-stream parameter, which is linked to the function governing how the stream is distributed between each pole, as also is ϵ, the incident angle of the stream (if present) to the field lines at the magnetic capture radius.

So, for example rows (4) and (5) constitute one test, as do rows (7) and (8). The symbols below the line (rows (18) on) are not input parameters, but result from the choices of $R_{mag}(q)$ in the test above.

The main method of comparison is to examine the spin profile, although when appropriate other profiles and power spectra may be considered. The comparison can be done by eye; however, a program to compare pairs of output by least-squares has been written, but this has to be used carefully, since if the option to normalise the output is chosen, differences in magnitude may be washed out. Ideally a quantitative comparison should be done, but to do this properly would require an estimate of standard deviation, perhaps during the binning-up into phase bins as the pulse profiles are built up.

Figure 5.1 shows the time series for two orbits, the whole series folded at various periods, and the power spectrum for the base set of parameters (from Table 5.1). The obvious features are the spin pulse seen in the light curve, with a corresponding peak in the power spectrum; a definite signal at the beat period; and a small signal at the orbital period, which is interpreted as a result of the interaction with spin and beat effects (c.f. Norton et al, 1996), as no explicit orbital modulation is used in the base set.

The model is found to be strongly sensitive to inclination i, energy E, azimuthal lag γ, magnetic colatitudes m_1 and m_2, and δ. The sensitivity to accretion rate depends sharply on energy. We now consider the parameters individually (the effects of varying energy are considered in more detail in section 5.3).

Table 5.1: Ranges of variation of parameters for initial testing

Parameter	Base value	.....Variations.....					
(1) i	65	0	10	20	30	40	50
(1b) i		60	65	75	80	85	90
(2) m_1	10	0	5	10	15	20	25
(3) m_2	170	180	175	170	165	160	155
(4) $R_{mag}(1)$	10	10	13	16	19	22	25
(5) $R_{mag}(2)$	7	7	10	13	16	19	22
(6) $R_{mag}(1)$	10	10	13	16	19	22	25
(7) $R_{mag}(1)$	10.0	10.0	14.0	18.0	22.0	26.0	30.0
(8) $R_{mag}(2)$	7.0	7.0	9.76	12.52	15.28	18.03	20.8
(9) M_*	0.75	0.5	0.6	0.75	0.9	1.1	1.25
(10) $\dot{M}_{17}$	1.0	0.8	1.0	1.5	2.0	5.0	10.0
(11) f''_d	0.50	0.50	0.45	0.40	0.35	0.30	0.25
(12) f''_s	0.10	0.10	0.20	0.25	0.30	0.35	0.40
(13) γ	180	180	170	160	140	120	90
(14) δ	0.6	0.5	0.6	0.7	0.8	0.9	1.0
(15) ϵ	0.0	0.0	20.0	40.0	60.0	80.0	90.0
(16) COV	1.0	1.0	0.85	0.70	0.55	0.40	0.25
(17) E/keV	4.0	0.5	1.0	2.0	4.0	8.0	16.0
(18) β_1	18.1	18.1	15.9	14.2	13.1	12.1	11.4
(19) β_2	21.9	21.9	18.1	15.9	14.2	13.1	12.1
(20) f_{-2}	3.6	3.6	2.5	2.0	1.6	1.4	1.2
(21) f'	0.17	0.17	0.17	0.17	0.17	0.17	0.17

Notes:

(1) All angles in degrees of arc unless stated otherwise.

(4)-(8) These are in units of the white dwarf radius. The $R_{mag}(q)$, being linked, are tested together. Rows (4) & (5) consitute one test, in which both are increased, keeping the difference constant. The resulting values of β_1 and β_2 are shown in the lower box.

(6) $R_{mag}(1)$ is increased, thereby increasing f' for constant f.

(7) & (8) The $R_{mag}(q)$ are increased so as to decrease f while keeping f' constant. (c.f. (20) & (21))

(11) The values for f''_d, the disc-fed accretion arc spread, are assumed the same for upper and lower poles in this test. This test is run three times, with δ having values of 0.5, 0.6 and 0.8 in each case, as disc-fed accretion is linked to this parameter.

(12) The values for f''_s are also assumed the same for upper and lower poles. This test is also run three times, with δ having values of 0.6, 0.8 and 1.0.

(14) ($\equiv$ AMAX): This test is run for each of the possible "flip" functions.

(15) This test is also run for each of the possible "flip" functions.

(17) Energy response is tested with combinations of δ, COV, and with/without multiple column densities.

(18) & (19) These are not input parameters, but correspond to the values of $R_{mag}(q)$ in rows (4) and (5).

(21) & (21) Likewise these values of f_{-2} and f' correspond to the test in rows (7) and (8).

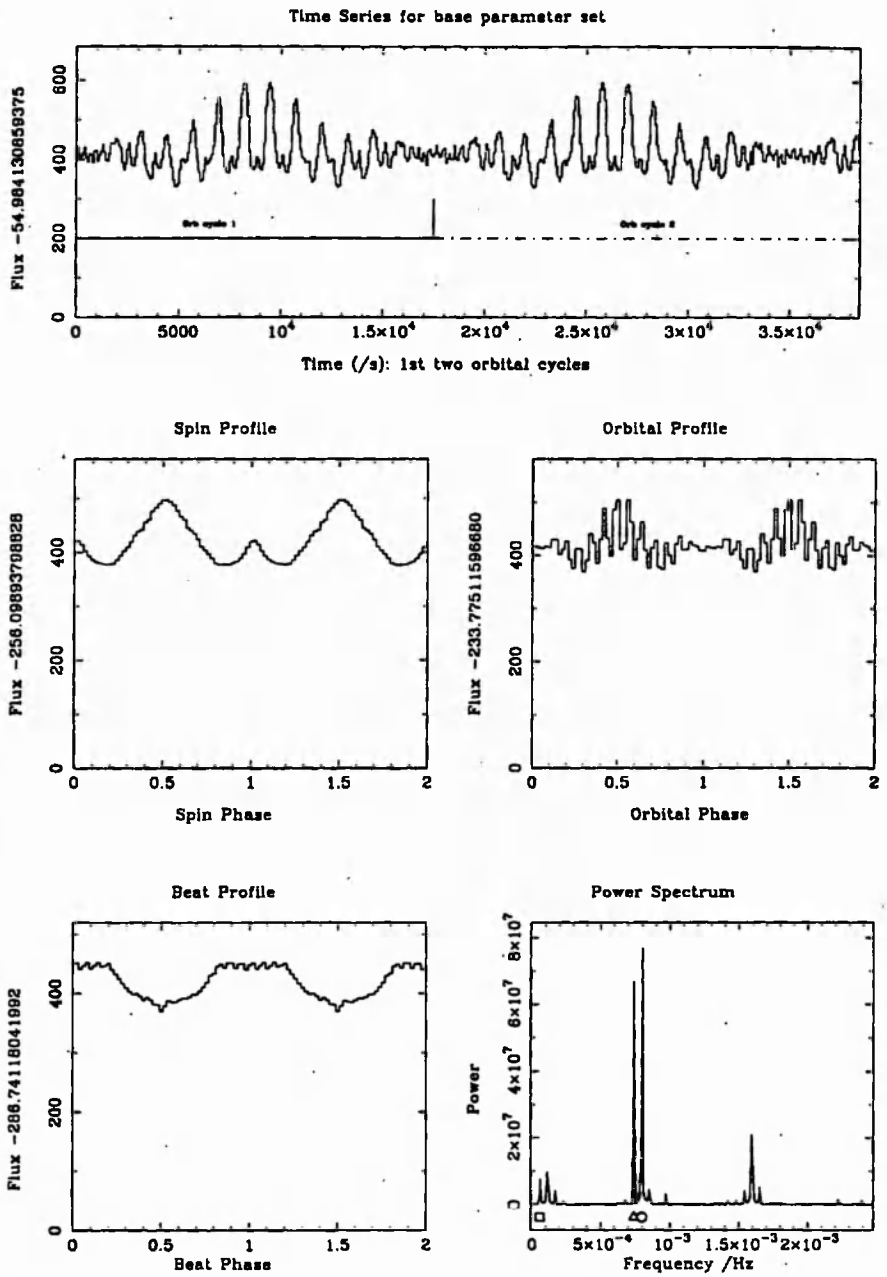

Figure 5.1: Data from the base parameter set run. The top panel shows the light curve over two orbital cycles; the profiles and power spectrum are also shown. The symbols used in the power spectrum: circle – spin frequency; triangle – beat; square – orbital frequency.

5.2.1 Inclination, i

Varying this parameter has a large effect on the profiles. Tests using the values from the parameters given in table 5.1, were carried out using a range of values for the disc-stream parameter, δ. At $i = 0°$, no spin modulation is seen in disc-fed mode. A small modulation in the beat profile is seen when the mode is set to disc-overflow ($\delta = 0.6$); this becomes increasingly prominent as the stream-fed proportion increases.

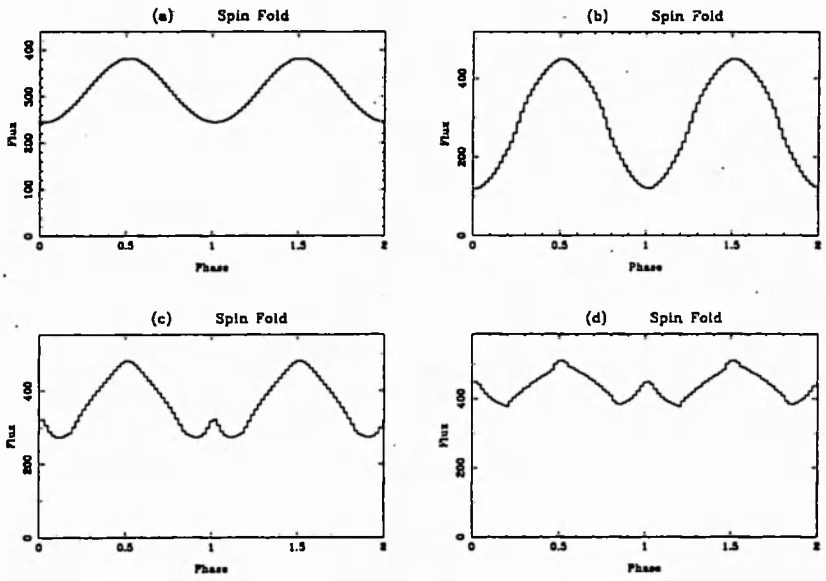

Figure 5.2: Variation of response with different i with disc-fed accretion. The values of i are: (a) 10°, (b) 30°, (c) 50° and (d) 75°. Other parameters as in base set.

Using non-zero values of $i \lesssim 40°$ the spin profiles are sine-like curves for disc-fed accretion (figure 5.2). With stream-fed accretion the curves are noisier, and sharper at the minimum for low inclination (figure 5.3). With these values, and using capture radii $R_{mag}(1) = 10R_*$, $R_{mag}(2) = 7R_*$ and $m_1 = 10°$, β_1 and β_2 work out at 18° and 22° respectively, meaning that for these ranges of i the elevation angle μ is high for spin-phase zero, leading to strong absorption. For $i \gtrsim 45°$, a small peak at spin phase zero becomes noticeable, increasing as i increases, in disc-fed accretion. In stream-fed mode this peak does not appear, but the curves become flatter at the top. At extremely high inclination, $i \gtrsim 85°$, the profile becomes quite irregular, with multiple peaks in disc-fed accretion. For stream-fed accretion, at high

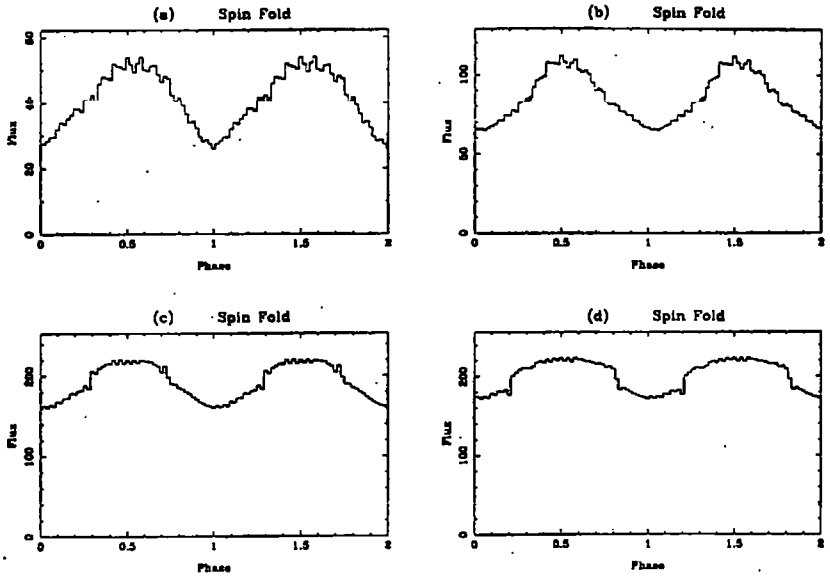

Figure 5.3: Variation of response with different i with stream-fed accretion. The values of i are: (a) 10°, (b) 30°, (c) 70° and (d) 75°. Other parameters as in base set.

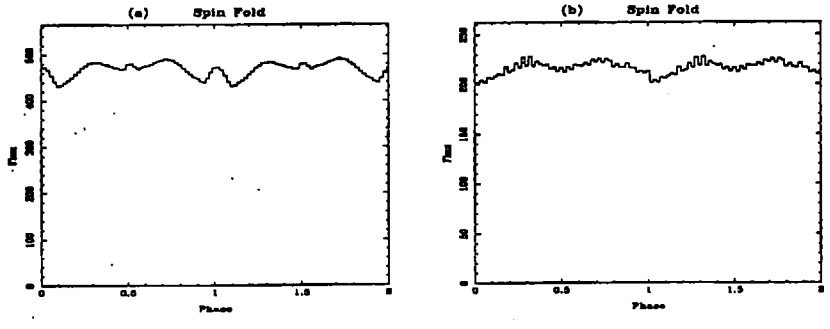

Figure 5.4: Spin profiles at high inclination ($i = 87°$). Left hand panel is disc-fed only, right-hand panel is stream-fed only.

inclinations the spin profile takes on an increasingly "humped" shape, then becoming less coherent at $i \gtrsim 85°$. The humps are seen in figure 5.3, and spin folds for $i = 87°$ are seen in figure 5.4.

The lack of spin modulation at $i = 0°$ is to be expected; the modulation at the beat period for stream-fed and disc-overflow modes is interpreted as being caused by the varying accretion on to the upper pole at this period. Naturally no such variation occurs in disc-fed only mode. The sine-like curves seen for $i \lesssim 40°$ are interpreted as the effect of absorption, thus the minimum at spin phase zero occurs on looking down the accretion column. The lower pole is not visible at these inclinations. The small peak at phase zero for higher inclinations may be interpreted as follows: at phase zero, the elevation angle μ is such that the line of sight is not directly down the column, and as noted in Chapter 4, τ can drop sharply with μ. At this phase the majority of cells are seen through an average horizontal distance of d_{rad} (to use the terminology of Chapter 4) through the absorber, which is relatively the shorter distance. As the star turns, more of the accretion curtain becomes "edge-on" to the observer, hence more cells have the line of sight passing through a horizontal distance of d_{trans}, resulting in more absorption. Past about phase 0.25, the line of sight is now through the opposite wall of the curtain, and at a lower μ, so an increase in brightness is seen. Also the lower pole may become visible, with an extra contribution. At high ($\gtrsim 60°$) inclinations, parts of the upper pole accretion region are occulted by the star, which actually causes the luminosity from the upper pole to drop further, but as the lower pole becomes visible this effect is more than compensated.

The double-peak effect is still seen when f''_d is reduced to 0.1, as the arc is still longer than it is wide. We may ask, then, why doesn't the model show double peaks for stream-fed accretion? This can be explained as the consequence of the accretion arc "migrating" around the pole with the beat phase, hence its different angles to the observer average out during an orbit, assuming several spin cycles per orbit. The peak also disappears in disc-fed mode when the program is run with the option to ignore the horizontal distance effect, that is taking an "average" τ_h (as calculated in Chapter 4 using the King & Shaviv formula). Thus the double peak is associated with variable horizontal τ in the current model, and seems to indicate an arc fixed on the white dwarf surface, as is assumed for the disc-fed portion.

At high inclinations, the situation can be complex. Consider the base parameters given above. The accretion arc is at an angle of 18–22° from the magnetic pole (average 20°), which is itself 10° from the spin axis. Hence the mid-point of the accretion arc is at 30°

from the spin axis for disc-fed accretion, and varies from 30° to 10° from the spin axis for stream-fed accretion. In the latter case, which depends on the beat phase, the 30° would correspond to maximum accretion to this pole. Hence at spin-phase zero, the elevation angle μ is $90° - (i - 30°) = 120° - i$ for disc-fed accretion, and from $120° - i$ to $80° - i$ for stream-fed accretion. At spin phase 0.5, the relevant elevations would be from $60° - i$ (disc and stream-fed) to $80° - i$ (stream-fed at beat-phase zero). The point is, that when $\mu < 0°$ the cells involved become occulted, and this effect can occur when $i > 60°$. In the general case, using the symbolism from Chapter 4, occultation can occur when $i + m_1 + \beta > 90°$. However, in the symmetrical dipole case, at spin phase zero the lower pole becomes visible for high inclinations; this is discussed in detail in King & Shaviv (1984), in their analysis of the occultation only model. The current model still retains these effects, although now the elevation angle has a further complication on the outcome.

5.2.2 Disc-stream parameter, δ

The variation of disc-stream proportion has a marked effect on the spin profile, as seen in figure 5.5.

It is noticeable that the curve gets noisier as the stream-fed proportion increases, and the phase-zero peak disappears (at $i = 65°$). Also the maximum (at phase 0.5) tends to flatten off, whereas the minimum sharpens up. Figure 5.6 shows the effect on the beat profile, with stream-fed accretion showing a dip at beat phase zero. (This is defined in the program as when the upper pole is on the farther side from the secondary. Since the model starts with the pole pointing towards the observer – spin phase zero, and the secondary at superior conjunction – orbital phase zero, then beat phase zero also starts at time zero.)

Power spectra for these are considered later (in section 5.6).

Using $\delta = 0.5$ means accretion to the pole is constant. For other values a variation at the beat period occurs, with resulting effects on the luminosity and the amount of absorption.

5.2.3 Azimuthal extent of accretion arc, f''

Checking the angular spread of the accretion arcs (relative to the magnetic pole), i.e. the parameters f_a'' and f_s'' (giving the lengths of the arcs as a fraction of a full circle) it is found

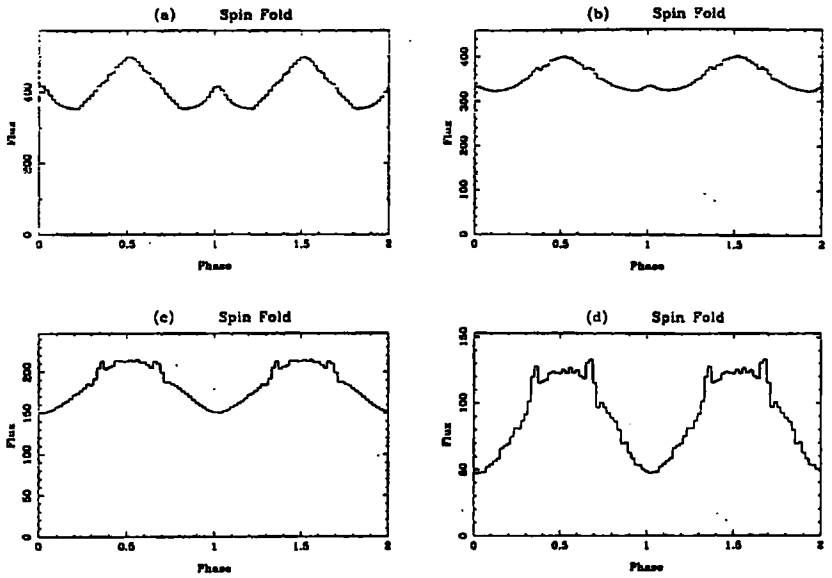

Figure 5.5: Spin profiles from the parameter set in table 5.1, showing the effect of varying the amount of disc and stream-fed accretion. Panel (a) has $\delta = 0.5$ (disc-fed only), (b) has $\delta = 0.8$ (disc-overflow), (c) has $\delta = 1.0$ (stream-fed). These use sinusoidal weighting for stream distribution. Panel (d) has $\delta = 1.0$, but with 100% flip for stream weighting.

that the model is moderately sensitive to f''_d, even with δ as high as 0.8. With f''_s, it is marginally sensitive at $\delta = 0.6$, and highly sensitive at $\delta = 1.0$. Figure 5.7 shows this effect. Alterations to f''_s show no effect when in disc-fed mode. Likewise varying f''_d in stream-fed mode result in no change, both these results are as expected.

In each case, when the disc-stream proportion affects the parameter, the magnitude of the signal increases with increasing f'', whereas the modulation depth decreases.

This parameter affects the area of the accretion region, so a more extended arc will have a relatively lower luminosity per cell, and the density of the absorber will be lower. The lower luminosity is counteracted by the greater luminous area and the lessening of absorption, which may explain both the increase in magnitude and the reduction in modulation depth. Possible changes in the emitted X-ray spectrum are not currently modelled.

The other effect of these parameters is to alter the geometry of the accretion region, which should affect the different τ_h.

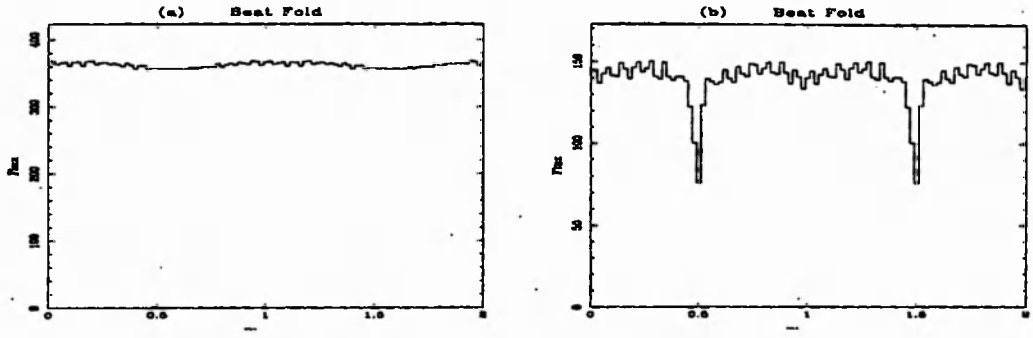

Figure 5.6: Effect of varying δ on beat modulation. (a) $\delta = 0.5$; (b) $\delta = 1.0$, both at $i = 50°$.

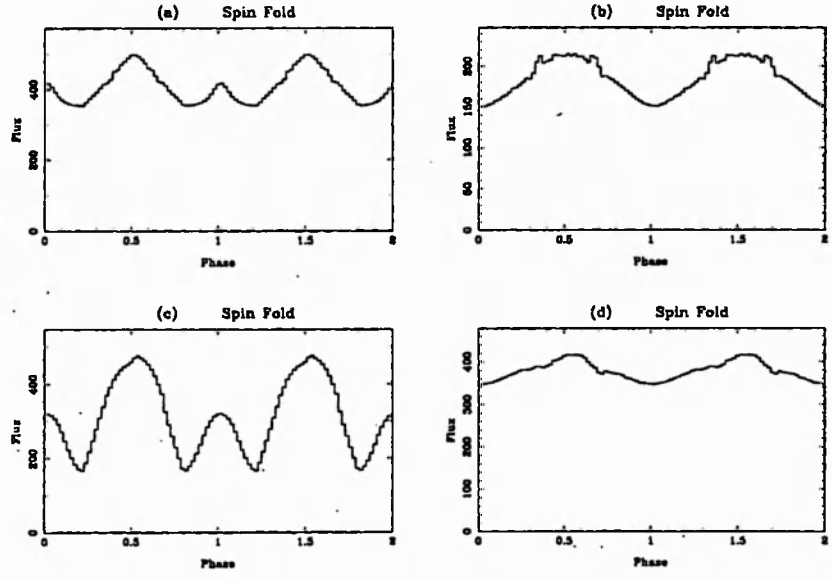

Figure 5.7: The left-hand column shows the variation with f_d'' for disc-fed accretion (top row: $f_d'' = 0.5$, bottom row:$f_d'' = 0.25$). The right-hand column shows the variation with f_s'' for stream-fed accretion (top row: $f_s'' = 0.1$, bottom row:$f_s'' = 0.4$).

5.2.4 Covering fraction and column densities, COV and $CDEN$

The covering fraction, COV, has an extremely strong effect at low energies, in effect the uncovered parts drowning out the contributions from the covered parts, which are effectively opaque. At higher energies the effect is less. In fact at $E = 0.5$ keV little modulation is seen in the full covering testing.

The option to use multiple column densities is invoked by setting the switch $CDEN$ to 1. When this option is chosen, the density is firstly calculated as in Chapter 4, then is multiplied by a number taken from a Gaussian distribution. In detail, a number is chosen from the range (-3,3), with standard deviation 0.5 and centred on zero; 10 is raised to this power, and the result used to multiply the density above. Thus it ranges from 10^{-3} to 10^{3} times the orginal density. Using multiple column densities has the effect of lowering the energy range at which particular shapes are seen.

At low ($\lesssim 1.0$ keV) energies, reducing the covering fraction even to ~ 0.99 has a surprisingly large effect on the results. This can be interpreted as due to the majority of the cells being covered by an opaque absorber, for many timesteps, and a small number producing zero absorption. This can lead to a few phase bins containing zero, with others having random amounts.

Options with various settings of COV and $CDEN$ will be considered further in section 5.3, when modulation depths are discussed.

5.2.5 Incident angle of stream, ϵ

The effect of varying ϵ, the angle at which the stream encounters the magnetic field (relative to the line joining the stars), is small. In fact using the sinusoid variance of stream-fed proportion to stream-field angle there is no discernible difference, even using stream-fed only mode. Using the sharper variations ($\cos^{0.1}$ and 100% flip), the model is marginally sensitive with $\delta = 1.0$, i.e. stream-fed mode. The shape of the curve varies slightly, and there is a small phase-shift between the extremes $\epsilon = 0°$ and $\epsilon = 90°$. Figure 5.8 shows the maximum difference obtainable, using stream-fed only accretion, weighting of $\cos^{0.1}$, and ϵ varying from 0–90°.

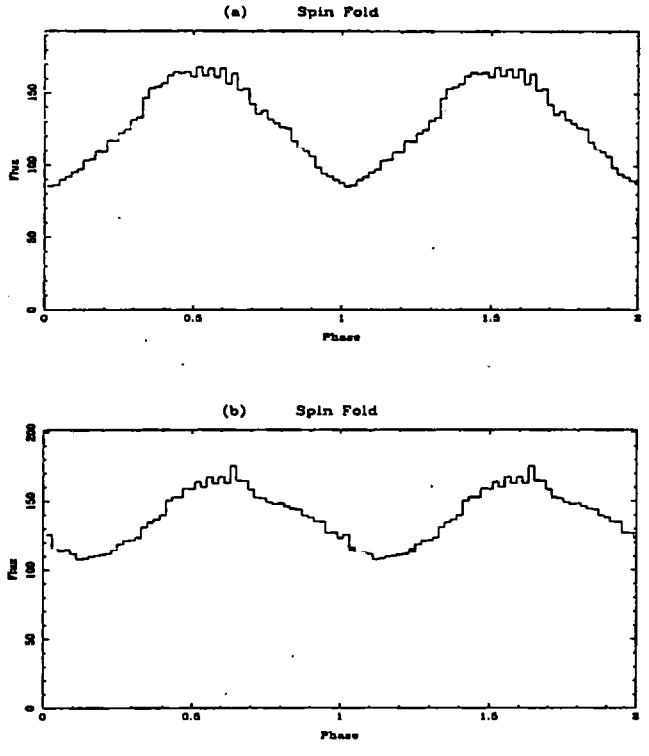

Figure 5.8: (a) has $\epsilon = 0°$, (b) has $\epsilon = 90°$. The weighting function is $\cos^{0.1}\psi$.

The way ψ varies as the beat phase varies will affect the amount of accretion to each pole, as the model is constructed. Thus ϵ has a slight effect on this, and will lead to the small phase shift seen.

5.2.6 Mass of white dwarf, M_*

The model is sensitive to white dwarf mass as far as the total output is concerned, but the actual shape of the pulse profiles is the same. Thus if the output is normalised no difference is seen. Energy has no discernible effect on this.

The increase in magnitude in the output as M_* increases reflects that this parameter only affects the brightness as the program is designed at present. From equations 4.85 and 4.86, we note that the optical depth of the column above the shock varies inversely as $(M_* R_9)^{1/2}$,

and in the ranges of M_* chosen, 0.5 to 1.25, this varies varies in proportion from a minimum of about 0.6 to a maximum of 0.71, assuming Nauenberg's relation. The effect on optical depth is therefore small, hence the lack of effect on the shape of the curve.

5.2.7 Accretion rate, $\dot{M}_{17}$

The model is extremely sensitive to accretion rate $\dot{M}_{17}$ for values $\gtrsim 1.5$, especially at low energies, but less sensitive when $\dot{M}_{17}$ is below about 1.0. In fact at values of $\dot{M}_{17}$ above 1.5, it shows no signal at 0.5 keV, likewise there is no signal above $\dot{M}_{17} \sim 50$ for 1 keV. At higher energies, the total signal increases as $\dot{M}_{17}$ increases to a maximum then falls off after (the maximum at $\dot{M}_{17} \sim 5$ at 4 keV, and ~ 50 at 8 keV). Thus the increase in luminosity must dominate the absorption up to a point, that point depending on the energy. Since both luminosity and optical depth are directly proportional to $\dot{M}_{17}$, this effect is presumably a result of the complex geometry of the accreting region and curtain. It should also be pointed out that the model assumes a flat emission spectrum, which is sufficient for most purposes, but would affect this last result.

Figure 5.9 shows a selection of spin profiles with $\dot{M}_{17}$ varying.

The lack of signal at low energies for large $\dot{M}_{17}$ suggests that the cover is opaque to these energies at such accretion rates (optical depth varies directly as $\dot{M}_{17}$). Thus the choice of $\dot{M}_{17}$ of about unity, as per current theory, seems to fit reasonably well. It should be noted, however, that partial covering may also affect this, in that the lower N_H gaps would allow lower energy X-rays to be transmitted even with higher accretion rates.

5.2.8 Magnetic colatitudes, m_1 and m_2

The colatitudes can be varied in concert, so as to keep them symmetrical, or they can be varied independently.

Keeping the poles symmetrical

Putting $m_1 = 0°$ and $m_2 = 180°$, so putting the magnetic poles coincident with the spin pole, reduces the modulation to effectively zero. For $m_1 \gtrsim 1°$ (and $m_2 \lesssim 179°$) the spin

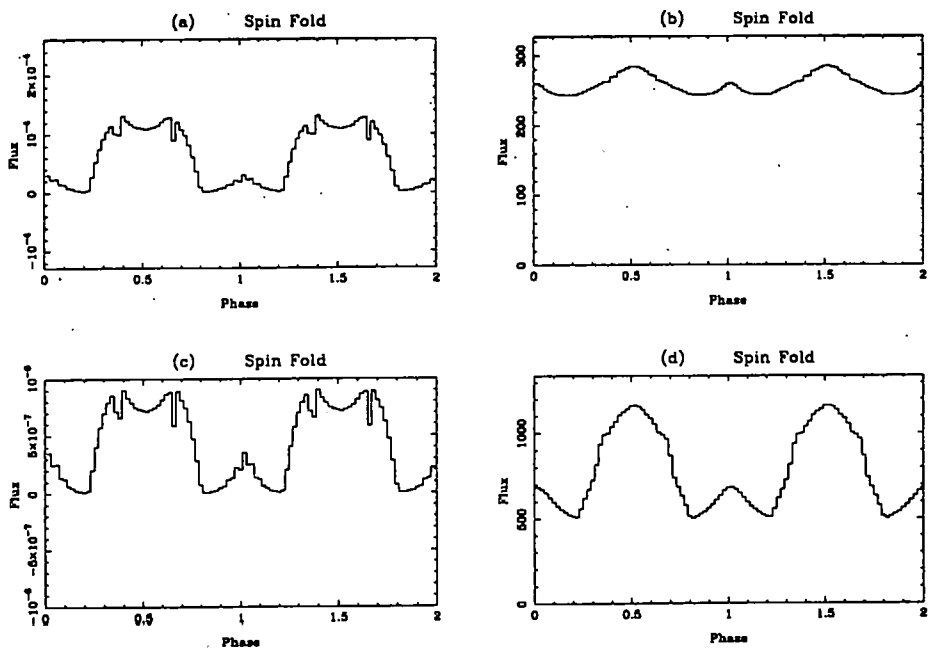

Figure 5.9: The first column shows reaction at low energies; both at $E = 0.5$ keV; the upper panel has $\dot{M}_{17} = 0.7$ and the lower has $\dot{M}_{17} = 1.0$. The right-hand column is at 4.0 keV and the upper panel has $\dot{M}_{17} = 0.5$, the lower panel has $\dot{M}_{17} = 5.0$.

profile is as in the base set, and varies little. At larger values ($m_1 \gtrsim 25°$ or $m_2 \lesssim 155°$) the central peak is reduced and the main peak is rounded off, but otherwise the broad features remain the same. As pointed out in Chapter 4, however, the use of arc-shaped geometry here is suspect. Figure 5.10 shows the effect of using the colatitudes 25° and 155°, one panel for disc-fed and one for stream-fed accretion.

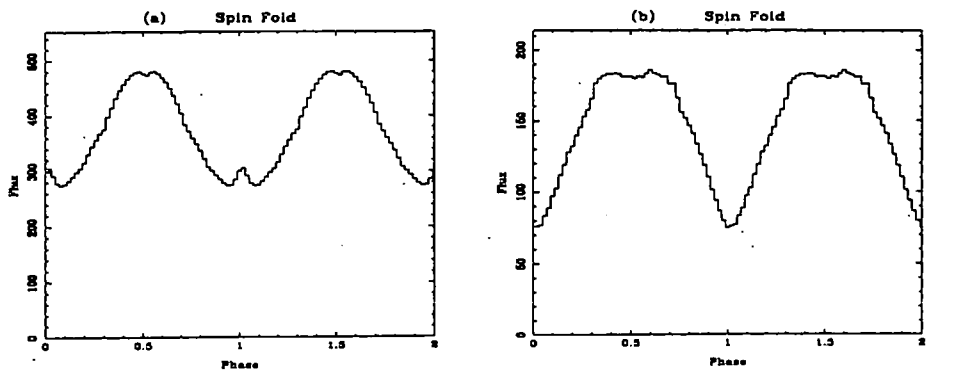

Figure 5.10: Spin profiles for $m_1 = 25°$ and $m_1 = 175°$. (a) has $\delta = 0.5$; (b) has $\delta = 1.0$.

Varying the poles independently

Varying m_1. Putting $m_1 = 0°$ and leaving $m_2 = 170°$ reduces the width of the peak in the spin profile. Here, the modulation is essentially caused by the intermittent appearance of the lower pole accretion region, the upper pole providing a constant flux.

Putting $m_1 \gtrsim 15°$ leads to increasingly irregular profiles. Figure 5.11 shows a selection of these.

The multiple peaks seen for $m_1 \gtrsim 15°$ are interpreted as being a result of the effect described in the section on inclination. The effect is to decrease β by only a small amount ($< 1°$) as m_1 goes from 10 to 15°, so the value $i + m_1 + \beta$ is increased, leading to occultation earlier in the spin cycle. Hence a dip occurs before the lower pole counteracts it.

Varying m_2. Putting the lower pole colatitude to 180° has the effect of reducing the period for which this pole becomes visible, so the result is a high-inclination observation of the

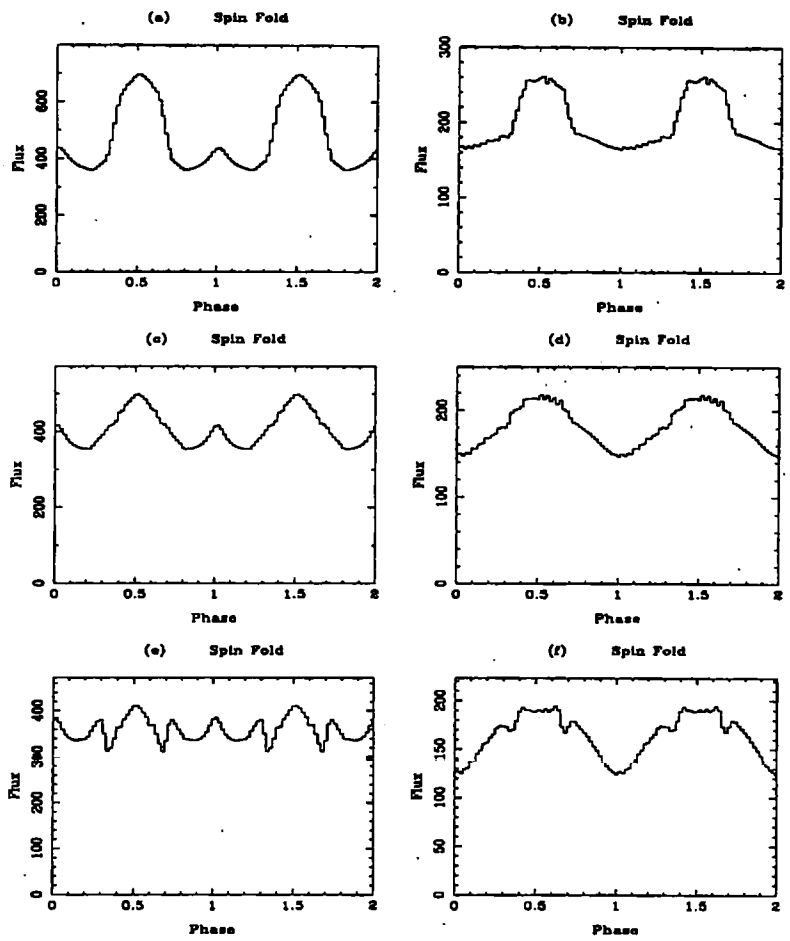

Figure 5.11: Variation of spin profile with upper pole magnetic colatitude. The left-hand column is for disc-fed only, the right-hand for stream-fed only. The upper row has $m_1 = 5°$; the middle row $m_1 = 10°$; and the bottom row $m_1 = 15°$. The lower pole is fixed at $m_2 = 170°$.

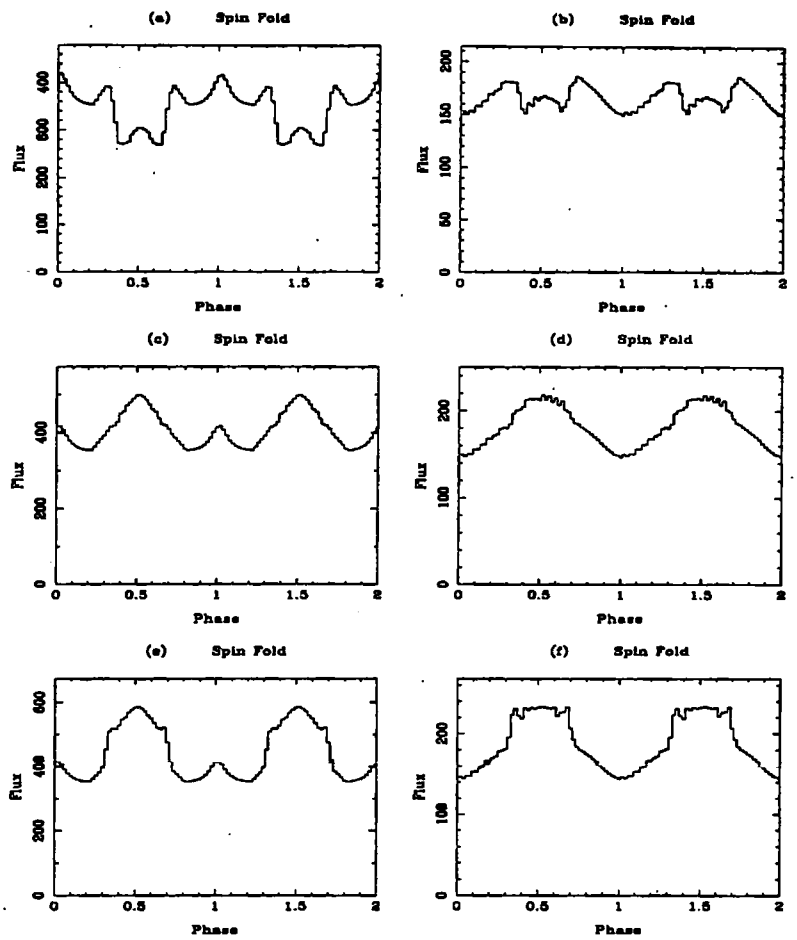

Figure 5.12: Variation of spin profile with lower pole magnetic colatitude. The left-hand column is for disc-fed only, the right-hand for stream-fed only. The upper row has $m_2 = 175°$; the middle row $m_2 = 65°$; and the bottom row $m_2 = 155°$. The upper pole is fixed at $m_1 = 10°$.

upper pole only, with the complications described above. This is borne out by allowing the colatitudes to increase but stay symmetrical, when the upper pole's dips are counteracted by the lower pole's appearance. Figure 5.12 shows variations in m_2. The irregular shape of the upper row is essentially due to the upper pole only, since at the inclination $i = 65°$ the lower pole at colatitude 175° is not seen. Hence the complications described in the discussion of i take effect. In the lower two rows, the lower pole becomes visible for a large part of the spin cycle. The fact that these irregular shapes are not seen suggests that large deviations from symmetrical colatitudes occur rarely, if the model is a good representation of the accretion geometry.

5.2.9 Azimuthal lag, γ

Altering the lag of the lower pole to be more or less than 180° away from the upper pole leads naturally to asymmetric spin profiles, unless the inclination is so small that the lower pole is never seen. Figure 5.13 shows an example of this, with power spectra, for different δ.

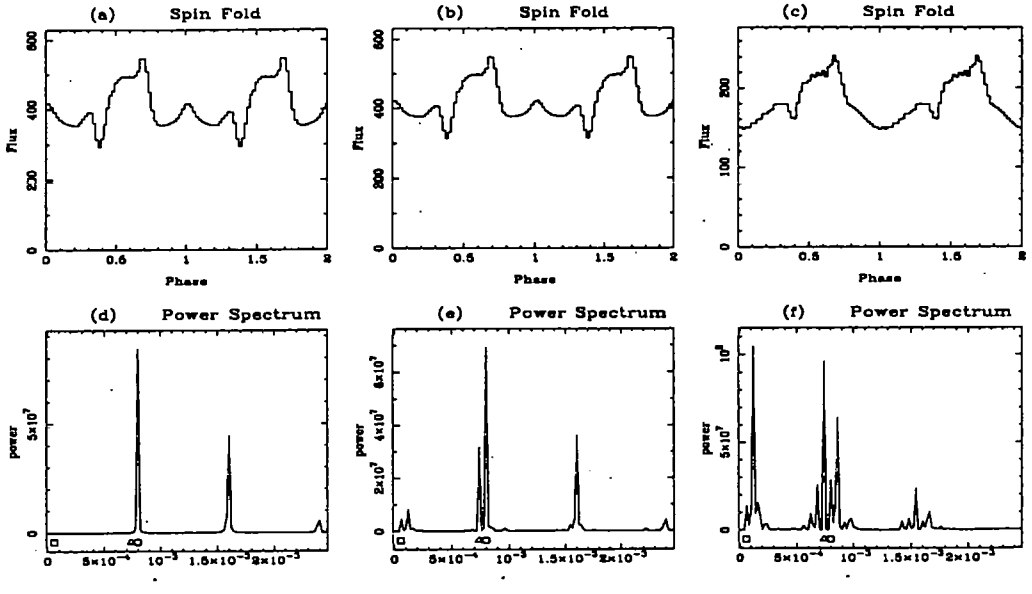

Figure 5.13: The upper row shows the effect of $\gamma = 200°$, with spin profiles for $\delta = 0.5$, $\delta = 0.6$ and $\delta = 1.0$ respectively. The lower row shows the corresponding power spectra.

The effect of azimuthal lag on the spin profile is explained as the result of the modulation

of the lower pole being out of phase with the upper pole.

5.2.10 Capture radii, $R_{mag}(1)$ and $R_{mag}(2)$

These were varied using disc-overflow, $\delta = 0.6$. The effect of varying them is small; keeping the difference constant and increasing both by the same amount has the effect of decreasing the magnitude slightly, while the spin folds retain the same shape.

Increasing $R_{mag}(1)$ and keeping $R_{mag}(2)$ constant results in a rounding off of the peaks and an increase in the total flux. The phase-zero peak is still present, at about the same relative depth of modulation. The parameter $R_{mag}(1)$ controls the inner edge of the accretion arc; increasing it reduces the distance of the inner edge from the magnetic pole, so increasing the width of the arc, that is f'.

Increasing both $R_{mag}(1)$ and $R_{mag}(2)$ so as to keep f' constant (and reduce the area of the accretion envelope, A) reduces the total flux, sharpens the peaks and troughs slightly, and increases the relative depth of the phase-zero peak.

5.2.11 Cell area and simulated run time, ΔA and $NTIME$

The area of each cell is determined by the run parameter ΔA, and the model is insensitive to this over a range 10^{-5} to 10^{-4} (in terms of the white dwarf surface area). This is not an intrinsic parameter, but it does help in reducing the run time. One caveat is that the width of the cell should be less than the width of the accretion arc, so care should be taken with the choice of $R_{mag}(q)$. Another non-intrinsic parameter is $NTIME$, which gives the length of the run. As long as this covers $\gtrsim 2$ orbital periods, the model is again insensitive to this.

5.3 Modulation depths

Here a series of tests is carried out in a range of energy windows, the modulation depth being estimated in each case. The program automatically outputs an estimate of the modulation depth, using the formula from Chapter 2 (equation 2.5). The spin pulse maxima and minima are taken after the spin profile phase bins are made up, so hopefully this process has averaged

out anomalous extremes. However, it may not be "correct" in the sense used in Chapter 3, where sinusoid fitting to real data was used.

The series consists of tests at different values of δ, and also with or without multiple column densities and partial covering.

Tables 5.2 and 5.3 show the modulation depths using various options, for two different inclination angles (thus the lower pole is visible in the first case, and always occulted in the second), with accretion rate $\dot{M}_{17} = 0.5$.

The 0.5 keV row may need some explaining. The flux as calculated by the program in these cases is very small, and shows as zero at the precision given, but the program calculates the modulation depth using the internal value. In some cases the maximum is small and non-zero. For example, for the first row in table 5.2 ($i = 65°$, $E = 0.5$ keV) for disc-fed only, full precision in the program would have given spin-max $= 0.18 \times 10^{-4}$, spin min $= 0.22 \times 10^{-13}$ giving modulation depth of approximately 1.00.

Figure 5.14 and 5.15 show the modulation depths in graphical form. Note that the partial covering cases show a maximum at $\sim$2 – 4 keV, consistent with the analysis in Chapter 2 (equation 2.12).

5.3.1 Full-covering models

The modulation depth decreases with increasing energy, for $E \gtrsim 2$ keV. The modulation depths for energies below this are unreliable, giving zero due to the opacity of the absorber. Consider the first test in table 5.2, at 0.5 keV, disc-fed only. With the parameters given, the optical depth due to electron scattering works out at 0.42, but that due to scattering plus photoelectric absorption works out at $\sim$ 2000 at this energy, so is opaque. Since modulations *are* seen at these energies, full covering with single column density does not fit the observations.

When the values for ΔN_H are calculated for the modulation depths in the full-covering model (based on equation 2.10), it is found that the values (in the disc-fed test) from 2.0 keV to 16.0 keV vary by a factor of 2 (from 94 to 199), and from 4.0 keV to 16.0 keV ΔN_H varies from 150 to 199. If this is compared to real data, for example the Ginga results for AO Psc from Chapter 3, we find that modulation depth 0.56 in the 1.7 – 4.1 keV band would

Table 5.2: Spin pulse maxima and minima, and modulation depths; $i = 65°$

	.....Disc-fed.....			.....Stream-fed.....			.....$\delta = 0.65$.....		
E/keV	spin max	spin min	mod depth	spin max	spin min	mod depth	spin max	spin min	mod depth
0.50	0.00	0.00	1.00	0.00	0.00	0.00	0.01	0.00	1.00
1.00	13.51	1.76	0.87	0.06	0.01	0.86	15.91	3.27	0.79
2.00	141.43	58.77	0.58	23.37	13.17	0.44	138.17	71.84	0.48
4.00	284.79	236.17	0.17	217.55	146.66	0.33	280.52	240.88	0.14
8.00	319.60	306.29	0.04	292.82	261.92	0.10	321.70	306.86	0.05
16.00	324.45	316.67	0.02	316.25	290.16	0.08	327.80	317.22	0.03
0.50	135.02	126.35	0.06	146.11	126.66	0.13	136.22	129.28	0.05
1.00	144.48	129.62	0.10	142.95	124.75	0.13	145.43	131.65	0.10
2.00	216.86	165.82	0.23	160.11	134.97	0.16	217.69	173.46	0.20
4.00	303.10	273.16	0.10	243.61	210.37	0.14	302.13	274.84	0.09
8.00	323.70	315.58	0.03	313.39	287.98	0.08	326.97	315.88	0.03
16.00	327.22	320.62	0.02	328.00	304.39	0.07	330.67	321.70	0.03
0.50	0.33	0.03	0.91	0.00	0.00	0.91	0.47	0.06	0.87
1.00	11.08	2.72	0.75	0.73	0.37	0.49	12.46	3.91	0.69
2.00	112.51	42.41	0.62	18.08	11.27	0.38	115.52	51.13	0.56
4.00	408.72	244.13	0.40	152.14	101.32	0.33	399.89	262.73	0.34
8.00	617.32	507.32	0.18	417.16	309.72	0.26	606.57	517.99	0.15
16.00	657.10	575.23	0.12	516.42	411.68	0.20	327.80	317.22	0.03
0.50	297.82	268.78	0.10	317.78	251.53	0.21	298.94	268.23	0.10
1.00	303.61	276.14	0.09	320.57	266.03	0.17	308.16	272.66	0.12
2.00	355.23	304.56	0.14	325.73	267.27	0.18	366.09	301.77	0.18
4.00	530.99	419.55	0.21	400.82	323.22	0.19	538.46	432.14	0.20
8.00	658.66	574.40	0.13	554.12	459.88	0.17	651.91	580.75	0.11
16.00	679.55	630.16	0.07	625.97	504.08	0.20	692.39	623.93	0.10

Notes:

Block 1: full covering, single column density;

Block 2: partial covering (cov = 0.6), single column density;

Block 3: full covering, multiple column density;

Block 4: partial covering (cov = 0.6), multiple column density;

Table 5.3: Spin pulse maxima and minima, and modulation depths; $i = 30°$

	.....Disc-fed.....			.....Stream-fed.....			.....$\delta = 0.65$.....		
E/keV	spin max	spin min	mod depth	spin max	spin min	mod depth	spin max	spin min	mod depth
0.50	0.00	0.00	1.00	0.00	0.00	0.00	0.00	0.00	1.00
1.00	6.35	0.10	0.98	0.00	0.00	0.97	8.04	0.32	0.96
2.00	107.55	11.94	0.89	7.04	3.69	0.48	102.80	19.33	0.81
4.00	269.61	119.34	0.56	111.91	65.09	0.42	255.91	139.92	0.45
8.00	315.62	258.13	0.18	246.73	179.63	0.27	309.79	260.87	0.16
16.00	322.23	289.17	0.10	279.48	227.01	0.19	318.30	289.90	0.09
0.50	134.99	128.28	0.05	141.05	117.97	0.16	136.20	127.50	0.06
1.00	139.15	129.03	0.07	141.83	123.14	0.13	139.44	130.46	0.06
2.00	196.26	138.36	0.29	146.58	128.07	0.13	193.60	143.77	0.26
4.00	294.14	202.96	0.31	198.91	168.71	0.15	284.07	215.81	0.24
8.00	321.44	286.77	0.11	278.99	241.37	0.14	317.16	289.01	0.09
16.00	325.32	305.27	0.06	298.87	264.02	0.12	322.62	305.84	0.05
0.50	0.14	0.00	0.99	0.00	0.00	0.99	0.20	0.01	0.97
1.00	6.67	0.44	0.94	0.17	0.07	0.62	7.31	0.81	0.89
2.00	78.12	10.53	0.86	7.62	4.21	0.45	78.11	15.14	0.81
4.00	345.75	90.68	0.74	79.98	46.72	0.42	327.53	113.47	0.65
8.00	581.09	296.27	0.49	277.83	184.29	0.34	551.06	326.59	0.41
16.00	647.87	410.14	0.37	391.42	267.32	0.32	318.30	289.90	0.09
0.50	297.76	262.24	0.12	330.20	256.35	0.22	296.98	268.98	0.09
1.00	298.81	268.44	0.10	338.31	254.59	0.25	295.48	273.40	0.07
2.00	336.24	279.99	0.17	319.99	238.73	0.25	350.75	278.65	0.20
4.00	493.80	337.72	0.32	360.56	289.20	0.20	479.19	342.88	0.28
8.00	640.79	451.57	0.29	472.99	382.14	0.19	621.22	480.17	0.23
16.00	675.88	526.08	0.22	538.43	436.57	0.19	653.54	536.64	0.18

Notes:

Block 1: full covering, single column density;

Block 2: partial covering (cov = 0.6), single column density;

Block 3: full covering, multiple column density;

Block 4: partial covering (cov = 0.6), multiple column density;

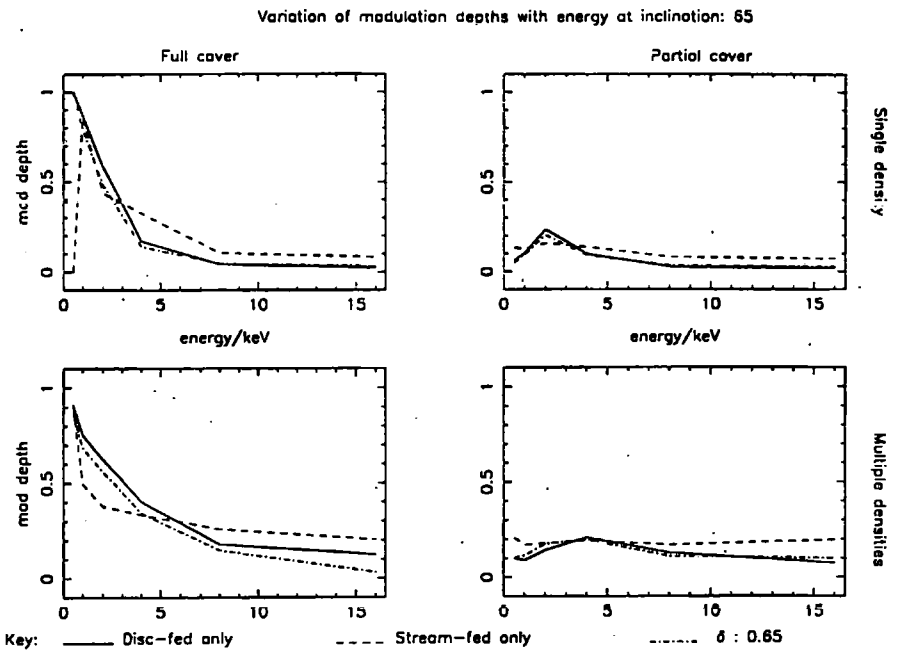

Figure 5.14: Modulation depths from Table 5.2.

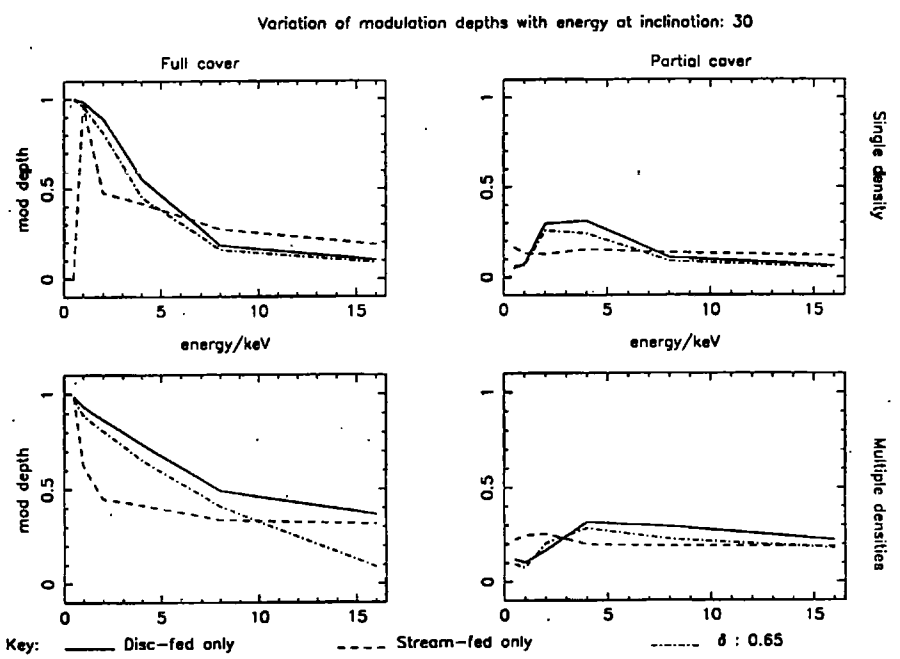

Figure 5.15: Modulation depths from Table 5.3.

have a theoretical ΔN_H of about 1.6 $\times 10^{24}$ cm $^{-2}$, and in the 9.8 – 18.6 keV band would have a ΔN_H of about 9.5 $\times 10^{24}$ cm $^{-2}$, a difference of a factor of ~ 6.

5.3.2 Partial covering & multiple densities

When the option to have partial covering is used, the effect at low energies is highly unpredictable. For a parameter close to 1.0 ($\gtrsim 0.99$) the modulation depth comes out at 100 percent. At higher energies, the results suggest that the effect of absorption is reduced.

5.3.3 Interpretation

The results at lower energies are explained in the model by considering that at most timesteps the signal is zero, due to complete absorption, interspersed with occasional unabsorbed signals. This effect lessens as COV is reduced, since it is less likely that a spin profile phase bin will have zero content.

In Chapters 2 and 3 there was some discussion of the modulation depth at different energies, with the conclusion that a single value of ΔN_H could not explain the data observed (both here and previous observations) hence partial covering/ multiple column density models have been proposed. When the formula from Chapter 2 relating modulation depth to ΔN_H is applied to the values in the tables above, it is found that there is a broad agreement in the full cover, single column density runs, especially in the disc-fed runs, at the higher energies ($\gtrsim 4$ keV). For example, using the first block of data in table 5.2, the modulation depths 0.17, 0.04, and 0.02 at 4.0, 8.0 and 16.0 keV respectively lead to estimates of ΔN_H of 220, 245 and 232 ($\times 10^{22}$ cm^{-2}). Such close estimates are not seen in the multiple density tests, thus agreeing with conclusions of the interpretations of observational data.

As stated in Chapter 4, the assumptions on the parameters of the Gaussian distribution used in the multiple densities case are arbitrary and fixed. The program should be enhanced to allow the researcher to vary these, thus to test the sensitivity of the model to them.

5.4 "Fitting" to IPs

The ultimate aim of this modelling is of course to find fits to various intermediate polars. Here we consider some of the problems in this.

5.4.1 Symmetric spin profiles

As the results above indicate, sinusoids and quasi-sinusoids can be produced by several combinations of parameters. One problem with fitting these is that such curves often lack features which could help constrain the parameters required, meaning that other clues need to be considered (for example orbital effects constraining the inclination).

Double-peaked systems offer a possibility of study, however these are rare in the X-ray band.

In view of this, it may be better to try to fit the less regular profiles.

5.4.2 FO Aqr

The frequently studied FO Aqr is an ideal candidate for fitting, since it exhibits an asymmetrical spin profile and secular changes in the profile and power spectrum. Thus if a set of parameters was found to fit the profile at a particular epoch, and plausible variations in parameters then fit it at other epochs, some conclusions about the system could be made.

Firstly, consider which parameters would be expected to be permanent (over timescales of decades). These would include the spin and orbital period, i, m_1 and m_2, M_* (and consequently R_*), and γ. Parameters which could plausibly change are $\dot{M}_{17}$, $R_{mag}(q)$ (which may depend on $\dot{M}_{17}$), COV, which would depend on the clumpiness of the accretion curtain, δ (which again may depend on $\dot{M}_{17}$), and the extent of the accretion arcs (f''). The 1990 observation shows no evidence of a beat period in the power spectrum, whilst the others do show a small beat effect, plus an orbital signal. We may assume from this that δ can also undergo changes, although the small power of the beat suggests that the parameter is close to 0.5, with mainly disc accretion.

So far testing has not produced a good fit with FO Aqr, however broad features of the spin profiles at certain epochs can be obtained. Figure 5.16 reproduces two of the spin profiles

extracted from figure 2.6, and considering these as a sample, it is evident that one feature common to most is the sharp rise to the maximum, followed by a slower decline , which may then produce a subsidiary peak. In October 1988 the decline is steepest at lower energies, also the depth of the dips. In May 1993 (figure 2.6) the first minimum has almost disappeared, giving a "shoulder" prior to the dip to the minimum. These two observations have a beat signal in common, suggesting a significant stream-fed contribution. The observation from June 1990 has no beat signal, which suggests that the accretion at this time was almost 100% through the disc. However, similar features to the others are still seen, with the steep rise and double peaks/ troughs. The peak in this case has a slightly flattened top, though. It may also be noted that the relative depths of the troughs has exchanged, although given the scarcity of datasets to compare it is difficult to determine whether this is a consequence of the different accretion modes or simply incidental.

Another point, although not shown here, an observation from October 1983 (Beardmore at al, 1997) shows the spin profile as being symmetrical, with little evidence for the dip preceding the maximum. If the assumption of asymmetry being caused by the offset dipole is correct, this means that it is possible for the lower pole to be not visible at times. If it assumed that m_2 cannot change over short timescales, this must be caused by either the area of the accretion envelope decreasing (hence $R_{mag}(2)$ increasing), or an eclipse of the lower pole, possibly by the inner edge of the disc. This is not yet a factor in the model.

The testing so far has succeeded in reproducing some of the features, but has yet to reproduce them all. For instance, figure 5.17(a) and (b) look rather similar to the 1988 and 1990 data respectively. However, one has $\gamma = 220°$ whilst the other has $\gamma = 160°$, and clearly γ is unlikely to vary between these epochs.

More plausible variations in parameter, such as those shown in figure 5.18 are not as convincing as figure 5.17 but are nonetheless consistent and show the expected signals in the power spectra.

The power spectrum does not quite match the ones seen in Beardmore et al, in that the beat signal is of similar magnitude to the orbital spike, in the disc-overflow run. However, the system does have orbital effects independent of the beat, and these have not been included for this test.

The panels do show the asymmetry which is evident in the data. The phase zero is at the

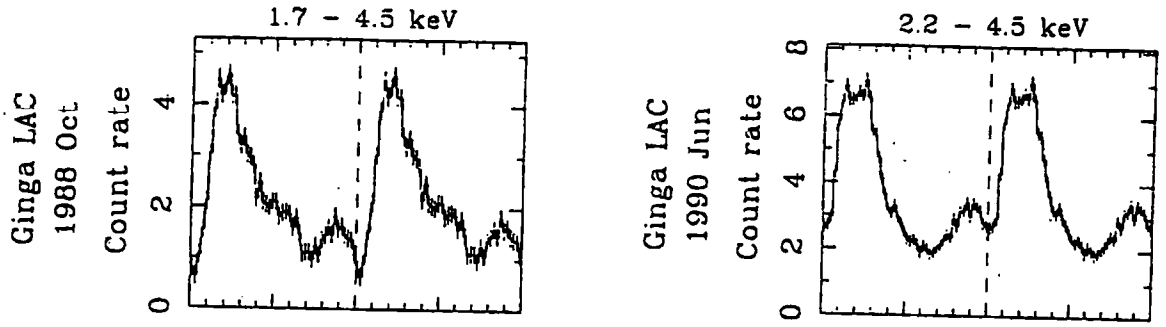

Figure 5.16: Spin profiles of FO Aqr. The left-hand panel is from the Oct 1988 *Ginga* observation, and the right-hand is from the June 1990 *Ginga* observation. (From Beardmore et al, 1997.)

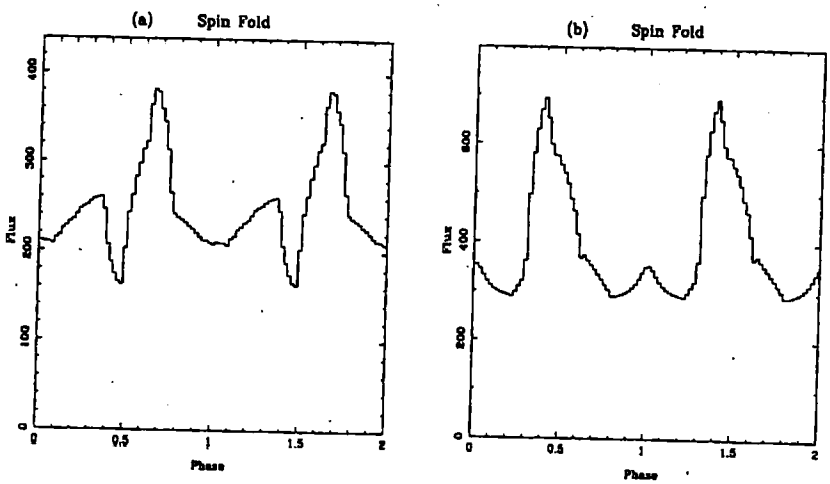

Figure 5.17: Two possible fits to the 1988 and 1990 data for FO Aqr. The left-hand panel has $m_1 = 15°$, $m_2 = 115°$, $\gamma = 220°$ and $\delta = 0.9$. The right-hand panel has $m_1 = 15°$, $m_2 = 160°$, $\gamma = 160°$ and $\delta = 0.5$. Energy is 4 keV in both cases.

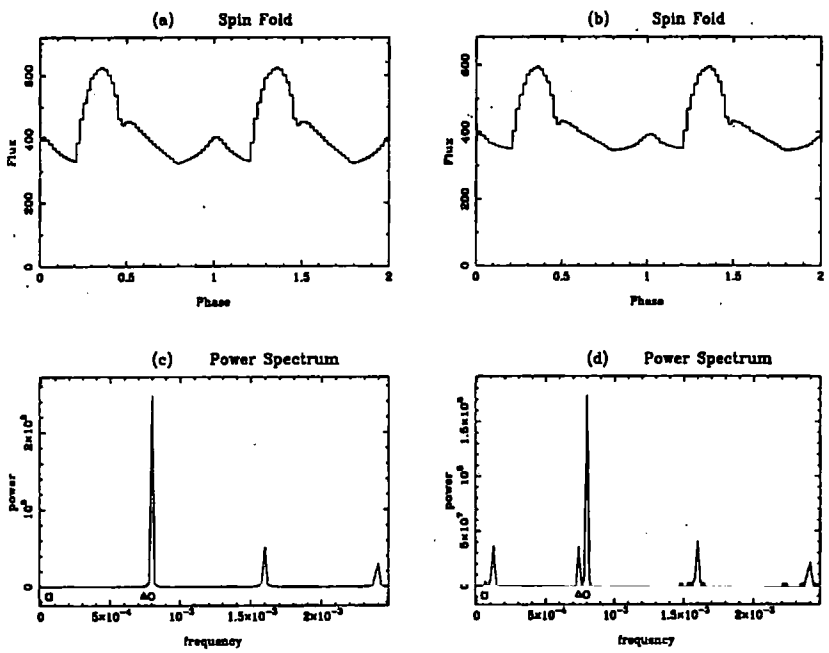

Figure 5.18: Simulated spin profiles to recreate the broad features of FO Aqr. The left-hand column has $m_1 = 7°$, $m_2 = 170°$, $R_{mag}(1) = 19$, $R_{mag}(2) = 14$ and $\delta = 0.5$. The right-hand column has $m_1 = 5°$, $m_2 = 170°$, $R_{mag}(1) = 11$ and $R_{mag}(2) = 8$ and $\delta = 0.65$. $\gamma = 116°$ for both tests, and energy = 4keV.

small peak, rather than the dip preceding the maximum, as assumed in the observational data. Also the small peak occurs at phase 0.6 – 0.7 after the maximum, so is in the expected place. The maximum in the 1990 observation has a flattish top, which hasn't been simulated effectively here. As far as the relative depths of the troughs, the simulation shows no real evidence of any dependence on accretion mode.

In summary the results presented in this section show a possible way forward in modelling the emission from FO Aqr, however a formal fit to the data awaits development to the model, which we discuss in Chapter 6.

5.5 Orbital profiles

The pulse profile at the orbital period can have a variety of shapes, and is dependent on parameters such as δ, and the orbital N_H values. So with disc-fed only accretion, no orbital modulation is seen, unless the ORBN_H parameters are set non-zero. With stream-fed accretion or disc-overflow, the signal at the beat period interacts with the spin signal, producing an orbital modulation, as well as a beat signal (see Norton et al, 1996).

Using the ORB$N_H$parameters, with a sinusoidal component and/or a dip, the modulation at the orbital periods becomes obvious, as is to be expected.

Figure 5.19 shows the effect of introducing these parameters into a disc-fed run. These are thought to be the types of effect seen in AO Psc and V1223 Sgr. Thus the first column shows the light curve, the second column the orbital profile and the third the power spectrum. The rows are: (top) with sinusoidal component of orbital modulation; (middle) orbital dip; and (bottom) both effects present.

The effects on the power spectra are discussed in section 5.6.

5.6 Power spectra

The types of power spectra are considered here, and compared with predictions from theory. Figure 5.20 shows a series of power spectra with δ varying from 0.5 (disc-fed only) to 1.0 (stream-fed). (Assumption: no absorption varying with the orbital period.)

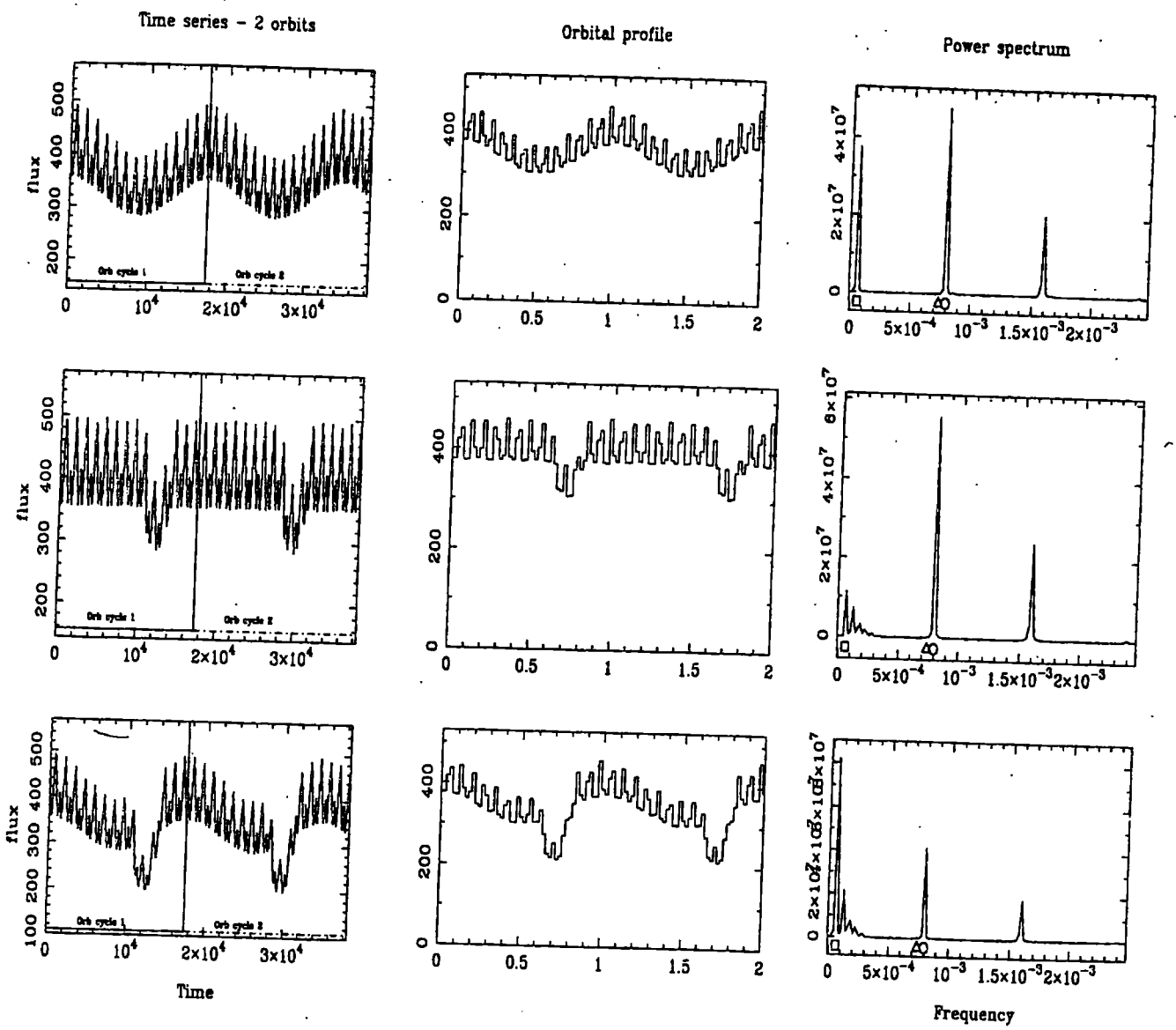

Figure 5.19: The effects of including orbital absorbers. Upper row: sinusoidal absorber; middle row: dip at phase 0.75; lower row: both effects.

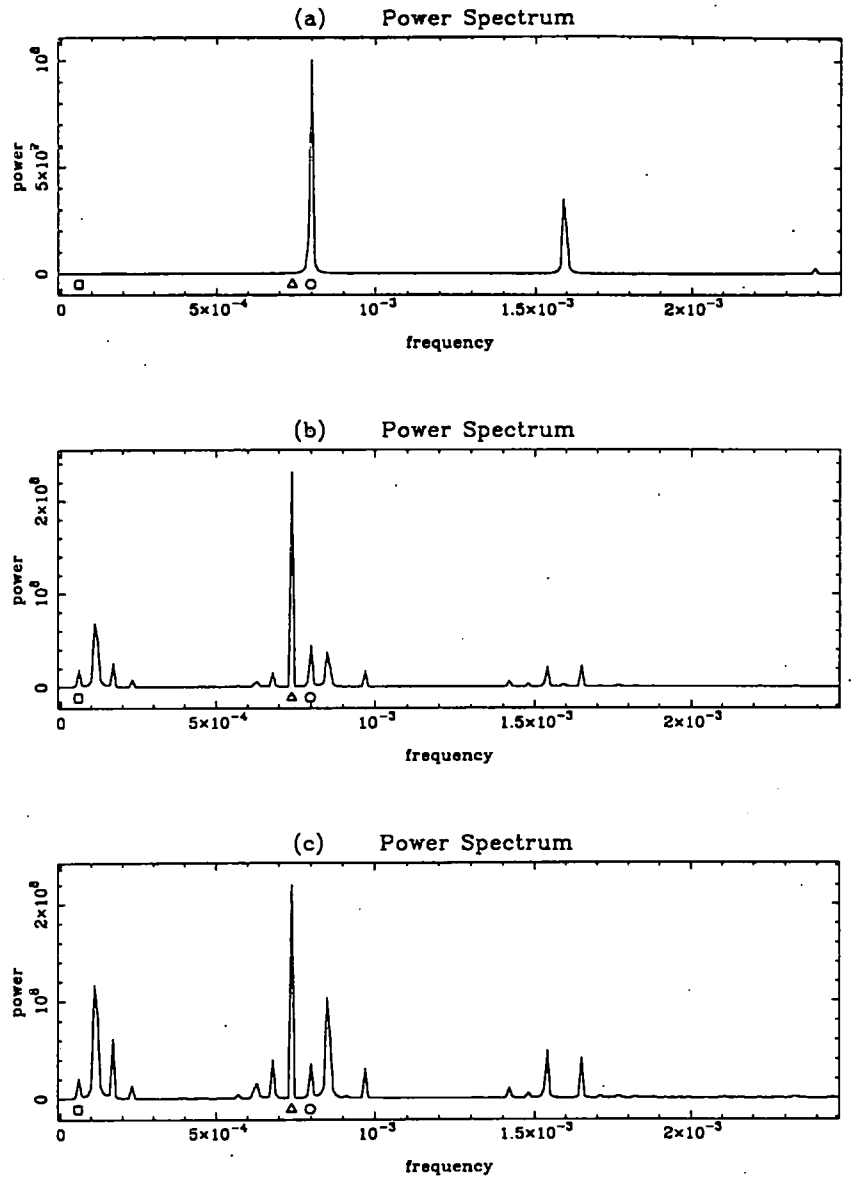

Figure 5.20: Power spectra from the parameter set in table 5.1. These correspond to the first three spin profiles in figure 5.5. Panel (a) has $\delta = 0.5$ (disc-fed only), (b) has $\delta = 0.8$ (disc-overflow), (c) has $\delta = 1.0$ (stream-fed). All use sinusoidal weighting for stream distribution.

5.6.1 Disc-fed, no orbital absorption

Looking at figure 5.20(a), these are found to exhibit signals at the spin frequency, and its harmonics, but show no evidence of any signal at the beat frequency, when the ORBN_H parameters are zero. The frequencies are denoted by the symbols: circle (spin), square (orbital), and triangle (beat).

5.6.2 Disc-fed with orbital modulation

When the ORBN_H parameters are non-zero, in other words an orbitally-fixed absorber is assumed, the power spectrum does show orbital effects, as seen in figure 5.19 (final column). As is apparent, the presence of a sinusoidal component gives a signal at the orbital period. Harmonics are not present here. With the non-sinusoidal dip (similar to V1223 Sgr) the orbital signal is present, with harmonics.

5.6.3 Disc-overflow

Varying δ leads to a progressive increase in the strength of the beat signal relative to the spin frequency signal. In fact at $\delta \approx 0.6$, corresponding to $\sim 80\%$ disc-fed accretion, the beat signal is about the same strength as the spin signal. The orbital second harmonic exceeds the spin signal at about $\delta = 0.8$, that is $\sim 60\%$ stream-fed accretion.

In the case of the sharper variation of stream to each pole, the spin period dominates up to about $\delta = 0.9$.

5.6.4 Stream-fed

Again, looking at figure 5.20(c), the power spectrum for stream-fed accretion shows strong signals at the beat frequency, as well as at the spin frequency. In this case the beat signal dominates, with strong signals also seen at the positive sideband (spin+orb). The first harmonic of the orbital frequency is strong, and the spin frequency signal is present but highly reduced.

Figure 5.21 shows power spectra for $\delta = 1.0$, this time with the stream varying more sharply

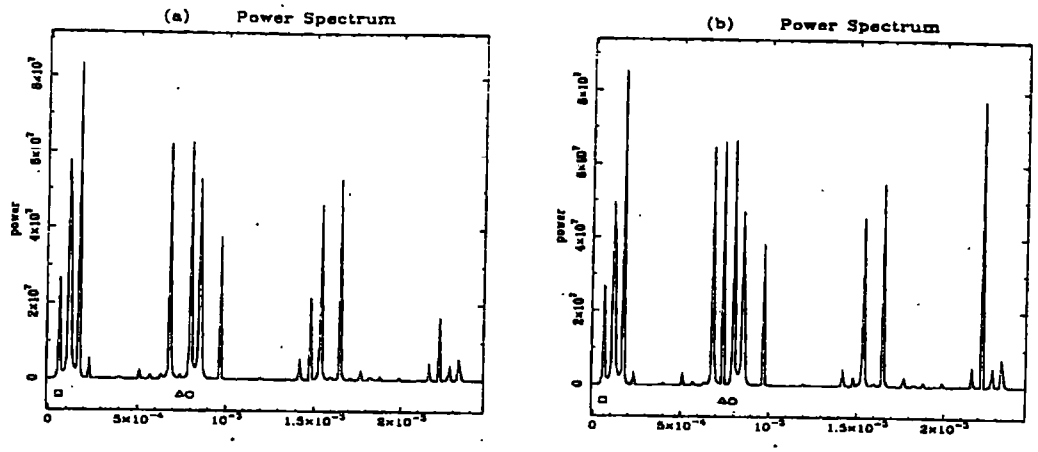

Figure 5.21: Power spectra for stream-fed accretion showing the difference between $\cos^{0.1}\psi$ and 100% flip weighting; although there is little discernible difference in the spin profile, these show a difference in the beat signal.

with the stream-field incident angle, using $\cos^{0.1}$ weighting in 5.21(a), and 100% flip in 5.21(b). The beat signal is surprisingly almost absent in 5.21(a), an effect not seen in 5.21(b). Whether this is an effect of choosing a power of the cosine function is difficult to say; the function is chosen arbitrarily in any case. In both these cases the spin signal is relatively strong, and the harmonics of the orbital period are also well evident.

5.7 Discussion

The model can be said to be partially successful, in that it produces many of the effects seen in intermediate polars, with the modelling based on what is assumed about the physics of the accretion process. It naturally produces a general decrease in modulation depths with increasing energy, which is built into its calculation of the photoelectric absorption. It can produce orbital effects, although these are somewhat artificial, being introduced ad hoc to fit particular systems, rather than being an outcome of the main physical part of the model. That being said, it should be expected that these effects would constrain the inclination.

A few intermediate polars exhibit double peaks in their spin profiles, for example PQ Gem, GK Per (in quiescence) and XY Ari. The latter has been observed to exhibit orbital and

spin periods, but no others, suggesting predominantly disc-fed accretion, and its inclination is estimated from eclipse data to be in the range $80° < i < 87°$ (Allan et al, 1996). This puts it in the class where the model predicts double peaks. GK Per also appears to have a disc-fed accretion mode, and inclination $46° < i < 73°$ (Reinsch, 1994). Again it would appear to be a good candidate for double peaks using our model.

An estimate of the numbers of intermediate polars at various inclinations from a statistical analysis would lead us to expect the distribution to be proportional to $\sin i$ (see for example King & Shaviv, 1984). Since the testing shows the double peak for $i \gtrsim 40°$, we should expect to see this in about $\int_{0.2\pi}^{0.5\pi} \sin i di$ of disc-fed systems. This works out at ~ 0.75 of cases.

Weaknesses, as mentioned earlier, are that simulations of symmetrical profiles really need extra information, as more than one set of parameters can often produce similar results. All in all, however, the model can be used to check whether suspected parameters sets do model systems under study. Future developments of the model are discussed in the next chapter.

Chapter 6

Summary and conclusions

The major part of this project is described in Chapters 4 and 5. This last chapter gives a brief review of the work, and suggestions for possible directions to take it further.

6.1 Key points about the simulation

The model as designed is flexible, in that it should allow ease of enhancements in the light of current and future theory. The development of the extra work on the accretion geometry, in particular the more involved calculation of optical depth in various directions, has taken the original groundwork, from such as Fabian, Pringle and Rees, further along the path to a more complete solution. The production of double peaks in the spin profiles of high inclination disc-fed systems is a natural result of this approach. The model produces many of the features seen in actual systems, from the basic light curve to the various profiles. The program itself does not produce power spectra, but these are easily producible using suitable software. The resulting power spectra are found to relate well to those seen in nature, and the source of these features, mainly spin, orbital and beat effects, support the ideas put forward to explain them when observed. The data also lend themselves to analysis similar to that done in practice, for instance in relating modulation depths and energy.

Weaknesses in the program include the large number of free parameters it currently has, so that apart from the problem of searching parameter space it can lead to multiple solutions to

the same problem (as the various parameter sets which produce sinusoidal or quasi-sinusoidal profiles).. Also the calculation of the accretion geometry as it stands assumes an arc with sharp edges and corners, which is perhaps somewhat unrealistic, and may lead to rather spikier profiles than would be seen in real life.

6.2 Comparison with other computer simulations

There have been other attempts to model these systems, a recent one being Kim & Beuermann (1995). Their model is complementary to ours; the magnetospheric radius is calculated using assumptions about accretion rate and magnetic field moment. Their process for splitting accretion between the upper and lower poles is similar to ours, and depends on the cosine of the angle between field line and gravity vector. The direction of the stream overflow is not taken into consideration – the model mainly assumes attachment from the inner disc edge. They have also included the emission spectrum, which is not yet a component of our model, and have allowed for clumpiness in the material. On the other hand, no allowance is made for offset dipoles, and the absorption in the accretion column is taken to be a function of azimuth only, so their light curves are generally simple, exhibiting symmetry, and a single peak.

6.3 Further work

As mentioned above, the model is flexible enough for enhancements to be applied. One such could be to amend it so as to round off the corners of the accretion region, as in reality it is highly unlikely that these would be as sharply defined as assumed here. As part of this, or independently, it may also be considered that the accretion curtain is itself not of the same density throughout (the Kim & Beuermann model assumes that the ends of the arc are less dense than the central part). It may be, for instance, that the thickness of the material is unbalanced, and increases as we go from one end to the other. This may help simulate the slight asymmetry between the rise to and fall from the maximum in some spin profiles (shown in Chapters 1 and 2), which seem to be qualitatively different from the more complex asymmetric profiles such as FO Aqr. If this amendment to the accretion curtain thickness does occur, this would complicate the absorption calculation somewhat, although

the brightness of the accreting cells should be easy to obtain. It would also seem that it ought to be parameterised, perhaps giving the relative distance along the arc where the maximum is, and using a suitable function to obtain the brightness of an individual cell.

At high inclinations, the inner edge of the disc may be close enough in to eclipse (totally or partially) the lower pole. This may be included in the model; the calculation depends on the white dwarf radius, the inner disc radius, and the positions of the lower pole cells in the observer's frame, all of which are currently in the model. This would affect the signal at the spin period. A more difficult calculation may be for that alluded to briefly in the studies of V1223 Sgr in Chapter 3: the possibility of an orbitally fixed absorber at the inner edge, as a result of the stream overflowing the disc. This would (at certain inclinations) act to eclipse (or reduce) the X-ray signal from the lower pole. The eclipse would occur at the spin period, but would only occur at orbital phases close to 0.5 (as defined in our model), when the thrown-up material is in the line of sight to the lower pole.

At the moment the accretion rate and capture radii are treated independently, but it should be more convenient to correlate these, with regard to the magnetic moment. As far as the outer capture radius is concerned, we would be replacing one parameter by another, but the inner capture radius could then be assumed to have a relation such as that given in Hameury, King and Lasota (1986). An advantage of this approach would be that if in future it was decided that the stream-fed accreting material attached at different radii (due to having a ram pressure different from the disc material) this could then be incorporated without requiring extra parameters.

The use of the covering fraction and multiple column densities in the model may also need some rethinking. At the moment it is assumed that a particular cell is either covered or uncovered, the decision being made using a random number generator and comparing it with the covering fraction, with the uncovered portion assumed to have optical depth zero (or the interstellar value). The algorithm for multiple column densities works independently, and again uses a randomiser to calculate the density as a gaussian spread about the average. These should really be correlated, probably with the theories of clumpy accretion. This is brought to light in the test at low energies with the covering fraction of $\gtrsim 0.99$, when a distribution of optical depths (rather than simply transparent or opaque) may result in more sensible results.

The model currently assumes a flat emission spectrum. Since its use has largely been to

simulate light curves, this is peripheral. However, it could be modified to produce a more realistic spectrum. Along with this, it should be noted that it assumes an exact energy "window", whereas X-ray telescopes in general are less precise. A possible amendment may be to take the average of (say) four energies within a band (weighted according to the detector response), to get a picture more in line with an observation. The modulation depth could very well differ when a range is taken into account.

Finally, we should give thought to inverting the model so rather than testing parameter sets, take a system as a target, and attempt to fit it, possibly using a genetic algorithm. For this it would require a quantitative fitting procedure to real data of course. The latter could be done on a χ^2 basis, or perhaps by comparing power spectra.

As more intermediate polars are discovered, it is hoped that this model will provide the basis for a more quantitative insight into their nature.

Bibliography

[1] Allan A, Horne K., Hellier C., Mukai K., Barwig H., Bennie P. J., Hilditch R. W., 1996, Mon. Not. R. Astr. Soc.,**279**, 1345

[2] Armitage P.J., Livio M., 1996, Astrophys. J., **470**, 1024

[3] Beardmore A. P., Mukai K., Norton A. J., Osborne J. P., 1997 Mon. Not. R. Astr. Soc., (submitted)

[4] Bevington P.R., Robinson D.K., 1992, Data reduction and error analysis for the physical sciences. McGraw-Hill Inc.

[5] Buckley D.A.H., Tuohy I. R., 1989, Astrophys. J., **344**, 376B

[6] Buckley D.A.H., Sekiguchi K., Motch C., O'Donoghue D., Chen A.-L., Schwarzenberg-Czerny A., Pietsch W., Harrop-Allin M.K., 1995, Mon. Not. R. Astr. Soc.,**275**, 1028

[7] Córdova F. A., 1993, (Cataclysmic variable stars), in X-Ray Binaries, Eds: W. H. G. Lewin, J. van Paradijs, and E. P. J. van den Heuvel; Pubs: Cambridge University Press

[8] Córdova F. A., Mason K. O., Nelson J. E., 1981, Astrophys. J., **245**, 609

[9] De Martino D., Buckley D. A. H., Mouchet M., Mukai K., 1994, Astronomy & Astrophysics **284**, 125

[10] De Martino D., Mouchet M., Bonnet-Bidaud J. M., Vio R., Rosen S. R., Mukai K., Augusteijn T., Garlick M. A., 1995, Astronomy & Astrophysics **298**, 849

[11] Fabian A. C., Pringle J. E., Rees M. J., 1976, Mon. Not. R. Astr. Soc.,**175**, 43

[12] Frank J., King A. R., Lasota J. -P., 1988, Astronomy & Astrophysics **193**, 113

[13] Frank J., King A. R., Raine D. J., 1992, Accretion Power in Astrophysics, second edition, Cambridge University Press

[14] Gilliland R. L., 1982, Astrophys. J., **258**, 576

[15] Hameury J. M., King A. R., Lasota J. -P., 1986, Mon. Not. R. Astr. Soc., **218**, 695

[16] Hameury J. M., King A. R., Lasota J. -P., Ritter H., 1987, Astrophys. J., **316**, 275

[17] Hameury J. M., King A. R., Lasota J. -P., 1989, Mon. Not. R. Astr. Soc., **237**, 39

[18] Hayashida K. Inoue H., Koyama K., Awaki H., Takano S., 1989 Publications. of the Astr. Soc. of Japan, **41**, 373

[19] Hellier C., 1991, Mon. Not. R. Astr. Soc., **251**, 693

[20] Hellier C., 1997, Advances in Space Research (in press)

[21] Hellier C., Mason K., O., Cropper M, 1989, Mon. Not. R. Astr. Soc., **237**, L39p

[22] Hellier C., Mason K., O., Mittaz J. P. D., 1991, Mon. Not. R. Astr. Soc., **248**, P...5H

[23] Hellier C., Cropper M, Mason K., O., 1991, Mon. Not. R. Astr. Soc., **248**, 233H

[24] Hellier C., Garlick M., Mason K., O., 1993, Mon. Not. R. Astr. Soc., **260**, 299H

[25] Hellier C., Ramseyer T. F., 1994, Mon. Not. R. Astr. Soc., **271**, L..25H

[26] Hellier C., Mukai K., Ishida M., Fujimoto R., Mon. Not. R. Astr. Soc., **280**, 877

[27] Ishida M.., 1991, X-ray Observations of Accreting Magnetic White Dwarfs, 1991, Thesis

[28] Jablonski F, Steiner J.E., 1987, Astrophys. J., **323**, L672

[29] Kaluzny J., Semeniuk I., 1988, Inf. Bull. Var. Stars, 3145

[30] Kamata Y., Tawara Y., Koyama K., 1991, ApJ 379, L65-L68. Astrophys. J., **379**, L65

[31] Kim Y., Beuermann K., 1995, Astronomy & Astrophysics **298**, 165

[32] King A. R., 1993, Mon. Not. R. Astr. Soc., **261**, 144

[33] King A. R., Shaviv G., 1984, Mon. Not. R. Astr. Soc., **211**, 883

[34] King A. R., Lasota J. P., 1991, Astrophys. J., **216**, L45

[35] Koyama K., Takano S., Tawara Y., Matsumoto T., Noguchi K., Fukui Y., Iwata T., Ohashi N., Tatematsu K., Takahashi N., Umemoto T., Hodapp K.W., Rayner J., Makishima K., 1991, Astrophus. J., **377**, 240

[36] Krzeminski W., 1977, Astrophys. J., **216**, L45

[37] Lamb D., 1974, Astrophys. J., **192**, L129

[38] Lamb D., 1988, (Theory of magnetic cataclysmic binary X-ray sources), in Polarized radiation of circumstellar origin, Vatican City State/Tucson, AZ, Vatican Observatory/University of Arizona Press, 1988

[39] Lubow S. H., 1989, Astrophys. J., **340**, 1064

[40] Lubow S. H., Shu F. H., 1975, Astrophys. J., **198**, 383

[41] Lubow S. H., Shu F. H., 1976, Astrophys. J., **207**, L53

[42] Mateo, M., Szkody, P., Garnavich, P. 1991, Astrophys. J., **380**, 380

[43] Motch C., Haberl F., 1995, (New Soft and Hard X-ray IPs from the ROSAT Galactic Plane Survey), in Proceedings of the Cape Workshop on Magnetic Cataclysmic Variables, Eds: Buckley D.A.H., Warner B., Pubs: Astronomical Society of the Pacific Conference Series, Vol 85, p. 113

[44] Norton A. J., 1993, Mon. Not. R. Astr. Soc., **265**, 316

[45] Norton A. J., Watson M. G., 1989, Mon. Not. R. Astr. Soc., **237**, 853

[46] Norton A. J., M^{c}Hardy I. M., Lehto H. J., Watson M. G., 1992, Mon. Not. R. Astr. Soc., **258**, 697

[47] Norton A.J., Beardmore A.P., Taylor P., 1996, Mon. Not. R. Astr. Soc., **280**, 937

[48] Norton A.J., Hellier C., Beardmore A.P., Wheatley P. J., Osborne J. P., Taylor P., 1997, Mon. Not. R. Astr. Soc., 000, 000

[49] O'Donoghue D., Koen C., Kilkenny D., 1996, Mon. Not. R. Astr. Soc., **278**, 1075

[50] Osborne J.P., Mason K.O., Bonnet-Bidaud J-M., Beuermann K., Rosen S., 1985, in Oda M., Giacconi R., eds, X-ray Astronomy '84, ISAS, Japan, p. 63

[51] Osborne J.P., Rosen S., Mason K.O., Beuermann K., 1985, Sp Sci Rev **40**, 143

[52] Patterson J., 1979, Astrophys. J., **234**, 978

[53] Patterson J., 1994, Publications. of the Astr. Soc. of the Pacific, **106**, 209

[54] Patterson J., Price C. M., 1981, Astrophys. J., **243**, L83

[55] Patterson, J., Moulden, M., 1993, Publications. of the Astr. Soc. of the Pacific, **105**, 779

[56] Penning W. R., 1985, Astrophys. J., **289**, 300

[57] Penning W. R., Schmidt G. D., Liebert J. E., 1986, Astrophys. J., **301**, 885

[58] Piirola V., Hakala P., Coyne G. V., 1993, Astrophys. J., **410**, L107

[59] Reinsch, K., 1994, Mon. Not. R. Astr. Soc., **281**, 108

[60] Ritter H., 1997, Astronomy & Astrophysics **85 3**, 1179R

[61] Rosen S. R. and Mason K. O., Córdova F. A., 1988, Mon. Not. R. Astr. Soc., **231**, 549

[62] Steiner J.E., Schwartz D.A., Jablonski F.J., Busko I.C., Watson M.G., Pye J.P., McHardy I.M., 1981, Astrophys. J., **249**, L21

[63] Tanaka Y., Inoue H., Holt S. S., 1994, Publications. of the Astr. Soc. of Japan, **46**, L37

[64] Taylor P., Beardmore A. P., Norton A. J., Osborne J. P., Watson M. J., 1997, Mon. Not. R. Astr. Soc., **289**, 349

[65] Turner M. J. L., Thomas H. D., Patchett B. E., Reading D. H., Makishima K., Ohashi T., Dotani T., Hayashida K., Inoue H., Kondo H., Koyama K., Mitsuda K., Ogawar Y., Takano S., Awaki H., Tawara Y., Makamura N., 1989, Publications. of the Astr. Soc. of Japan, **41**, 345

[66] Walker M. F., 1954, Publications. of the Astr. Soc. of the Pacific, **66** , 230

[67] Walker M. F., 1956, Astrophys. J., **123**, 68

[68] Warner B., 1996, Cataclysmic variable stars; Pubs: Cambridge University Press

[69] Warner B., Cropper M., 1984, Mon. Not. R. Astr. Soc., **206**, 261

[70] Warner B., Wickramasinghe D. T., 1991, Mon. Not. R. Astr. Soc., **248**, 370

[71] White N. E., Marshall F. E., 1981, Astrophys. J., **249**, L25

[72] Wynn G.A., King A. R., 1992, Mon. Not. R. Astr. Soc., **255**, 83

[73] Zhang E., Robinson E.L., Stiening R.F., Horne K., 1995, Astrophys. J., **454**, 447